The Dissertation Committee for Donghoon Kuk
certifies that this is the approved version of the following dissertation:

Experimental Studies of Laser Driven Proton Acceleration from Ultrashort and Highly Intense Laser Pulse Interaction with Overdense Plasma

Committee:

Todd Ditmire, Supervisor

Björn Manuel Hegelich

John W. Keto

Michael W. Downer

Milos Milosavljevic

Experimental Studies of Laser Driven Proton Acceleration from Ultrashort and Highly Intense Laser Pulse Interaction with Overdense Plasma

by

Donghoon Kuk, B.S., M.S., M.A.

DISSERTATION

Presented to the Faculty of the Graduate School of

The University of Texas at Austin

in Partial Fulfillment

of the Requirements

for the Degree of

DOCTOR OF PHILOSOPHY

THE UNIVERSITY OF TEXAS AT AUSTIN

December 2014

Dedicated to my Family.

Acknowledgments

I have buch of grateful peoples who have supported and assisted me to finish Ph.D. in physics successfully. First of all, I would like to say to my beloved family that I love you. They always encourage me to finish my degree and I know this is to theirs honer.

I appreciate to my supervisor Professor Todd Ditmire who inspires and supports me for long time. For the TC1 commissioning period, his supports and advising make me to be a big boy as an experimental physicist that can't be experienced at any other universities. I also appreciate to Dr. Gilliss Dyer who always illuminate me in practical and theoretical way. I also very appreciate to all members of the High Energy Density Physics group, Mike Donovan, Aaron Bernstein, Erhard Gaul, Hernan Quevedo, Ishay Pomerantz, Chunhua Want, Alex Arefiev, Sam Feldman, Joel Blakeney, Kristina Serratto, Craig Wagner, Franki Aymond, Sandi Bruce, Ahmed Helal, Sean Grant, Woosuk Bang, Intai Kim, Matt McCormick, Nirmala Kandadai, Johannes Rougk, Johannes Wenz. It was very happy hours to work with all of them at this group for the past 6 years. I also very appreciate all of the people who had and have worked at Texas Petawatt. Without their support, I can't finish my degree successfully.

And I also appreciate all of korean graduate student at the department of physics. Especially, I appreciate Dr. Hosik Lee and his family who have

been my good advisor, senior and good friend so long time. And I don't forget to comment about Dr. Austin Yi, Dr. Hosung Seo, Dr. Yooonsang Lee and their family. Whenever I need snuggies, they always be around, hang out and spend time with me. That is the most important legacy of my graduate school life.

I gratefully acknowledge for supports from professor Seung-Woo Hong at Sungkyunkwan University, and Professor Insoo Ko at POSTECH.

Experimental Studies of Laser Driven Proton Acceleration from Ultrashort and Highly Intense Laser Pulse Interaction with Overdense Plasma

Donghoon Kuk, Ph.D.
The University of Texas at Austin, 2014

Supervisor: Todd Ditmire

The generation of high current multi-MeV protons and ions by irradiation of short pulse high intense laser on an ultra-thin target has been observed and subjected great interest in recent. When ultra-thin overdense target is irradiated by focused ultraintense laser pulse, hot electrons are generated by various mechanisms and they generate energetic ion beams.

In TNSA, a quasi-electrostatic field is produced on the target rear surface when the the laser pulse interacts with overdense target, driving hot electrons go torward the target rear surface. However, this mechanism results in a range of field gradients leading to a broad proton energy distribution typically. To overcome the issue, an alternative accelration mechanism has been presented to achieve the quasi-monoenergetic proton acceleration and the mechanism is called Radiation Pressure Acceleration. In the RPA, the radiation pressure push electrons into the target smoothly and setting up an electrostatic field by the laser pressure.

In this thesis, we study two alternative experimental methods for the quasi-monoenergetic proton acceleration and find experimental feasibility of the presented methods from other research groups.

Table of Contents

Acknowledgments **v**

Abstract **vii**

List of Figures **xii**

Chapter 1. Introduction **1**

Chapter 2. Basic Concepts and Model of Plasma **5**

2.1 Debye Sheath 5

2.2 Ponderomotive Force 6

2.3 Dispersion relation in a homogeneous plasma and critical density 8

2.4 Maxwell's Equations in a Medium 9

Chapter 3. Physics of High Intensity Laser - Solid Density Matter Interactions **12**

3.1 Analytical solution for linear density gradient plasma 12

3.2 Obliquely Incident of Laser Light Wave in Inhomogeneous Plasma (Resonance Absorption) 14

3.2.1 S-Polarized Laser Light Wave Propagation 14

3.2.2 P-Polarized Laser Light Wave Propagation - Resonance absorption 16

3.3 Inverse Bremsstrahlung (Collisional Heating) 20

3.4 Relativistic $\mathbf{J} \times \mathbf{B}$ Heating 21

3.5 Vacuum Heating (Brunel-type Heating) 22

Chapter 4. High Energy Proton Acceleration in Interaction of Short Laser Pulse with Solid Target **25**

4.1 Target Normal Sheath Acceleration (TNSA) 26

4.2 Radiation Pressure Acceleration (RPA) 31

Chapter 5. Accelerated Charged Particle Detector **33**
5.1 Radiochromic RCF film 33
5.1.1 RCF Imaging Spectroscopy 33
5.1.2 Stopping Power 36
5.2 Phosphor Screen Image Plate 41
5.3 Thomson Parabola Spectrometer 42
5.4 Electron Spectrometer 47

Chapter 6. Experimental Setup and Data **52**
6.1 Laser System 52
6.1.1 GHOST Laser 52
6.1.2 Texas Petawatt Laser 55
6.2 Micro-structured Target Experiments at the TPW 57
6.2.1 Motivation 57
6.2.2 Microstructured Target Fabrication 58
6.2.3 Experimental Setup 65
6.2.4 Results 69
6.3 Circularly Polarized Laser Experiments at the GHOST 74
6.3.1 Motivation 74
6.3.2 PMMA Target Fabrication 75
6.3.3 Experimental Setup 77
6.3.4 Results 88
6.3.5 EPOCH simulation 107

Chapter 7. Summary **118**

Appendices **120**

Appendix A. Operation Procedure at the Microelectronics Research Center at J. J. Pickle Research Campus **121**
A.1 Hood C16 - Piranha Cleaning 121
A.1.1 Procedure 121
A.2 LPCVD Nitride - MRL 122
A.3 Woollam Ellipsometer 125

A.4 RIE Etcher - 790 Plasma Therm #2 128
A.5 Hood H18 - KOH Etching 130
A.6 Denton DV - 502A Thermal Evaporator 132

Appendix B. Pulse duration calculation from the 2nd order Auto-correlation Measurement of the GHOST 134

Appendix C. EPOCH input deck file 136
C.1 LP, 20nm PMMA target 136
C.2 CP, 20nm PMMA target 140

Appendix D. Igor Pro Electron Spectrometer Analysis Code 146
D.1 Igor Pro Procedure for the Electron spectrometer analysis . . . 146

Bibliography 149

List of Figures

1.1 Progress in peak intensity sicen the invention of the laser in 1960 [24] 2

3.1 For $L/\lambda_L \sim 1000$ scale length, plot of laser electric field as it propagate into a linear density profile plasma region from vacuum into solid target with long prepulse. 13

3.2 Geometry of plane-wave incidient on a plasma density profile for s-polarized light (E-field in the x-direction). [23] 15

3.3 Geometry of plane-wave incidient on a plasma density profile for p-polarized light (E-field in the z-direction). [23] 17

3.4 A plot of the function $\phi(\tau)$, which characterize the efficiency of resonance absorption. Region in A ($\theta \to 0$), the E_d is too much week. Region in B ($\theta \to 90\,^\circ$), on the other hand, the driver field have to tunnel through too long distance, so E_d getting week exponentially. 19

3.5 Scheme of vacuum heating mechanism. Strongly p-polarized laser pulse can directly pull electrons out of the sharp boundary of plasma and kikc them back into overdense region. 23

4.1 Ions can be accelerated backwards by the ambi-polar field at the front of laser-irradiated plasma plume. They can be also accelerated forward by the sheath field that is set on the target rear surface. 27

4.2 Numerical result of electric field at the ion front as a function of time. The accelerating sheath field is shown that dramatically decreased in few ion plasma time scale [41] 29

4.3 Left graph shows the maximum proton energy as a function of laser pulse duration. Laser intensities labelled on left-top corner are in units of W/cm^2. Lines present calculation for various laser intensity using free expansion model with fluid model assuming 20 μm thick target and 10μm FWHM laser focal spot. Right graphs shows number of protons in a 1 MeV bin around 10 MeV as a function of laser irradiance for same model, target and laser focal spot condition [19]. 30

4.4 RPA PIC simulation for the $n = 8n_{cr}$ (L) and $n = 2n_{cr}$ (R) target [16]. 32

5.1 Configuration of GAFCHROMIC® for MD-55 (left) and HD-810 dosimetry films (right). 34
5.2 Dose response curves for three different types of RFC. 35
5.3 OD calibration for the Konica Minolta DiIMAGE Scan Dual IV film scanner. 36
5.4 The Bragg curve of 5.49 MeV alpha particles in the air [1]. . . 38
5.5 SRIM stopping power simulation of the RCF stack with the proton beams. 39
5.7 Bragg Peak for the RCF HD-810 stack from the shot shown in figure 5.6. 39
5.6 RCF data of the TPW commissioning shot. #2118 on a 5 μm Ti target. 40
5.8 Composite structure of Storage Phosphor Screen BAS-IP. . . . 41
5.9 Diagram of Thomson parabola spectrometer where the magnet plates and elecstrodes are shown. 42
5.10 Particle tracking study of the Thomson spectrometer with SIMION and solidwork design. 43
5.11 Machining of the Thomson spectrometer. 44
5.12 Radiaion shielding block and pinhole of the Thomson spectrometer. 45
5.13 HV test of the Thomson spectrometer in the vacuum. 46
5.14 Particle parabolic trajectories and data analysis with the matlab. 47
5.15 Electron spectrometer. 48
5.16 β^- decay scheme of the ^{90}Sr. 49
5.17 Calibration curve of electron spectrometer using a ^{90}Sr source. 50
5.18 Calibration curve fitting with the Larmor curve of data shown in the figure 5.17. 51

6.1 The layout of the GHOST Laser. 53
6.2 GHOST 2nd order autocorrelation stage. 54
6.3 GHOST 2nd order autocorrelation calibraion image. 55
6.4 The laser layout of the Texas Petawatt Laser. 57

6.5 Conceptual scheme of the micro-structured target experiment. Micro-dot can be aligned with the main focal spot and the ablation laser. [53] 58
6.6 Micro-dot target fabrication process 60
6.7 Absorption and emission spectrum of the Rhodamine 6G . . . 61
6.8 Micro-dot array target on a silver film coated on a substrate . 63
6.9 Micro-dot array target on the target holder 64
6.10 Image relay of the focal spot. 66
6.11 Ablation beam setup 67
6.12 Micro-dot target on the focal spot. 68
6.13 Micro-dot target alignment procedure 70
6.14 Proton energy spectrum of the micro-dot expriment. 73
6.15 Pointing error analysis with the Far-Field diagnostic image. . . 73
6.16 50 nm PMMA film on the substrate. 75
6.17 A scheme for the PMMA target fabrication. 76
6.18 Vibration ellipse of light reflected from a metal at the principal angle of incidence. 77
6.19 (a) A periscope scheme for 0° rotation in azimuthal angle of the polarization. (b) 90° rotation scheme. (c) 45° rotation scheme. (d) 45° rotation setup. 79
6.20 Scheme of the periscope and M1 setup for circularly polarized beam generation. 80
6.21 Beam intensity measurement for rotating the polarizer 360°. . 82
6.22 (a) Proton energy spectrum for $a_0 = 20$ and different ellipticities. (b) Dependence of thershold ellipticity on a_0. (c) Dependence of the proton bunch energy on ellipticity for $a_0 = 20$ [51]. 83
6.23 Through focus beam setup with 20X infinity-corrected Objectives. 84
6.24 Focal spot image and its contour line. 86
6.25 STM tip end image alogn the through focus line. 87
6.26 Experimental setup with the Thomson parabola spectrometer. 88
6.27 Raw data for the CP setup with PMMA targets. 93
6.28 Raw data for the linearly polarized setup with PMMA targets. 94
6.29 Electron energy spectrum for 20 nm PMMA targets. 95
6.30 Electron energy spectrum for 30 nm PMMA targets. 96

6.31 Electron energy spectrum for 52 nm PMMA targets. 97
6.32 Electron energy spectrum for 85 nm PMMA targets. 98
6.33 Electron energy spectrum for 113 nm PMMA targets. 99
6.34 Electron energy spectrum for 230 nm PMMA targets. 100
6.35 Proton energy spectrum for 20 nm PMMA targets. 101
6.36 Proton energy spectrum for 30 nm PMMA targets. 102
6.37 Proton energy spectrum for 52 nm PMMA targets. 103
6.38 Proton energy spectrum for 63 nm PMMA targets. 104
6.39 Proton energy spectrum for 85 nm PMMA targets. 105
6.40 Proton energy spectrum for 113 nm PMMA targets. 106
6.41 Proton energy spectrum for 230 nm PMMA targets. 107
6.42 EPOCH cell size. 108
6.43 Gaussian beam parameters. 108
6.44 E field of the propagating linearly polarized laser. 110
6.45 E field of the propagating circularly polarized laser. 111
6.46 Electron density evolution for the linearly polarized beam with the 20 nm PMMA target. 112
6.47 Hydrogen density evolution for the linearly polarized beam with the 20 nm PMMA target. 113
6.48 Electron density evolution for the circularly polarized beam with the 20 nm PMMA target. 114
6.49 Hydrogen density evolution for the circularly polarized beam with the 20 nm PMMA target. 115
6.50 Electron energy sprctrum of 20nm PMMA target. Top is for the linearly polarized and bottom is for the circularly polarized beam. 116
6.51 Proton energy sprctrum of 20nm PMMA target. Top is for the linearly polarized and bottom is for the circularly polarized beam. 117

B.1 Schematic of the 2nd order autocorrelation. [49] 134
B.2 GHOST laser pulse duration calculation from the 2nd order autocorrelation data data 135

Chapter 1

Introduction

The recent development of ultrashort high intensity laser pulses has allowed for the generation of laser intensities that are orders of magnitude over what was possible with previous laser technology. The ultrashort regime includes laser light with pulse lengths τ_p of 30 μm (10 fs) up to 3 mm (10 ps). The high intensity regime covers intensities starting at 10^{17} W/cm^2, and now reaches up to approximately 10^{21} W/cm^2. Even as late as ten years ago, most lasers could not produce light that could approach this high intensity region, with the exception of a few CO_2 lasers built in the 1970s [24]. Now, there are a large number of high intensity lasers all over the world. What made this possible was the application of Chirped-Pulse Amplification (CPA) and Optical Parametric Chirped-Pulse Amplification (OPCPA) technology. This breakthrough in laser hardware has aroused considerable interests in ultrashort high-intensity laser matter interactions. Never before has it been possible to deposit so much laser energy in such a short amount of time, in such a tiny volume on the front of a target. As shown in the figure 1.1 courtesy of [24], in today the state-of-the-art laser technology allows us to investigate in region of fusion research and praticle acceleration since we have achieved enough intensity laser for the relativistic limit.

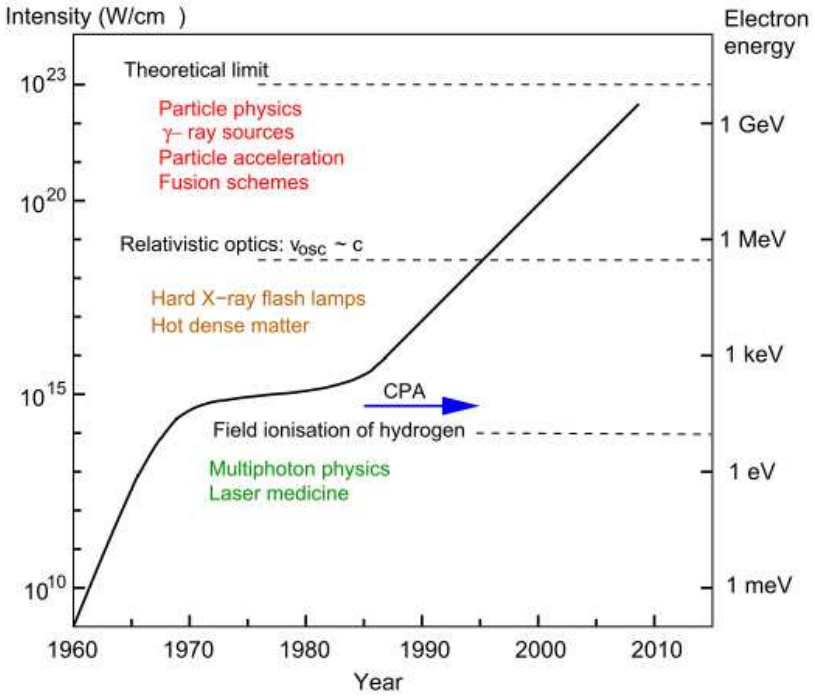

Figure 1.1: Progress in peak intensity sicen the invention of the laser in 1960 [24]

The relativistic character of laser radiation with intensity I is realized at the magnitude of a dimensionless parameter $a_0 > 1$ where $a_0 = \dfrac{eE_0}{m_e c\omega_0}$ is the dimensionless normalized vector potential [15]. This parameter represents the dimensionless momentum of the electron oscillating in the electric field of linearly polarized laser radiation and can be expressed as

$$a_0 = \frac{eE}{m_e c\omega_0} = 0.85\lambda_L \left(\frac{I}{10^{18}}\right)^{1/2} , \tag{1.1}$$

$$E = \sqrt{\frac{2I}{c\,\varepsilon_0}} = 27.7\, I^{1/2} \quad \text{in} \quad \mathrm{V/cm}^2 \tag{1.2}$$

where e and m_e are the charge and mass of the electron, respectively, E is the amplitude of electric field strength of laser radiation, λ_L is the radiation wavelength in μm, ω is the frequency of laser radiation, c is the speed of light, and I is the radiation intensity in W/cm^2.

Terawatt-power laser systems can fulfill the condition $a_0 > 1$, which corresponds to the electric field strength above 10^{10} V/cm . In such intense fields, the overbarrier ionization of atoms occurs in atomic time on the order of 10^{-17} s, and the electrons produced are accelerated and reach MeV-range relativistic energies during the laser pulse.

The acceleration of atomic ions in femto and picosecond laser plasmas constitutes a secondary process. It is caused by the strong quasistatic electric fields arising due to spatial charge separation. Such separation is related to the motion of a bunch of fast electrons. For laser radiation intensities exceeding $I \geq 10^{18}$ W/cm^2, it is possible to obtain directed beams of high energy ions with the energies more than 1 MeV. Note that this ion acceleration is not caused directly by the laser **E** field, we will review about this at chapter 4.

In this thesis, experimental studies for the laser driven quasi-monoenergetic proton acceleration are introduced and presented. Two different experiments suggested from other research groups are carried out to study the experimental feasibility for the quasi-monoenergetic proton acceleration. One is the micro-dot target experiment introduced at the chapter 6.2. And the other is circularly polarized laser beam experiment at chapter 6.3. To accomplish the experimental studies, theoretical background for the plasma physics and

detector science is introduced. From chapter 2 to chapter 3, basic concepts for the plasma physics and physical mechanisms of the laser driven hot electrons generation are introduced. And in the chapter 4, physical mechanisms for the laser driven proton acceleration are introduced. In the chapter 5, we review the energetic ions beam detector such like RCF film stack and Thomson parabola spectrometer which are used in the experiments. In the chapter 6, the two experiments for the quasi-monoenergetic proton acceleration are introduced. The numerical studies with EPOCH simulation for the experiments are presented in the chapter 6. And we summarize the experiments and the results in the chapter 7.

Chapter 2

Basic Concepts and Model of Plasma

In this chapter, we will review basic concepts about plasma and its properties. That is a little bit prior background assumed for starting laser-plasma interaction. Review for basic properties of plasma could be an appropriate start for this thesis.

2.1 Debye Sheath

A plasma has very important character of shielding electric potential. This can be happened by the response of electron cloud in $1/\omega_{pe}$ time scale is faster than characteristic time scale of system perturbation. We can start from Poisson equation for a particle of charge q at position $x = 0$,

$$\nabla^2\phi = -4\pi q\delta(\mathbf{x}) + 4\pi e(n_e - n_0) \tag{2.1}$$

where the ions are treated as a neutralizing background n_{i0} and the electron density is initially uniform so, $n_e = n_0$. In a static limit ($\partial/\partial t = 0$ and $v_e = 0$), the fluid momentum equation of plasma reduces to

$$0 = n_e eE + k_B T_e \nabla n_e \quad . \tag{2.2}$$

With $\mathbf{E} = -\nabla\phi$, the electron density becomes

$$n_e = n_0 \exp\left(\frac{e\phi}{k_B T_e}\right) \quad . \tag{2.3}$$

An equation for the electric potential ϕ can be obtained by Taylor Expansion of equation 2.3 for small $e\phi/k_B T_e$ and substituting n_e into equation 2.1:

$$\nabla^2\phi - \frac{\phi}{\lambda_D} = -4\pi q\delta(\mathbf{x}) \tag{2.4}$$

where $\lambda_D = \sqrt{k_B T_e/4\pi n_0 e^2}$ defines the electron Debye length. The solution of equation 2.4 has a Yukawa potential (i.e. screened Coulomb potential) shape of

$$\phi = \frac{q}{\mathbf{x}}\, e^{-\mathbf{x}/\lambda_D} \tag{2.5}$$

and then, the meaning of the Debye length becomes obvious. The usually Coulomb like potential of a single charge q is shielded out by the collective effect of an electron density n_e, where the Debye length is the characteristic length.

2.2 Ponderomotive Force

The ponderomotive force is caused by the gradient of the time-averaged oscillating potential. Let's consider the non-relativistic case of a single electron oscillating near the center of a focused laser beam. In the limit $v/c \ll 1$, the equation of motion for the electorn becomes

$$\frac{\partial v_y}{\partial t} = -\frac{e}{m_e} E_y(\mathbf{r}) \quad . \tag{2.6}$$

The electromagnetic wave is taken to be propagating in the x-direction but has radial intensity dependence, assuming only in y-direction. Taylor expansion of the electric field then gives

$$E_y(\mathbf{r}) \simeq E_0(y)\cos\phi + y\frac{\partial E_0(y)}{\partial y}\cos\phi + \cdots \quad , \tag{2.7}$$

where $\phi = \omega t - kx$. To lowest order, we therefore obtain

$$v_y^{(1)} = -v_{osc}\sin\phi \tag{2.8}$$

$$y^{(1)} = \frac{v_{osc}}{\omega}\cos\phi \tag{2.9}$$

where $v_{osc} = \dfrac{eE_0}{m_e\omega}$ is osciallting velocity of electron in the $\mathbf{E}$. Substituting above 1^{st} order term of velocity and position into equation 2.6 gives

$$\frac{\partial v_y^{(2)}}{\partial t} = -\frac{e^2}{m_e^2\omega^2}E_0\frac{\partial E_0(y)}{\partial y}\cos^2\phi \quad . \tag{2.10}$$

Multiplying by m_e and taking the time average gives the ponderomotive force on the electron

$$f_p \equiv \overline{m_e\frac{\partial v_y^{(2)}}{\partial t}} = -\frac{e^2}{4m_e\omega^2}\frac{\partial E_0^2}{\partial y} \tag{2.11}$$

Note that this forece is just expression of gradient of the ponderomotive potential [15]

$$U_p = \frac{e^2E^2}{4m_e\omega^2} = 9.33\times10^{-14}\,I[\mathrm{W}/cm^2]\,\lambda_{\mu m}^2 \quad \mathrm{eV} \tag{2.12}$$

For example, roughly 10 keV ponderomotive energy for a Nd:Phosphate glass laser at 1.054 μm focused to intensity of 10^{17} W/cm^2 . Physically, the foce will tend to push electrons away from region of locally higher intensity to lower

intensity. A single electron will therefore inevitably drift away from the center of focused laser beam, picking up a velocity $v \sim v_{osc}$ in the process.

The expression for relativistic ponderomotive force is given following as

$$f_p = -m_e c^2 \nabla \overline{\gamma_{osc}} \quad , \tag{2.13}$$

where $\gamma_{osc} = (1 + +a_0^2/2)^{1/2}$ [24]. Then the relativistic ponderomotive energy can be written as [15]

$$U_p^{rel} = (\gamma_{osc} - 1) m_0 c^2 \tag{2.14}$$

and the effective electron temperature associated with this relativistic ponderomotive potential can be written as [61]

$$T_{hot} \approx \left(\sqrt{1 + \frac{I \lambda_{\mu m}^2}{1.37 \times 10^{18}}} - 1 \right) 511 \quad \text{keV} \tag{2.15}$$

where $\lambda_{\mu m}$ is the wave length of laser in μm.

2.3 Dispersion relation in a homogeneous plasma and critical density

If a plane wave propagates a quasi-neutral homegeneous plasma, then the phase velocity of electromagnetic waves in a dielectric medium can be expressed in terms of dielectric constant

$$v_p = \frac{\omega}{k} = \frac{c}{n} = \frac{c}{\sqrt{\varepsilon}} \quad . \tag{2.16}$$

And the dielectric constant for plasma can be also expressed in terms of plasma frequency;

$$\varepsilon = 1 - \frac{{\omega_{pe}}^2}{\omega^2} \quad \text{where} \quad {\omega_{pe}}^2 = \frac{4\pi n_e e^2}{m_e} \quad . \tag{2.17}$$

From equation 2.16, 2.17, we can get a dispersion relation of wave which propagates through homegeneous plasma:

$$\omega^2 = {\omega_{pe}}^2 + c^2 k^2 \quad . \tag{2.18}$$

Note that ω_{pe} is the cut-off frequency for propagating wave in a plasma. Because the characteristic response time for electrons is ω_{pe}^{-1}, the electrons in a plasma would shield out the wave when $\omega < \omega_{pe}$. Therefore the maximum plasma density to which a light wave can penerates depends on the cut-off condition $\omega = \omega_{pe}$. This is called critical density, n_{cr}, and we can categorize under-dense, over-dense plasma by criterion of n_{cr}

$$n_{\text{underdense}} < n_{cr} < n_{\text{overdense}} \quad .$$

And we can have very useful expression for the critical density in terms of free-space wavelength of the laser in units of microns

$$n_{cr} \quad = \quad \frac{m_e}{4\pi e^2}\omega^2 = 1.1 \times 10^{21}/\lambda_{\mu m}^2 \quad \text{cm}^{-3} \quad . \tag{2.19}$$

2.4 Maxwell's Equations in a Medium

Let's consider general wave propagation in a plasma. Our approach is to view a plasma as a linear dielectric and describe wave propagation through such a dielectric material. Let's recall the Maxwell's equations in a medium

$$\nabla \times \mathbf{E} = \frac{i\omega}{c}\mathbf{B} \tag{2.20}$$

$$\nabla \times \mathbf{B} = -\frac{i\omega}{c}\varepsilon\mathbf{E} \quad . \tag{2.21}$$

There are two things we can do these equation in order to make them wave-like. First, we can take a curl of the Faraday's Law

$$\begin{aligned} & \nabla \times \mathbf{E} = \frac{i\omega}{c}\mathbf{B} \\ \rightarrow \quad & \nabla \times (\nabla \times \mathbf{E}) = \nabla \times \frac{i\omega}{c}\mathbf{B} \\ \rightarrow \quad & \nabla^2\mathbf{E} - \nabla(\nabla \cdot \mathbf{E}) + \frac{\omega^2}{c^2}\varepsilon\mathbf{E} = 0 \quad . \end{aligned} \tag{2.22}$$

Second, we can multiply ε^{-1} by Ampere's Law and take its curl

$$\begin{aligned} & \nabla \times \mathbf{B} = -\frac{i\omega}{c}\varepsilon\mathbf{E} \\ \rightarrow \quad & \nabla \times (\nabla \times \mathbf{B}) = -\frac{i\omega}{c}(\nabla \times \varepsilon\mathbf{E}) \\ \rightarrow \quad & \nabla^2\mathbf{B} - \nabla \underbrace{(\nabla \cdot \mathbf{B})}_{0} = \frac{i\omega}{c}\left(\varepsilon\left(\nabla \times \mathbf{E}\right) + (\nabla\varepsilon \times \mathbf{E})\right) \\ \rightarrow \quad & \nabla^2\mathbf{B} + \frac{\omega^2}{c^2}\varepsilon\mathbf{B} + \frac{1}{\varepsilon}\nabla\varepsilon \times (\nabla \times \mathbf{B}) = 0 \quad . \end{aligned} \tag{2.23}$$

Now, let's consider about the propagation of laser light wave in an inhomogeneous plasma. Assuming variations only in z-direction, then we can have

$$\begin{aligned} n_0 &= n_0(z) \quad , \\ \varepsilon &= \varepsilon(\omega, z) \quad , \\ \mathbf{E}_\perp &= \mathbf{E}(z)\exp(-i\omega t) \quad . \end{aligned}$$

Then the equation 2.22 become

$$\begin{aligned} \frac{d^2}{dz^2}E_\perp + \frac{\omega^2}{c^2}\varepsilon E_\perp &= 0 \quad , \\ \varepsilon E_z &= 0 \quad . \end{aligned} \tag{2.24}$$

and the equation 2.23 become

$$\begin{aligned} \frac{d^2}{dz^2}B_\perp + \frac{\omega^2}{c^2}\varepsilon B_\perp - \frac{1}{\varepsilon}\frac{d\varepsilon}{dz}\frac{dB_\perp}{dz} &= 0 \quad , \\ \frac{dB_z}{dz} &= 0 \quad . \end{aligned} \tag{2.25}$$

Chapter 3

Physics of High Intensity Laser - Solid Density Matter Interactions

The interaction of high intensity laser pulse with solid density matter involves a variety of processes and mechanisms: ionization, laser propagation and refraction, plasma wave generation, and subsequent thermal and hydrodynamic evolution of targets. In this chapter, basic theory about hot electron generation associated with proton acceleration will be introduced.

3.1 Analytical solution for linear density gradient plasma

When high intensity laser pulse interact with solid density matter and travels into that matter, the surface undergoes ionization due to the strong electric field of laser. Even though pre-pulse, it is enough strong to ionize the target surface so the main pulse interact with this pre-plasma at first, however the inner matter still remains solid density, so we may need to consider a situation of linear density gradient. Let's consider the linear plasma density gradient situation in the z-direction, so $n = n_{cr}z/L$ where the L is density scale length (the length over which the electron density ramps up from 0 to n_{cr} [15]). Then we can recall the equations 2.17, 2.24 and put $n_{cr} = m_e\omega^2/4\pi e^2$

into equation, we obtained

$$\frac{d^2E}{dz^2} + \frac{\omega^2}{c^2}\left(1 - \frac{z}{L}\right)E = 0 \quad . \tag{3.1}$$

Substitution a variable $\eta \equiv \left(\frac{\omega^2}{c^2 L}\right)^{1/3}(z - L)$ into equation 3.1, then this gives a well known differential equation as the Airy equation

$$.\frac{d^2E}{d\eta^2} - \eta E = 0 \tag{3.2}$$

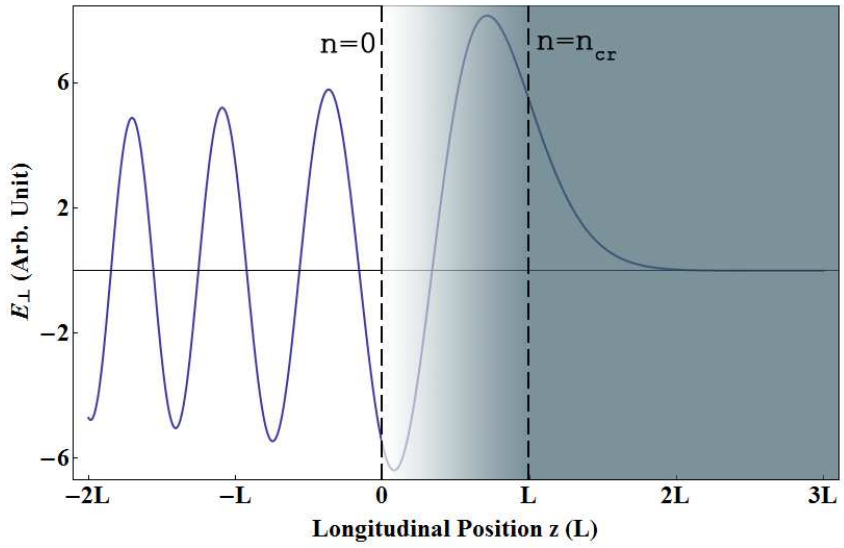

Figure 3.1: For $L/\lambda_L \sim 1000$ scale length, plot of laser electric field as it propagate into a linear density profile plasma region from vacuum into solid target with long prepulse.

Well known general solution of this equation leads the electric field as following,

$$E(z) = 2\sqrt{\pi}\left(\frac{\omega L}{c}\right)^{1/6} E_{FS}\, e^{i\phi} Ai((\omega^2/c^2 L)^{1/3}(z - L)) \quad . \tag{3.3}$$

As can be seen from figure 3.1, the amplitude of the laser electric field swells before it reach but near n_{cr} cut-off plane. The extent of this swelling is approximately given as [34]

$$\left|\frac{E_{max}}{E_{FS}}\right|^2 \simeq 3.6\left(\frac{\omega L}{c}\right)^{1/3} \quad . \tag{3.4}$$

3.2 Obliquely Incident of Laser Light Wave in Inhomogeneous Plasma (Resonance Absorption)

We again consider a plane electromagnetic wave incidient onto a plasma slab with electron density $n_e(z)$. The vacuum-plasma interface is taken to be at $z = 0$. Let's consider a laser light wave which propagates into plasma slab with an incidient angle θ, between of laser propagation vector k and to plasma density gradient $\hat{z}$. Here we set a plane of incidence as a yz-plane, and the vacuum plasma interface as $z = 0$. Thus, $\partial/\partial x = 0, k_x = 0, k_y = (\omega/c)\sin\theta, k_z = (\omega/c)\cos\theta$.

3.2.1 S-Polarized Laser Light Wave Propagation

For s-polrized incidien laser, the electric field is suppose to point out $y - z$ plane. We can take $\mathbf{E} = E_x\hat{x}$, then equation 2.22 becomes

$$\frac{\partial^2 E_x}{\partial y^2} + \frac{\partial^2 E_x}{\partial z^2} + \frac{\omega^2}{c^2}\varepsilon(z)E_x = 0 \quad . \tag{3.5}$$

The dielectric function, ε, of the plasma depends on z only, k_y can be expressed as $k_y = (\omega/c)\sin\theta$.Then the E_x can be expressed as

$$E_x = E(z)e^{ik_y y} = E(z)\exp\left(\frac{i\omega y\sin\theta}{c}\right) \quad . \tag{3.6}$$

Substituting equation 3.6 into equation 3.5 returns

$$\frac{d^2E(z)}{dz^2} + \frac{\omega^2}{c^2}\left(\varepsilon(z) - \sin^2\theta\right)E(z) = 0 \quad . \tag{3.7}$$

This reduced wave equation gives us very simple and apparent understanding that reflection of the laser light wave occurs when

$$\varepsilon(z) = \sin^2\theta \quad . \tag{3.8}$$

We can derive the density at this reflection plane as $n_e = n_{cr}\cos^2\theta$ from equation 2.17. This means that an obliquely incidient s-polarized laser light wave reflects at a density lower than the critical density. i.e., $n_e = n_{cr}\cos^2\theta$. A copied scheme for the S-polarization incident on the plasma is shown in the figure 3.2 [23].

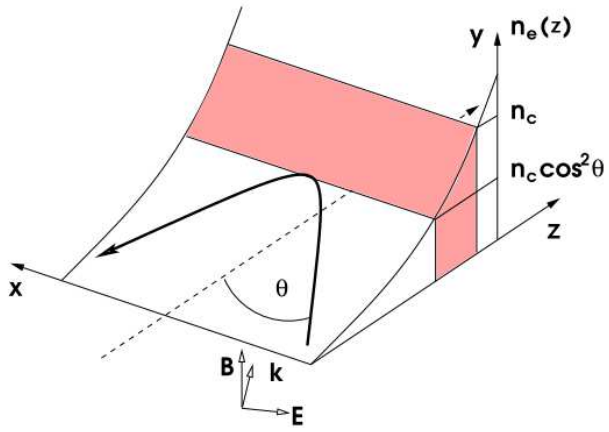

Figure 3.2: Geometry of plane-wave incidient on a plasma density profile for s-polarized light (E-field in the x-direction). [23]

3.2.2 P-Polarized Laser Light Wave Propagation - Resonance absorption

Now let's consider the case that the electric field of the wave lies in the plane of incidence, namely, p-polarized wave. In this case, there is a longitudinal component of electric field which is parallel with the density gradient direction, i.e. $\mathbf{E} \cdot \nabla n_e \neq 0$. This field contributes the oscillation of plasma in longitudinal direction and generate charge density fluctuation. This motivation can be enhanced resonant oscillation of plasma wave and some fraction of laser energy can be transferred into plasma wave energy, this phenomenon is called resonance absorption. Although the obliquely incident light reflects at the surface of $\varepsilon = \sin^2\theta$, where its density is less than the critical density, it can still tunnel into the critical surface and drives fluctuations in plasma density.

Let's configure this phenomenon some more analytically. the electric field in the plane of incident can be written as $\mathbf{E} = E_y\hat{y} + E_z\hat{z}$. The Poission equation is becomes

$$\begin{aligned} \nabla \cdot (\varepsilon \mathbf{E}) &= 0 \quad , \\ \nabla \cdot \mathbf{E} &= -\frac{1}{\varepsilon}\frac{\partial \varepsilon}{\partial z} E_z \quad . \end{aligned}$$

where $\varepsilon(z) = 1 - \omega_{pe}^2(z)/\omega^2$ is the plasma dielectric function. The resonant happens where $\omega_{pe} = \omega$.

The magnetic field for p-polarized case is $\mathbf{B} = B_x\hat{x}$ and similar to equation 3.6, B field can be written as

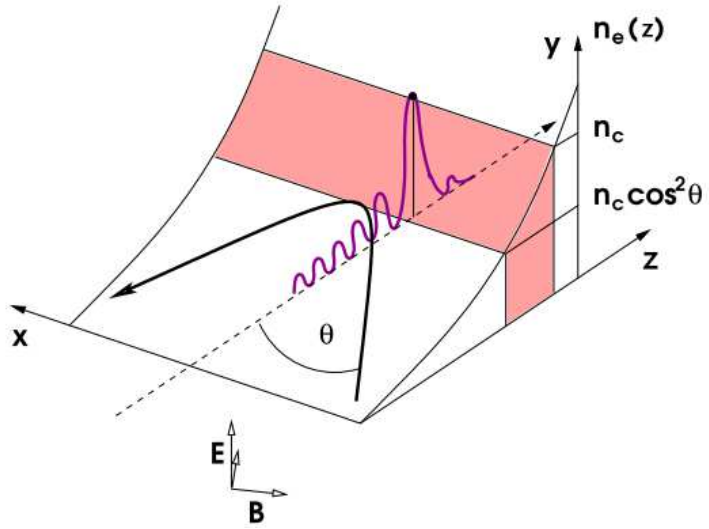

Figure 3.3: Geometry of plane-wave incidient on a plasma density profile for p-polarized light (E-field in the z-direction). [23]

$$\mathbf{B} = B(z)\exp\left(-i\omega t + \frac{i\omega y\sin\theta}{c}\right)\hat{x} \quad . \tag{3.9}$$

Now we can plug in equation 3.9 into equation 2.21 to get the associated **E**, then the z-component of electric field is driven as

$$E_z = \frac{\sin\theta B(z)}{\varepsilon(z)} \quad . \tag{3.10}$$

With an approximation $E_z = E_d/\varepsilon(z)$, the resonant driving field at the critical density E_d is estimated as the following form

$$E_d = B(z = L\cos^2\theta)\sin\theta e^{-i\beta} \quad . \tag{3.11}$$

Here, we assume a linear density profile again, i.e., $n_e = n_c rz/L$.

Then the cut-off of laser is $z = L\cos^2\theta$. Magnitude of magnetic field at the critical surface is evaluated from the exponential decaying of the field at the reflection plane and the decaying factor is defined as [34]

$$\beta = \int_{L\cos^2\theta}^{L} \frac{1}{c}\sqrt{\omega_{pe}^2 - \omega^2\cos^2\theta}\, dz = \frac{2\omega L}{3c}\sin^3\theta \quad . \tag{3.12}$$

Let's define new parameter $\tau = (\omega L/c)^{1/3}\sin\theta$, then we can find

$$E_d = \frac{E_{FS}}{\sqrt{2\pi\omega L/c}}\phi(\tau) \tag{3.13}$$

where $\phi(\tau) \simeq 2.3\tau\exp(-2\tau^3/3)$.

A copied scheme for the P-polarization incident on the plasma is shown in the figure 3.3 [23]. equation 3.13 implies that there is an optimum angle of incidence for the maximum absorption. E_d vanishes as τ (or θ) approaches zero, since the component of electric field of laser parallel to the plasma gradient is proportional to $\sin\theta$. When angle of incidence is large ($\theta \to 90\,^\circ$), the distance that the evanescent wave has to penetrate is too long and the driver field intensity getting small. Between these two limits, there is an optimum angle of incidence given approximately by

$$\theta_{max} \simeq \sin^{-1}\left(0.8\left(\frac{\omega L}{c}\right)^{-1/3}\right) \quad . \tag{3.14}$$

The large amplitude of plasma wave is damped by various processes, such as electron-ion collisions, wave-particle interactions or even the wave and particle propagation out of the resonant region. If we assume that the linear density profile and small damping frequency, $\nu/\omega \ll 1$, the absorbed energy

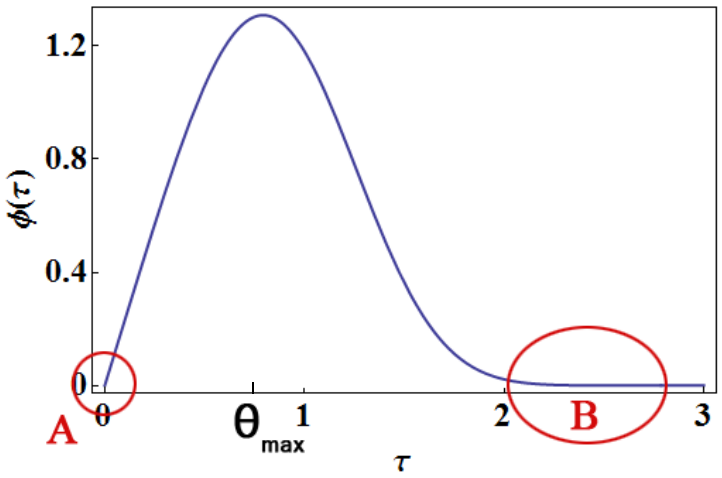

Figure 3.4: A plot of the function $\phi(\tau)$, which characterize the efficiency of resonance absorption. Region in A ($\theta \to 0$), the E_d is too much week. Region in B ($\theta \to 90\,^\circ$), on the other hand, the driver field have to tunnel through too long distance, so E_d getting week exponentially.

flux is given by [34]

$$I_{abs} \approx \frac{\omega L E_d^2}{8} = f_A \frac{E_{FS}^2}{8\pi} c \tag{3.15}$$

where f_A is the fractional absorption of the laser energy. Through these resonant processes, absorbed laser energy is mainly converted into electron kinetic energy without collisions and they are driven once inward and once outward of the target per single laser cycle.

The formula of the temperature of the hot electron generated by the resonance absorption is given by Wilks [61]

$$T_{hot} \approx 10 \left[T_{\mathrm{keV}} I_{15} \lambda_\mu^2 \right]^{1/3} \text{ keV} \tag{3.16}$$

where the $T_{\rm keV}$ is the background electron temperature in keV, I_{15} is the laser intensity in units of 10^{15} W/cm^2 and λ_μ^2 is the laser wavelength in microns.

3.3 Inverse Bremsstrahlung (Collisional Heating)

Inverse Bremsstrahlung is the most relevant collisional process which arises from electrons that have gained energy from the photon, then lose this energy in collisions with ions. Let's consider that electrons that are oscillating in an electric field acquire energy from laser by this oscillation. The scaling for T_e is now given more by the ponderomotive potential, instead of by resonance absorption [61]. Thus the electrons acquire energy order of pondoromotive potential energy and this energy is then transferred to ions by collisions and the plasma heats up. The fractional absorption is [63]

$$f_{ib} = 1 - \exp\left(-\frac{32}{15}\frac{\nu_{ei}(n_{cr})}{c}L\right) \tag{3.17}$$

where L is the density scale length of a linear density profile and $\nu_{ei}(n_{cr})$ is the electron-ion collision frequency evaluated at the critical density n_{cr} . The collisional frequency (in the weak field limit) depends on T_e, n_e and Z in the following way

$$\nu_{ei}(n_{cr}) \propto \frac{n_{cr}Z}{(k_B T_e)^{3/2}} \quad . \tag{3.18}$$

Hence absorption by inverse Bremsstrahlung is large for long density gradients, low temperatures and high Z plasmas. The hot electron temperature that can be reached with collisional absorption scales as [22]

$$T_e \backsimeq 8(I_{16}\lambda_{\mu m}^2)^{1/3} \quad \text{in keV} \tag{3.19}$$

where I_{16} is the focused intensity in 10^{16} W/cm^2.

Although the analysis for both Inverse Bremsstrahlung and resonance absorption presented are done assuming long laser pulse ($c\tau_p \gg \lambda_L$) in a large scale length ($L \gg \lambda_L$) plasma, these results apply to certain regimes as well. According to the reference [63], Inverse Bremsstrahlung and resonance absorption can be the dominant absorption mechanisms for intensities at $10^{12} - 10^{17}\,\mathrm{W}\mu m^2/cm^2$ and the scale length as small as $0.1\lambda_L$.

3.4 Relativistic J × B Heating

This effect is an interplay between the ponderomotive force [33]

$$\mathbf{F}_p = -\frac{e^2}{4m_e\omega^2}\nabla E^2(r) \tag{3.20}$$

which causes electrons to oscillate perpendicular to the laser direction and the magnetic field **B** which comes into play for intensities $> 10^{18}$ W/$cm^2\mu m^2$. [33] Since the oscillatory motion and the magnetic eld are perpendicular, the electrons experience a force along the laser direction which is given by [63]

$$F_z = -\frac{\partial}{\partial z}\left(\frac{m_e < v_{osc}^2 >}{2}\frac{4\omega^2}{\omega_{pe}^2}e^{-2\omega_{pe}z/c}\left[\frac{1+\cos 2\omega t}{2}\right]\right) \quad . \tag{3.21}$$

This is the force felt by an electron a depth z inside the plasma. Equation 3.21 shows, that the electrons oscillate at the vacuum plasma boundary in twice laser frequency. If the magnitude of F_z is big enough, all electrons will oscillate (non-resonantly) with some electrons having the appropriate phase so that they gain energy from this oscillation before they are kicked into the

overdense plasma. $\mathbf{J} \times \mathbf{B}$ heating increases if more electrons can be accelerated, i.e. if the laser penetrates more into the overdense plasma. The skin depth can be increased either by a higher focused intensity or by an overdense plasma with lower density. The latter is reflected by the dependency of F_z on n_{cr}/n. Note that the direction of acceleration caused by $\mathbf{J} \times \mathbf{B}$ heating can be distinguished from the resonance absorption acceleration direction [12]. Usually, the acceleration direction based on the resonance absorption is normal to the solid target surface. However the $\mathbf{J} \times \mathbf{B}$ heating's is that of the laser direction, i.e., $\mathbf{k}$ direction.

In particular, the hot electron temperature of the J $\times$ B heating is scaled by Wilks [61] as

$$T_{J\times B} = 0.511 \left(\sqrt{1 + \frac{I\lambda_\mu^2}{2.8 \times 10^{18}}} - 1 \right) \text{ MeV} \tag{3.22}$$

3.5 Vacuum Heating (Brunel-type Heating)

Vacuum heating is also refered to as not-so-resonant resonance heating or Brunel effect [63] [9]. For resonance absorption a gently increasing plasma with scale length $L > \lambda_L$ is necessary so that the field can drive a large plasma wave resonantly. For vacuum heating however a the laser couples into a short scale length plasma $L < \lambda_L$ or overdense plasma interface and no large plasma wave can be driven. If the density scale length is sufficiently small, and the laser is sufficiently intense, vacuum heating occurs when the excursion of an

electron in the driven wave at the vacuum plasma interface is so large that it is literally pulled out into vacuum as see in the figure 3.5[30], then sent into the plasma with a random phase.

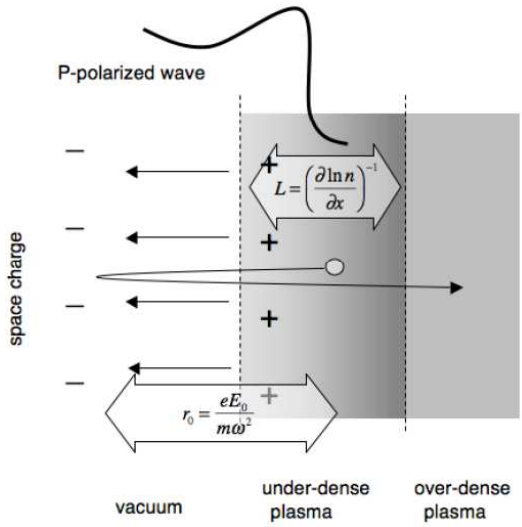

Figure 3.5: Scheme of vacuum heating mechanism. Strongly p-polarized laser pulse can directly pull electrons out of the sharp boundary of plasma and kikc them back into overdense region.

Consider a plane electromagnetic wave, with an electtric field of the form $E(x,t) = E_L \sin(\omega t - kx)$ incident on a slab of plasma with a steep density jump. Notice that a reflected wave will be present, which we will approximate as having the same amplitude as the incoming wave. This means that there will be a driving electric field of amplitude $E_d = 2E_0 \sin\theta$ that the electron on the surface of the plasma can interact with. Once the electrons are shove back into the overdense plasma, the laser field is shielded and this electrons retains a large portion of the energy they acquired from laser electric

field.

Vacuum heating is one of the important absorption mechanism for ultrashort high intensity lasers. The angular dependency of the fractional absorption is given [63]

$$f_{vh} \cong 8\frac{v_{osc}}{c}\sin^3\theta \quad . \tag{3.23}$$

In fact, Brunel empirically found that the fraction of laser energy absorbed is given by [63]

$$f_{vh} = \frac{\eta}{2\pi}\frac{v_{osc}^3}{v_L^2 c\cos\theta} \tag{3.24}$$

where η is an efficiency factor which gives a measure of how much oscillatory motion is actually lost to heating the plasma. The dependence of η on the density was found as $\eta \approx 1/(1-\omega^2/\omega_{pe}^2)$ [63].

Chapter 4

High Energy Proton Acceleration in Interaction of Short Laser Pulse with Solid Target

The generation of high current multi-MeV protons and ions by irradiation of short pulse high intensity lasers on thin targets has been observed and stuided with great interest in recent years. When a thin target is irradiated by a focused ultraintense ($> 10^{18}\,\mathrm{W/cm^2}$) laser pulse, plasma is formed on the target front surface and hot electrons are generated by the mechanisms introduced in previous chapter. The laser pushes the electrons, then these displaced electrons generate sheath field which pull on ions. Because of the ion's higher inertia, the ion response is delayed by a factor $(M_i/Zm_e)^{1/2}$ relative to the electrons, which is just the ratio of electron and ion plasma frequencies ω_{pe}/ω_{pi}. Before analyzing this process in detail, we may deduce a general point concerning laser-ion acceleration from simple physical considerations. We notice that the ion quiver motion in a laser field can be negligible compared with the electrons quiver motion which is almost speed of light, c. The ratio of electron and ion quiver velocity can be expressed as

$$\frac{v_i}{c} = \frac{ZeE}{M_i \omega c} = \frac{Zm_e}{M_i} a_0 \quad . \tag{4.1}$$

Thus, to accelerate ions to relativistic velocity ($v_i \approx c$) directly by the laser light field, we need $a_0 \sim 2000$, or $I\lambda_{\mu m}^2 > 10^{24}$ W/cm^2 μm^2 laser intensity which is still beyond the current state of the art for high power lasers.[24] In fact, electrons in a plasma mediate laser energy between the laser field and the ions by charge separation. In this chapter, Target Normal Sheath Acceleration (TNSA) which is a well known ion acceleration mechanism, is introduced using a plasma expansion model. The energy scaling law of protons accelerated by TNSA can be derived from this free plasma expansion model.

4.1 Target Normal Sheath Acceleration (TNSA)

If hot electrons can be created on the thin target front surface by ultraintense laser irradiation and their mean free path is sufficiently larger than the thin target thickness, these hot electrons can pass through the target and exit out of the target rear surface. These escaped hot electrons set up a strong sheath field on the target rear surface and ionize atoms in the sheath. Then, hydrogenated contamination materials in this sheath are ionized by the sheath field and accelerated toward the rear direction. This sheath field acceleration occurs on a length scale of 10's of microns. These accelerated protons or ions move in the direction of the quasi-static Debye sheath field formed on target rear surface which is normal to the target surface. This Target Normal Sheath Acceleration (TNSA) mechanism was first observed experimentally by

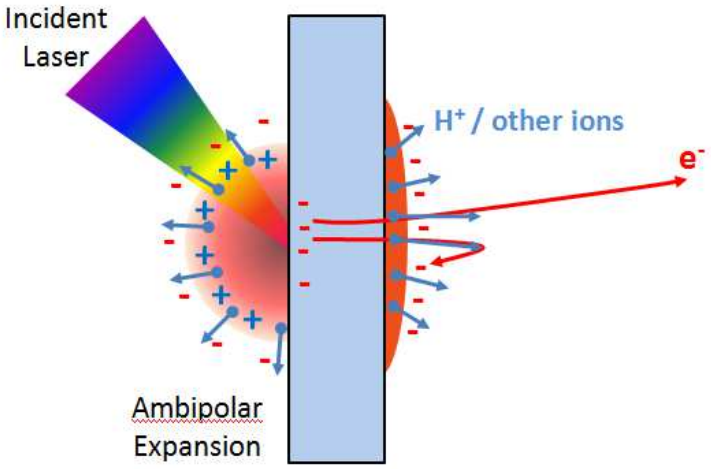

Figure 4.1: Ions can be accelerated backwards by the ambi-polar field at the front of laser-irradiated plasma plume. They can be also accelerated forward by the sheath field that is set on the target rear surface.

R. Snavely et al [57] and has been con consistently shown in mumerous other group's experimental results. Figure. 4.1 shows the schematic concept of TNSA [53]. The sheath produces quasi-static electric field given by

$$E_{sheath} \approx \frac{k_B T_H}{e\,\lambda_D} \tag{4.2}$$

where T_H is the hot electron temperature, $\lambda_D = \sqrt{(k_B T_H)/(4\pi n_e e^2)}$ is the Debye length for the hot electrons temperature and n_H is the density of the hot electrons. Typically, ℓ_D is of order a micron and temperature for the hot electrons is of order a MeV, so the quasi-static sheath fields are of order MeV/μm and so can accelerate protons to the MeV energies observed. It is important to understand that this quasi-static field is evanescent as the proton and ions are accelerated, so hot electrons co-move with protons and

ions in forward direction. Typically their number and energy ($k_B T_H$) and target capacitance are such that only small fraction escapes before the target is sufficiently charged, so that escape is nearly impossible. The remaining hot electrons then bounce back and forth, ionizing the matter as they travel.

The accelerating sheath field created by TNSA mechanism can be given roughly in equation 4.2, but more rigorous analysis about the maximum cut-off energy scaling law associated with TNSA has been studied in a free plasma expansion model [41][19]. According to ref. [41] and [19], the ion front velocity as a function of time and maximum cut-off energy of accelerated proton are given by

$$v_{front} \simeq 2c_s \ln\left(\tau + \sqrt{\tau^2 + 1}\right) \tag{4.3}$$

$$E_{max} \simeq 2E_0 \left[\log(2\tau)\right]^2 \tag{4.4}$$

where $\tau = \omega_{pi} t/\sqrt{2e}$ is the normalized acceleration time, $c_s = (Z k_B T_e/m_i)^{1/2}$ is the ion-acoustic velocity, $\omega_{pi} = (n_{e0} Z e^2/m_i \epsilon_0)^{1/2}$ is the ion plasma frequency, n_{e0} is the electron density in the unperturbed plasma, and $E_0 = (n_{e0} k_B T_H/\epsilon_0)^{1/2}$. Figure. 4.2 (courtesy of [41]) shows the sheath electric field being attenuated as it accelerates protons and ions.

If we combine the free expansion model with a hydrodynamic model, we can enhance this cut-off energy scaling law which shows good consistency with previously published data. Fuchs, et al. in the reference. [19] shows the numerical result of that combined model results consistency with previously published data taken from various laser facilities. Figure 4.3 (courtesy of [19])

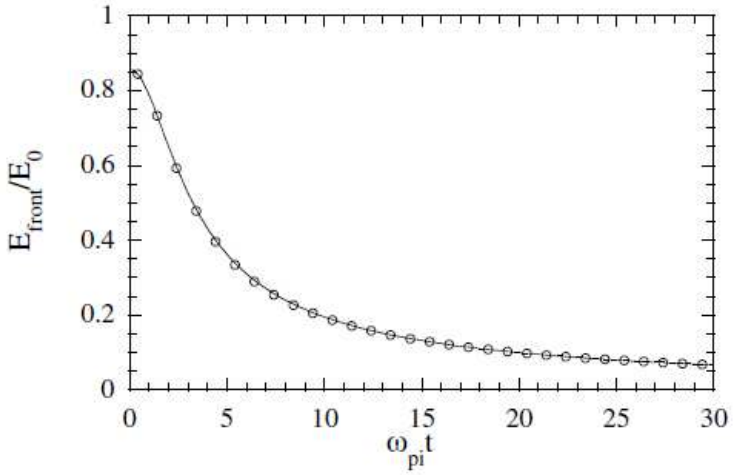

Figure 4.2: Numerical result of electric field at the ion front as a function of time. The accelerating sheath field is shown that dramatically decreased in few ion plasma time scale [41] .

shows the maximum proton cut-off energy versus the laser pulse duration, for two intensity ranges (circles and squares) together with the prediction of the fluid model for various intensities (solid line). However, it is noteworthy that this combination model also takes into consideration the attenuated sheath field. According to this reference, the effective acceleration time (or limit time) was used in this model to prevent endless acceleration by isothermal assumption. With this limited acceleration time, their numerical analysis results consistently with previously published data.

Even though many other additional effects may could be taken into account such as electron recirculation in thin foils, magnetic field effects, 3D effects, the simple plasma expansion model describes the TNSA mechanism

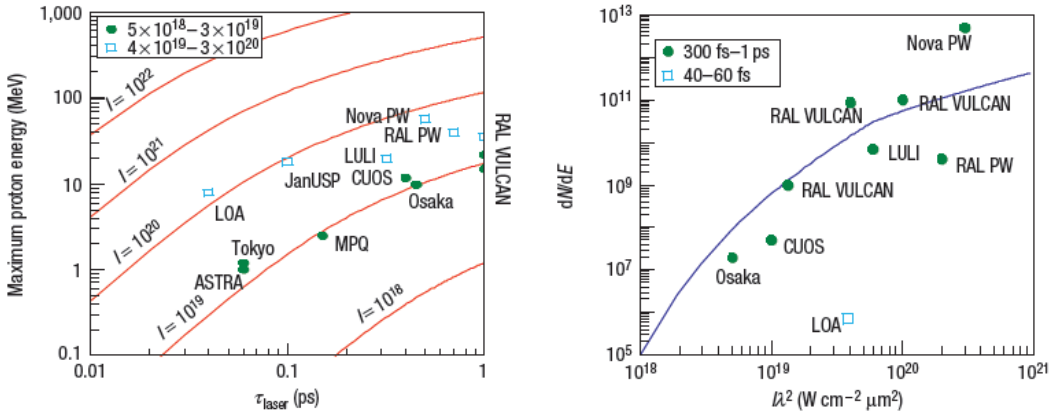

Figure 4.3: Left graph shows the maximum proton energy as a function of laser pulse duration. Laser intensities labelled on left-top corner are in units of W/cm^2. Lines present calculation for various laser intensity using free expansion model with fluid model assuming 20 μm thick target and 10μm FWHM laser focal spot. Right graphs shows number of protons in a 1 MeV bin around 10 MeV as a function of laser irradiance for same model, target and laser focal spot condition [19].

accurately and demonstrates consistency with experimental results for thick target.

4.2 Radiation Pressure Acceleration (RPA)

In TNSA, the initial cold ions are accelerated by the strong sheath field at the rear of the target. Recently, another efficient way to accelerate the ions by using the pressure of the laser light has been presented - Radiation Pressure Acceleration (RPA) [37][67][36][32][50][64][51][48]. In principle, RPA is a very efficient acceleration mechanism for obtaining monoenergetic ions beam, as the particles gain energy from the laser directly [47].

Initially, an overdense target ($n_e > n_{\mathrm{cr}}$), the target foil remains in its initial shape and the laser pulse is totally reflected. Then the radiation pressure, $P_R = 2I/c$, pushs the electrons into the target in a piston like fashion and sets up an electrostatic shock. The electrostatic space charge field pulls along the ions at the hole-boring velocity, $v_{\mathrm{hb}} \approx (2I/\rho c)^{(1/2)}$, where I is the intensity and ρ is the mass density [16][61]. If the taget is sufficiently thin so that all electrons are able to be pushed in the entire target thickness, then so called "light-sail" phase of RPA occurs, which is most efficient accelerating condition of the RPA. The equation of motion for RPA is as follows

$$\frac{dp}{dt} = \frac{2I}{c}\frac{\sqrt{p^2+\sigma^2c^2}-p}{\sqrt{p^2+\sigma^2c^2}+p} \tag{4.5}$$

where p is the areal momentum of the foil and σ is the areal mass of the foil

[50].

For a linearly polarized laser, the RPA can be expected to be dominant at I $> 10^{23}$ W/cm^2 by piston like acceleration mechanism [16]. Unfortunately, this high of intensity is still beyond current cutting-edge of the laser technology. However, it has been presented that the RPA can be dominant at the I $> 10^{21}$ W/cm^2 with a circularly polarized beam[17][50]. For circularly polarized laser, the ponderomotive force has no oscillating component. In the absence of an oscillating component of the J $\times$ B force, the generation of hot electron is strongly suppressed. In the case of circularly polarized, the electrons are pushed smoothly by the laser pressure and compressed into a highly dense layer.

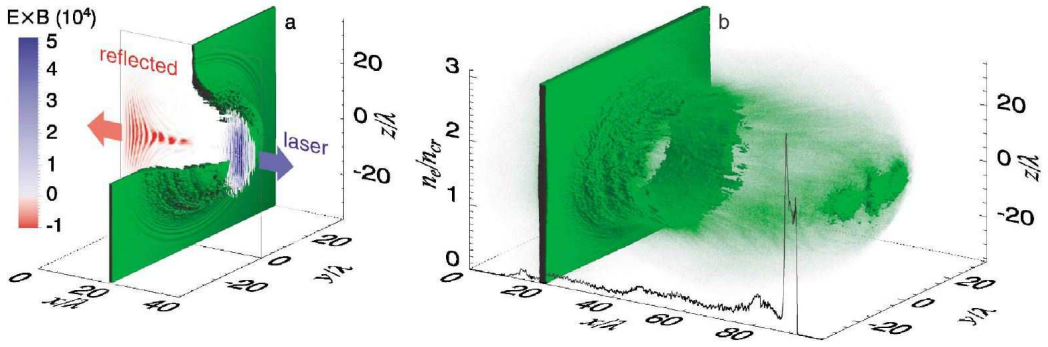

Figure 4.4: RPA PIC simulation for the $n = 8n_{\mathrm{cr}}$ (L) and $n = 2n_{\mathrm{cr}}$ (R) target [16].

Figure 4.4 shows the ion density isosurface for a RPA PIC simulation [16]. The accelerated ions form an almost flat thin plate with high density.

Chapter 5

Accelerated Charged Particle Detector

5.1 Radiochromic RCF film

GAFCHROMIC® RadioChromic Film (RCF) is designed for the measurement of absorbed dose of high energy photons or charged particle beam. RCF is composed of several functional layers and the active layer has the radiation-dose sensitive films. The sublayer of two different models of the RCF film is shown in the figure 5.1 [46]. This film is basically composed of a dye precursor disolved in a plastic host, the color develops when the film is exposed to ionizing radiation so any chemical developing is unnecessary after the radiation exposure. The color of the film changes from transparent to different shades of blue, depending on the amount of radiation (dose) that was absorbed in the film.

5.1.1 RCF Imaging Spectroscopy

The radiation exposed RCF films become quantitative data through digitizing scanner for data analysis. This can be done by transmission-densitometers, spectro-photometers or film scanners. Film scanner converts the radiochromic film to a pixel data with each pixel value representing an absorption value or optical density. Almost (90%) dyeing in RCF appears in milliseconds from

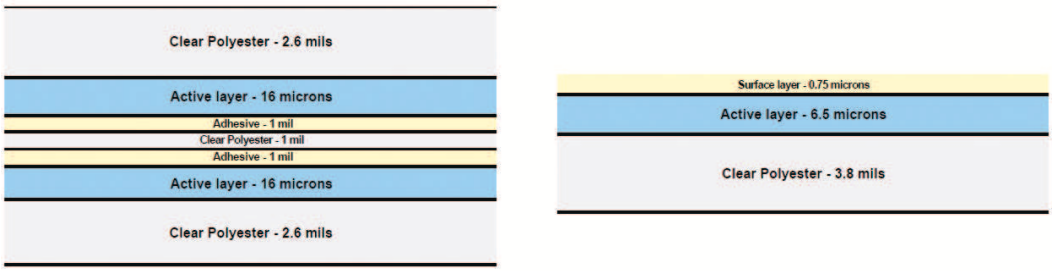

Figure 5.1: Configuration of GAFCHROMIC® for MD-55 (left) and HD-810 dosimetry films (right).

when it is exposed radiation. However, during the first 24 hours after irradiation, an increased level of dyeing can not be neglected. Thus, it is recommended to let the film stabilize for two days after irradiation before scanning and digitizing [44][29]. Calibration for GafChromic film is well known and readily available from Hey. et al. [29]. Figure 5.2 cited from this reference shows the calibration results for dose and net OD. This figure shows that the net OD starts to saturate as it approachs two even if a higher dose is accumulated in the film. The dose curve shows that HD-810 type of RCF film is less sensitive than the MD-55 or HD types. For both MD-55 and HS type films a lower deposited dose induces the same OD as for type HD-810. Thus, MD-55 and HS type can be used for the detection of lower fluxes as the energy deposition of each particle is higher than in the HD-810 type film. The fitting formula for this calibration is given by Hey et al. [29].

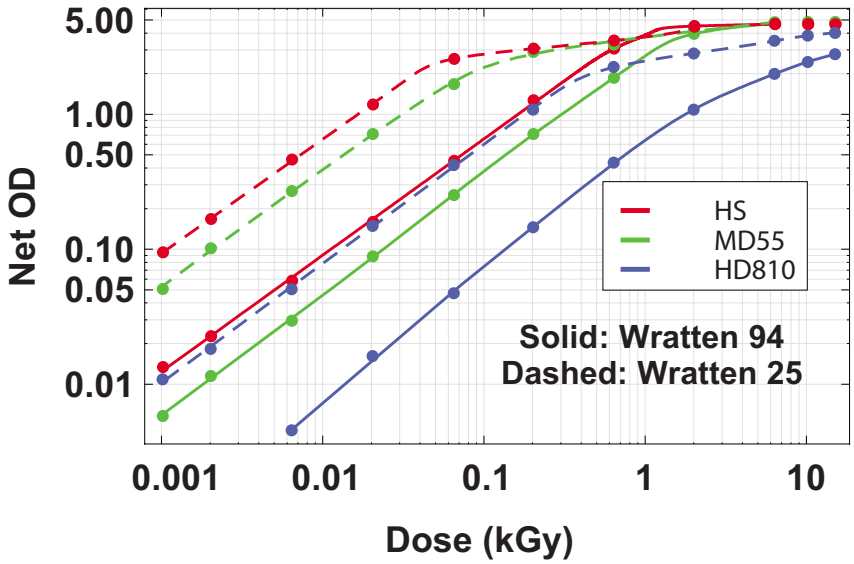

Figure 5.2: Dose response curves for three different types of RFC.

The film can be scanned with a 16 bit scanner. During image processing, it is better to read the red channel of image because RCF film absorbs light at 600 nm more effectively. The scanning signal can be converted into OD by the following formula

$$\mathrm{OD} = -\log\left(\frac{i}{2^{16}-1}\right) \tag{5.1}$$

where i is the pixel value of red channel in 16 bit. But this formula should be calibrated in each scanner. We have calibrated the Konica Minolta DiIMAGE Scan Dual IV film scanner with a certified transmission step wedge (T4110cc, Stouffer Industry, Inc.) and the result is shown in the figure. 5.3.

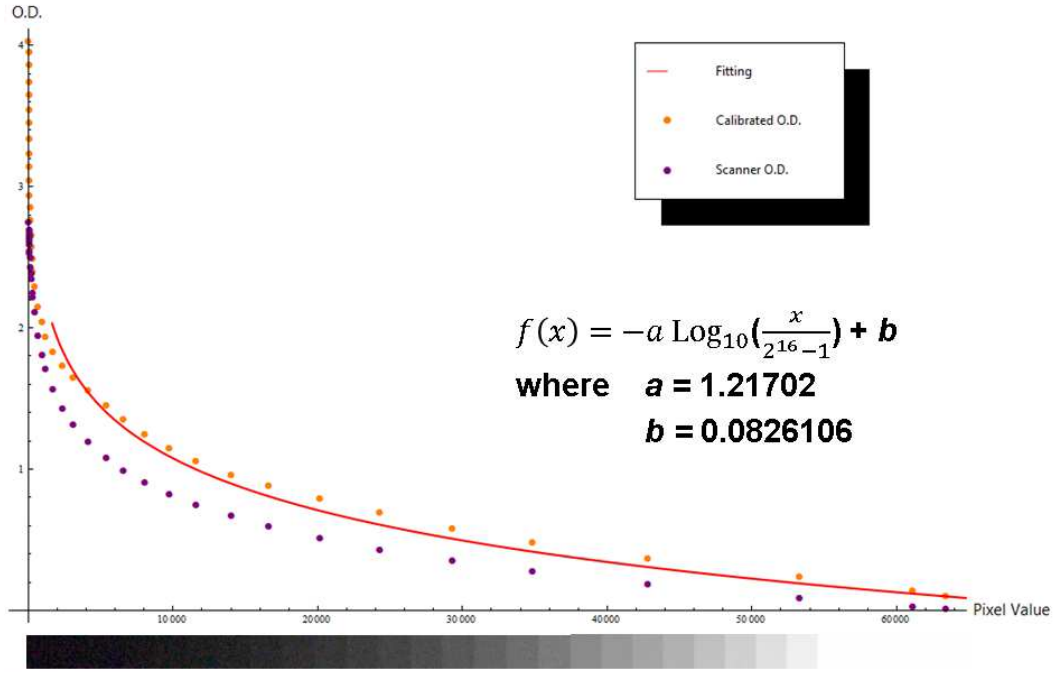

Figure 5.3: OD calibration for the Konica Minolta DiIMAGE Scan Dual IV film scanner.

5.1.2 Stopping Power

To estimate the cut-off energy of the proton beam with RCF film stack quickly, we can use the stopping power calculation. When an ion beam propagates in matter, it looses its energy by interaction with the atoms in matter. The differential energy loss or stopping power, i.e., the infinitesimal energy fraction dE lost by the particle on its infinitesimal travel fraction dx, is described by the Bohr-Bethe-Bloch equation, with some correction factors depending on the initial energy and projectile type. An unique property of the

ion energy loss characteristics is the increase of dE/dx towards the end of the range, with a global maximum just at the end of the range where the particle is stopped. The continuous model of the stopping power for non-relativistic particles is given in equation 5.3 and for relativistic particles is given in equation 5.2

$$-\frac{dE}{dx} = \frac{NZ^2e^4}{4\pi\varepsilon_0^2 m_e v^2} \cdot \ln\left(\frac{2m_e v^2}{I}\right) \tag{5.2}$$

$$-\frac{dE}{dx} = \frac{NZ^2e^4}{4\pi\varepsilon_0^2 m_e c^2\beta^2} \cdot \left[\ln\left(\frac{2m_e c^2\beta^2}{I\left(1-\beta^2\right)}\right) - \beta^2\right] \tag{5.3}$$

where number density N, charge Z, energy E, traveling distance x, experimental mean inelastic scattering energy I, the speed of light c, vacuum permittivity ε_0, $\beta = v/c$, electron charge e and rest mass of the electron m_e [56].

Figure 5.4 shows the Bragg peak of the 5.49 MeV alpha particles in the air. The Bragg-Peak is a result of the projectile velocity and target electron velocity in the atom shell approaching the same value, enhancing the energy transfer from projectile to target. RCF is sensitive to all ionizing radiation, but it is most sensitive to protons due to their higher stopping power compared to electrons or x-rays. Heavy ions usually penetrate the first layer only. The entrance of RCF stack holder is usually blocked by aluminum foil to shield the stack from radiation and target debris.

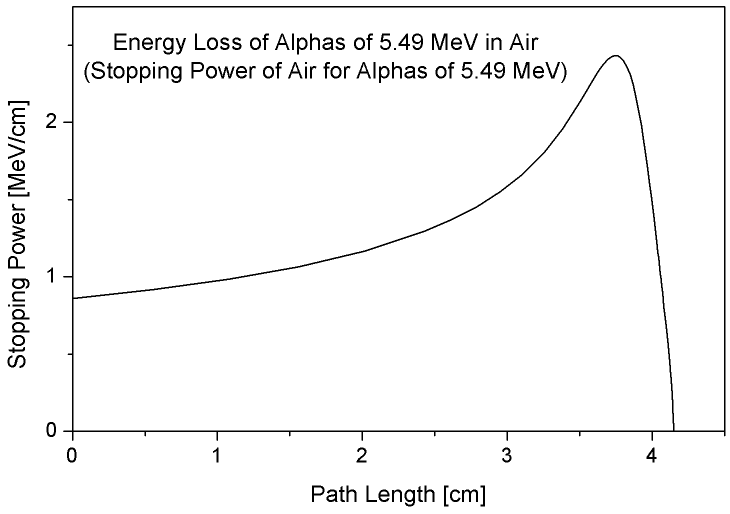

Figure 5.4: The Bragg curve of 5.49 MeV alpha particles in the air [1].

SRIM and TRIM are collections of software packages that can calculate features of the ionizing radiation of ions in matters and assist to diagram the Bragg peak and stopping power for materials. Figure 5.5 shows the proton trajectories in a stack that is bombarded from the left as they pass towards the right. A 25 μm thickness Al foil is placed on the left side for the debris shielding, with a HD-810 RCF stack placed afterwards. The protective layer in the RCF is relatively thicker than active layer resulting in a $\pm$ 1 MeV error of the proton energy when reading the developed RCF film itself.

Figure 5.6 shows the RCF data of the TPW commissioning shot #2118 with a 5 μm thickness Ti target and figure 5.7 shows the Bragg-peak of the stack generated by TRIM.

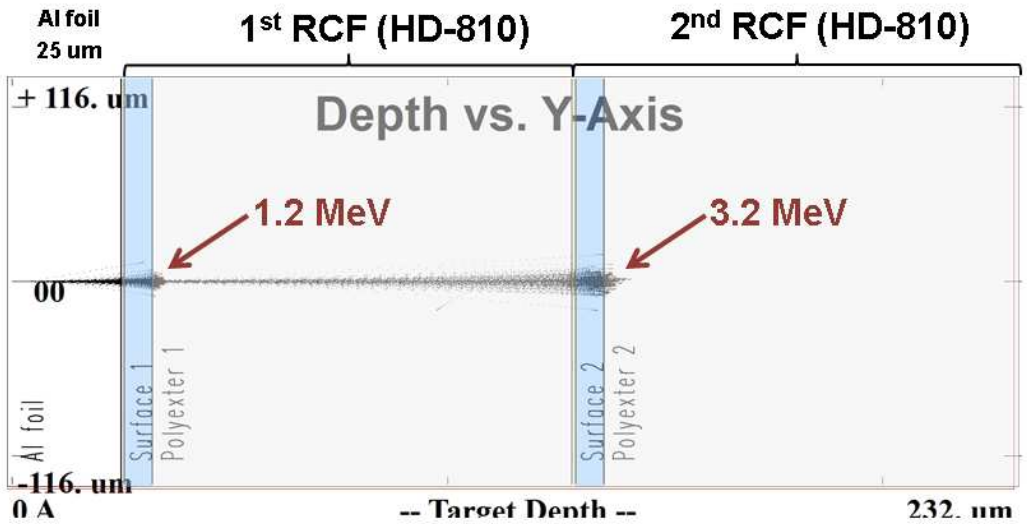

Figure 5.5: SRIM stopping power simulation of the RCF stack with the proton beams.

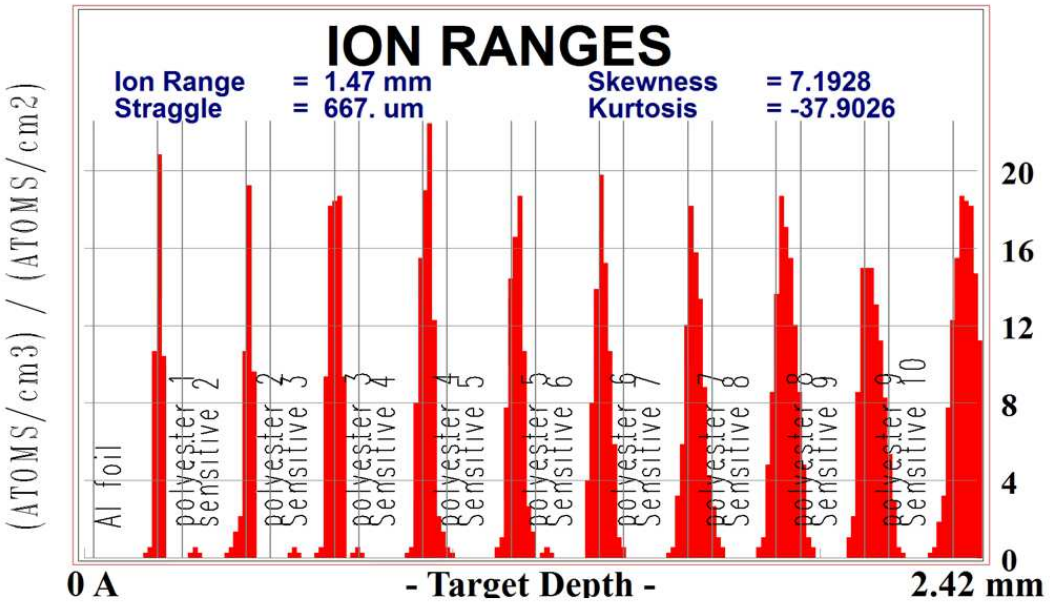

Figure 5.7: Bragg Peak for the RCF HD-810 stack from the shot shown in figure 5.6.

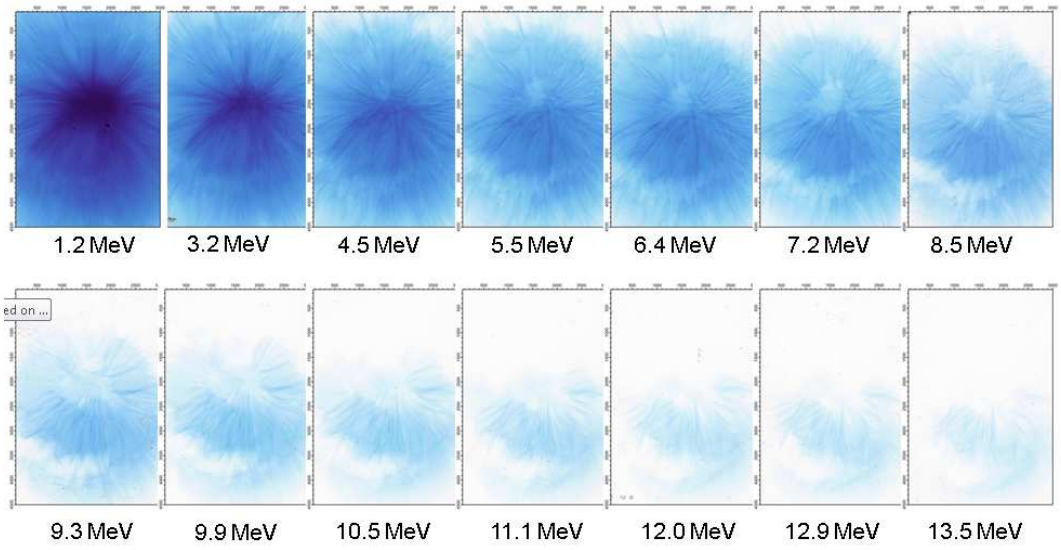

Figure 5.6: RCF data of the TPW commissioning shot. #2118 on a 5 μm Ti target.

Each subsequent layer in a stack has a lower detection threshold where the energy deposition quickly rises and then slowly falls off, representing an inverse Bragg-curve. MD-55 type film has two peaks because of the two active layers in the film. The total energy deposition in the MD-55 type is higher than in the HD-810 type due to the thicker active layer. Because of this peaked energy deposition profile, each RCF layer can be attributed to a small energy interval with a width of approximately 1 MeV for the MD-55 type and 0.5 MeV for the HD-810 type. Hence, the stack of RCF layers can be used as a 2-D imaging spectrometer, measuring the transverse intensity distribution in the two transverse dimension and the energy-resolved particle spectrum in the third longitudinal dimension.

5.2 Phosphor Screen Image Plate

The Phosphor Imaging Plate (IP) contains a phosphor layer of fine-grained, BaF_2 (Barium Fluorohalide) crystals doped with a divalent Europium (Eu_2^+). Figure 5.8 shows the composite structure of the IP screen [54]. When the IP screen is exposed to radiation such like x-ray, excited electrons are trapped in the halide vacancies to form a color centers. This excitation results in holes and leads to change of Eu_2^+ to Eu_3^+. This latent image is stable for up to several days.

Approximately 80% of stored signal in the IP is released upon scanning. The remaining signal must be erased before the reusing. By exposure with light wavelengths of 475 $\sim$ 650 nm, the signal in the IP is erased effectively. For example, using a 500 W photoflood tungsten light bulb and a yellow filter (Wratten 16), an exposure of 10 J/cm^2 will leave a residual signal level of less than 10-5 of the original exposure level in 10 minutes [55].

The calibrations of these IP with well known methods are available in reference [11], [66], [58].

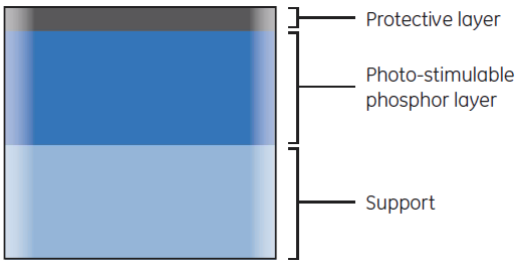

Figure 5.8: Composite structure of Storage Phosphor Screen BAS-IP.

5.3 Thomson Parabola Spectrometer

A Thomson parabola spectrometer is a detector which gives the energy spectrum of the charged ion particles. As shown in the figure 5.9, an E-field is applied parallel with a B-field, so that charged particles in that region deflected not only in the vertical direction by the E-field, but also deflected in the horizontal direction by the B-field. These deflections lead to a parabolic trace of the particles in terms of each particles energies on the detector at the rear of the spectrometer. Different ion species leave different parabolic traces according to their q/m ratio.

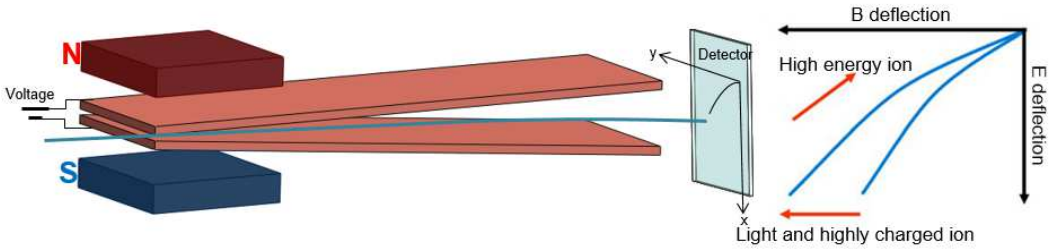

Figure 5.9: Diagram of Thomson parabola spectrometer where the magnet plates and elecstrodes are shown.

Theoretical modeling of the spectrometer design is done with the particle tracking code SIMION. Figure 5.10 shows the SIMION simulation for different energies of proton beams incident on the spectrometer. The electrode gap is gradually widened, so that the low energy particles that are deflected by large angles are not blocked by the other electrode plate so that and they can arrive to the detector at the rear of the spectrometer.

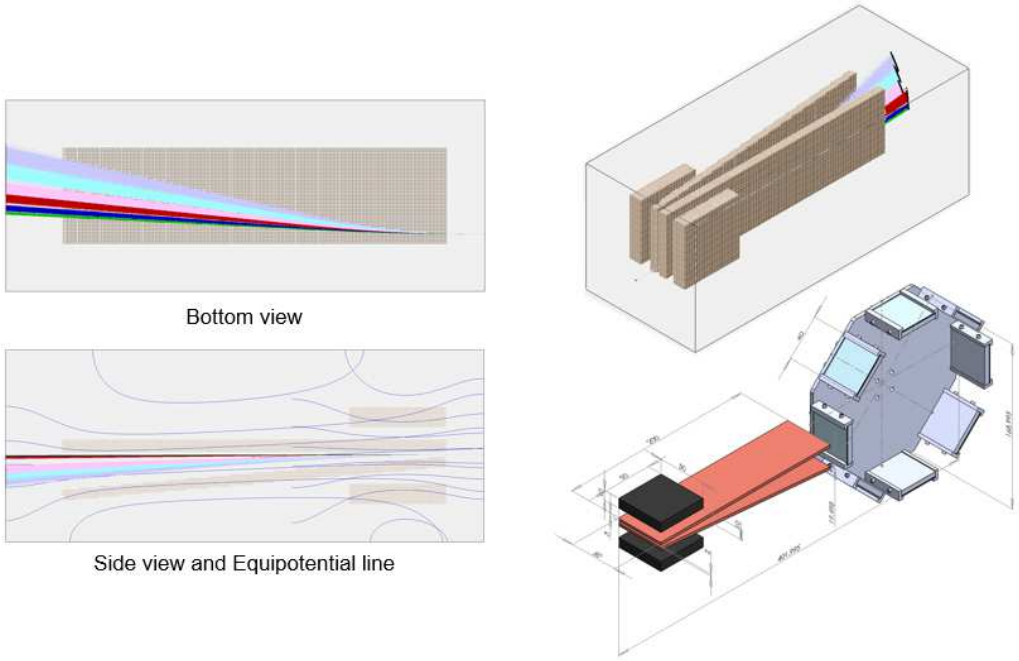

Figure 5.10: Particle tracking study of the Thomson spectrometer with SIMION and solidwork design.

The spectrometer is designed and machined by the Ohio State University group and a detailed description of the design is given my Morrison, et al. [42]. As shown in the figure 5.12, the image plate holder is able to hold 4 pieces of the Phosphor screens and switch them for different show by rotating the holder. The spectrometer is aligned by aligning a HeNe laser from the neutral particle trajectory on the back plate of the Thomson and through the pinhole in the front shielding block. As shown in the figure 5.12, a well aligned HeNe laser creates an Airy pattern when it passes through the pinhole. A 1-inch thickness stainless steel is placed in front of the spectrometer to block the

gamma-ray radiation from the plasma.

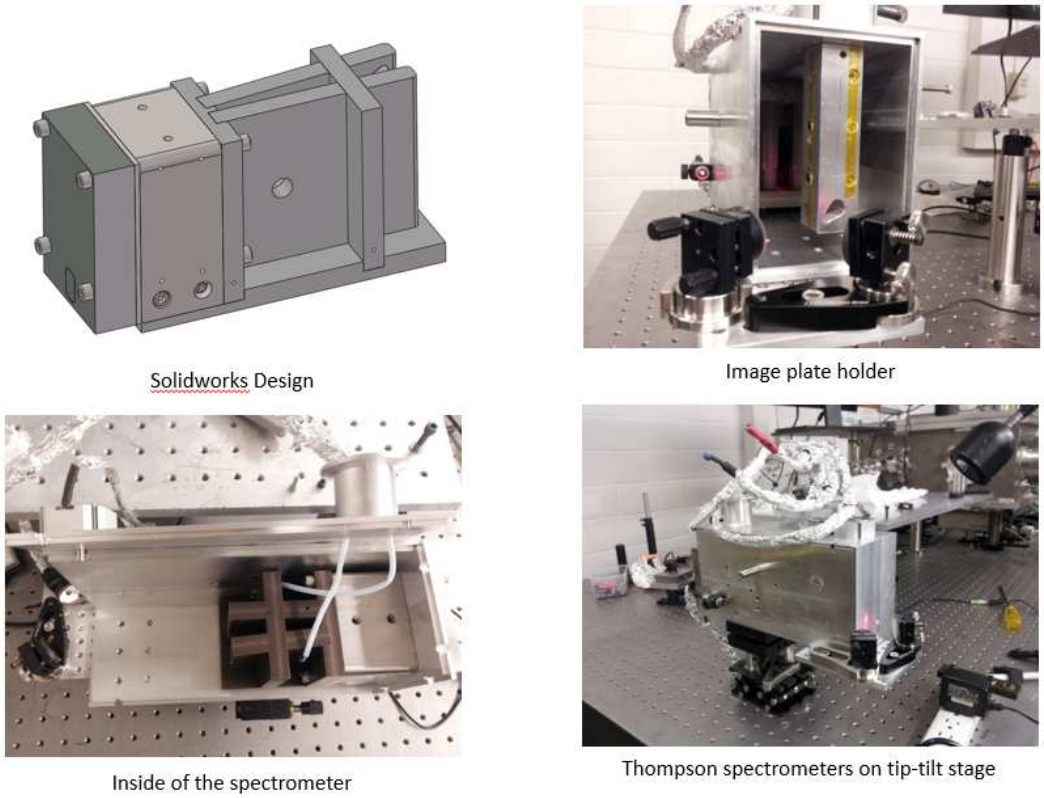

Figure 5.11: Machining of the Thomson spectrometer.

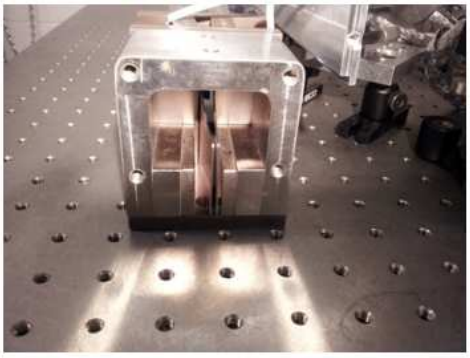

1.5 Tesla Niobium magnet

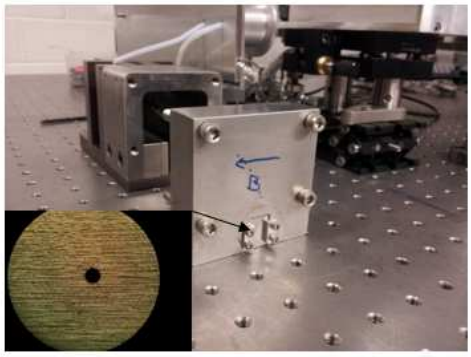

Φ = 200 μm pinhole on the gamma-ray blocker

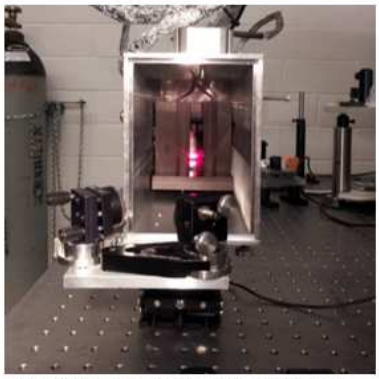

HeNe laser is used for the alignment

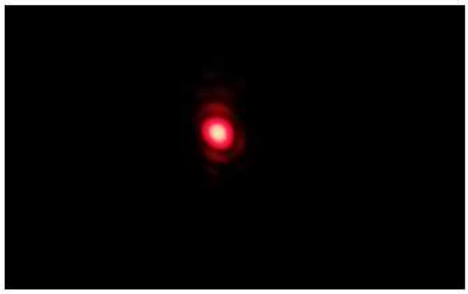

Airy pattern of the alignment HeNe laser

Figure 5.12: Radiaion shielding block and pinhole of the Thomson spectrometer.

Figure 5.13 shows the test setup for the high voltage power supply and measurement of the applied voltage on the electrode. Figure 5.14 shows the scanned Phosphor screen image plate data and the Matlab analysis code.

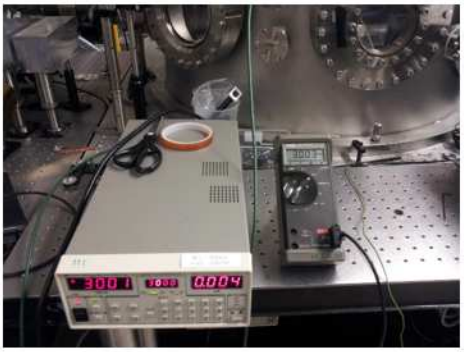

Setup for the High Voltage Probe in vacuum

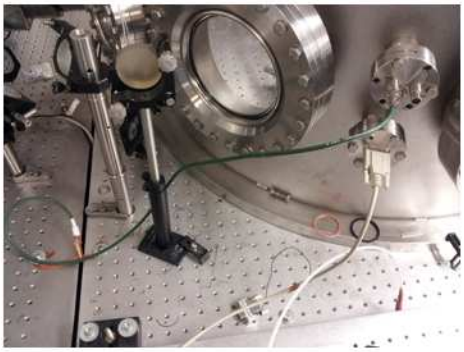

Grounding and image plate rotator feedthrough

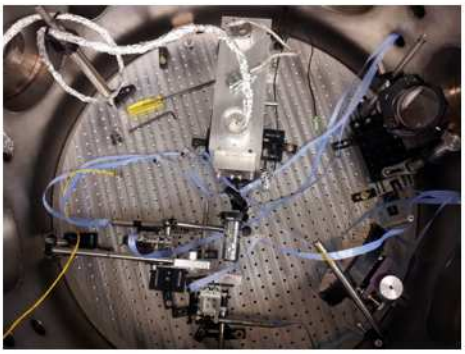

Thompson spectrometer in the vacuum chamber

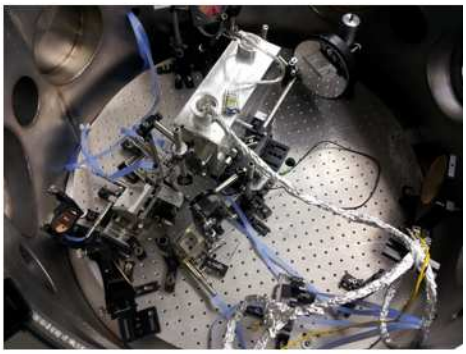

Thompson spectrometer in the vacuum chamber

Figure 5.13: HV test of the Thomson spectrometer in the vacuum.

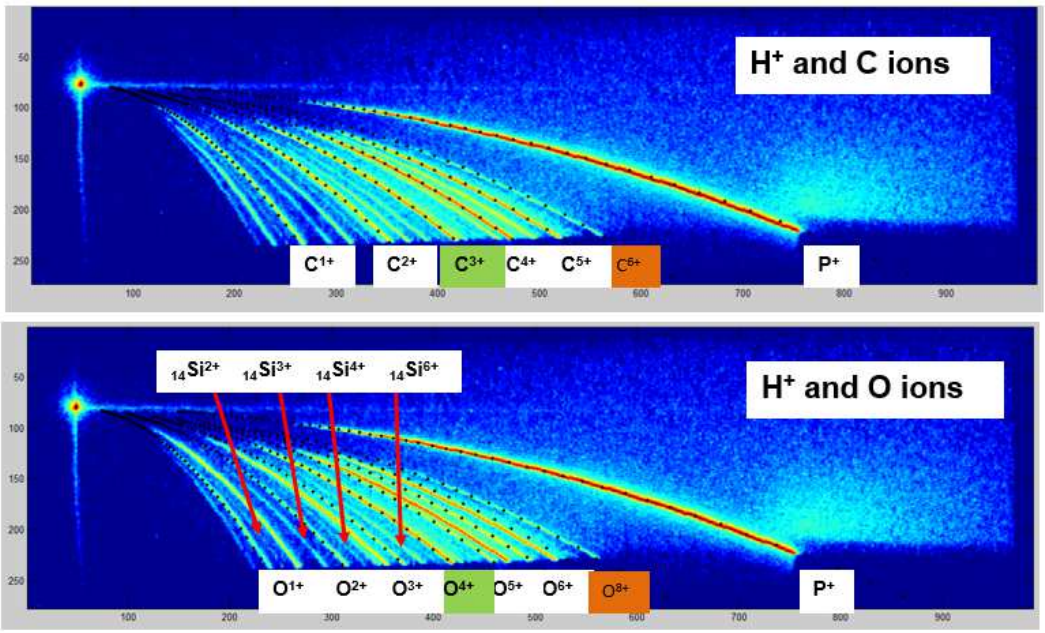

Figure 5.14: Particle parabolic trajectories and data analysis with the matlab.

5.4 Electron Spectrometer

The detection of the negatively charged particle is incompatible with the Thomson parabola spectrometer as they are deflected to the opposition direction. The light mass of the electron results in the electrodes and magnet being deflected intensionally while the flight and it can not reach to the detector. Therefore, we need another spectrometer that is designed to detect negatively charged particle. Figure 5.15 shows the electron spectrometer used with a pair of 0.15 T magnets. The pin-hole side on the incident side of the detector is shielded with a piece of lead to protect the image plate from

radiation.

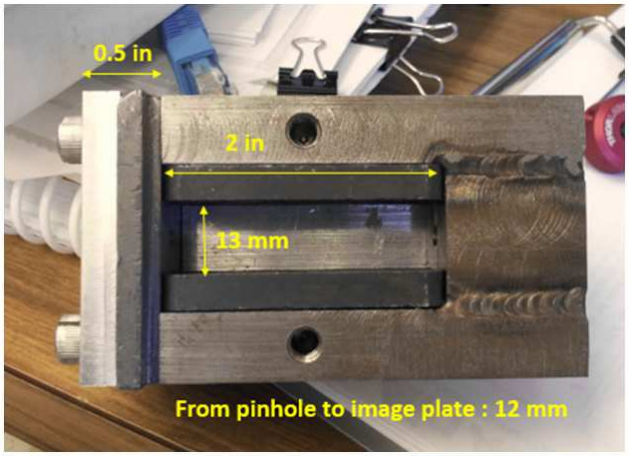

Figure 5.15: Electron spectrometer.

The electrons are easily gain energy from the laser and become relativistic, so the spectrometer should be calibrated to account for the relativistic deflection given by the Larmor radius R given by [58]

$$R = \frac{m_o c}{eB}\sqrt{\left(\frac{\varepsilon + m_o c^2}{m_0 c^2}\right)^2 - 1} \tag{5.4}$$

where R is the relativistic Larmor radius for electrons with energy ε in the magnetic field B.

For calibration process, ^{90}Sr is widely used for the electron beam source as it is almost pure beta particle source for its radioactive decay. Figure 5.16 shows the β^- decay process of the ^{90}Sr [2].

^{90}Sr undergoes β^- decay with a half-life of 28.79 years and a decay maxinum energy of 546 keV and mean energy of 196 keV distributed to electrons.

Then the daughter producer ^{90}Y undergoes β^- decay again with half-life of 64 hours and decay maximum energy of 2.28 MeV and mean energy of 927 keV distributed to electrons, and becomes stable ^{90}Zr. The gamma photon emission from the decay of ^{90}Y can be ignored as it is so infrequent. A schematic of this decay process is shown in the figure 5.16.

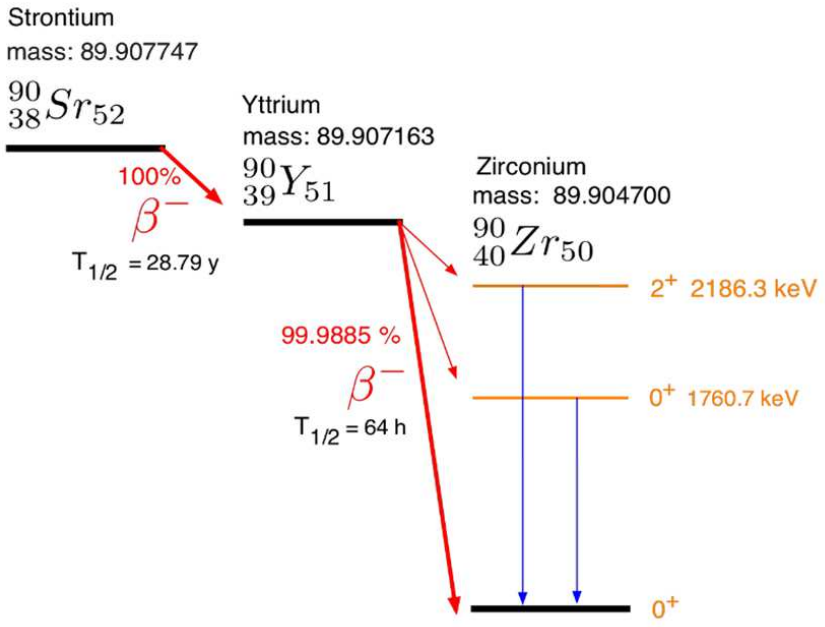

Figure 5.16: β^- decay scheme of the ^{90}Sr.

For calibration, spectrometer is exposed for 5 hours in a 10^{-5} Torr vacuum and then the image plate is scanned immediately. Figure 5.17 shows the result of the calibration data. Two peaks are observed each of them corresponding to each β^- decay process's mean energy. From this data, the electron spectrometer is numerically calibrated using a 2nd-order polynomial. The re-

sults of this calibration and the coefficients of the each term are shown in the figure 5.18.

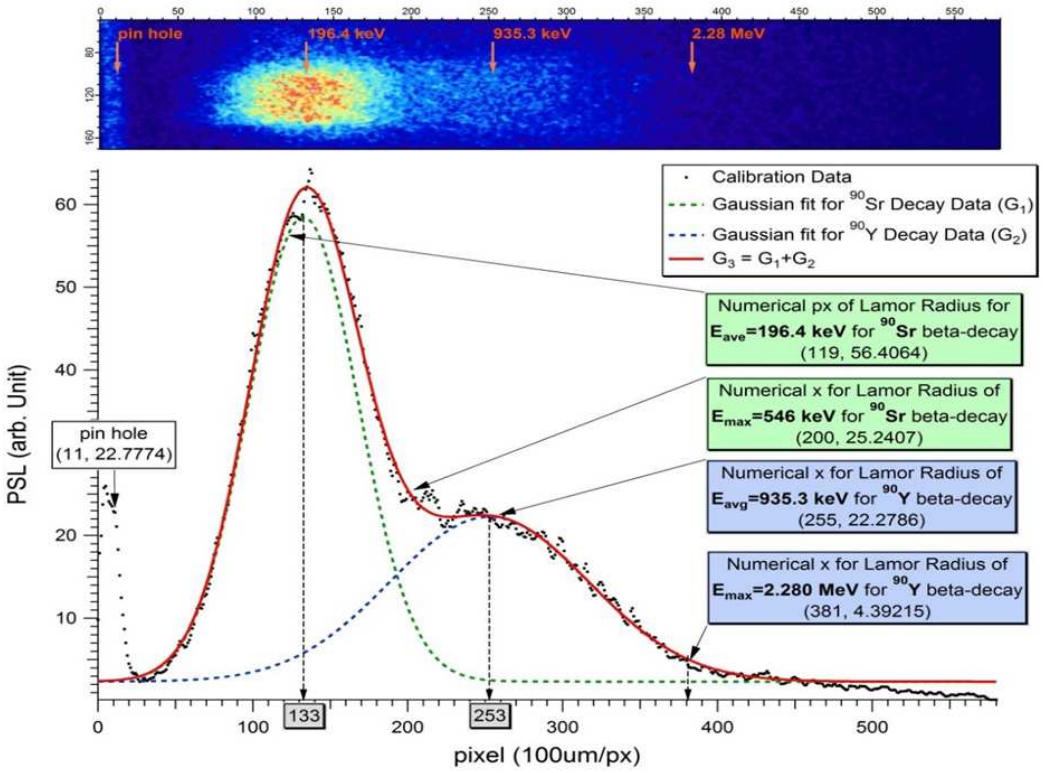

Figure 5.17: Calibration curve of electron spectrometer using a ^{90}Sr source.

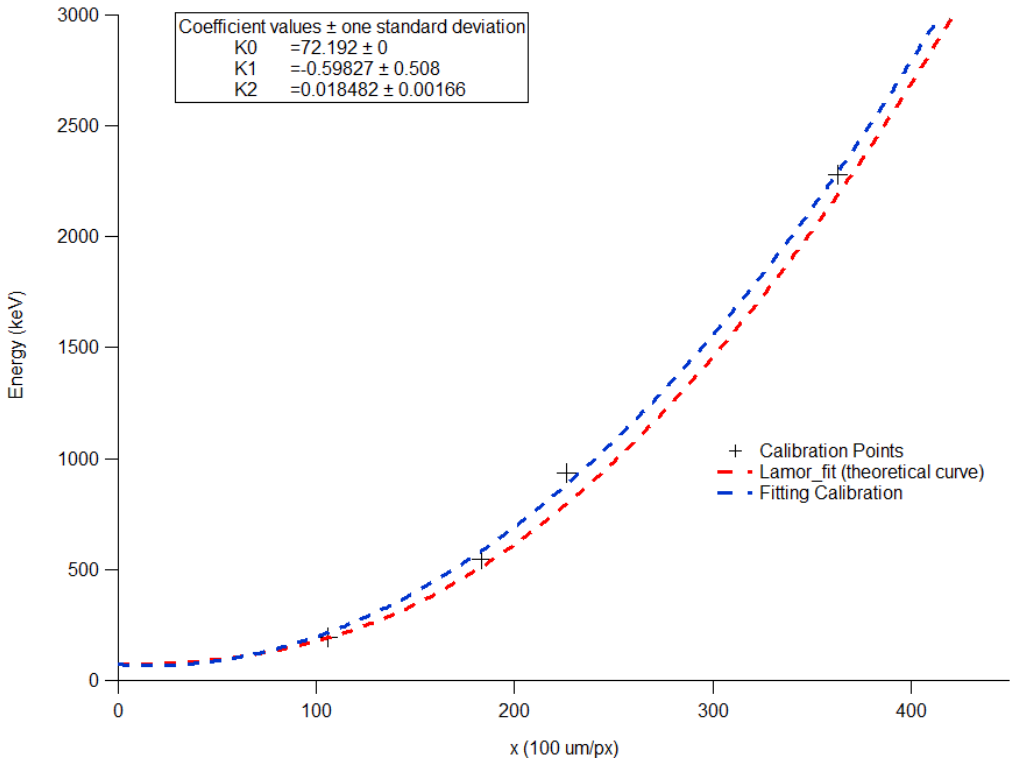

Figure 5.18: Calibration curve fitting with the Larmor curve of data shown in the figure 5.17.

Chapter 6

Experimental Setup and Data

In this chapter, we introduce 2 different laser facilities and the experimental setup for the laser driven proton acceleration that is carried out at each facilities.

6.1 Laser System

6.1.1 GHOST Laser

The Glass Hybrid OPCAP Scale Test (GHOST) Laser system had been developed as a preliminary investigation laser for the Texas Petawatt Laser. The main amplification stage after the OPCPA stage is composed of 2 glass rods of Nd:Phosphate hybrid and Nd:Silicate. This 2 different amplification media amplify the the laser in a slightly different peak wavelength so that can minimize the gain narrowing in the chain of the amplification.

The Coherent Verdi laser produces 75.6 MHz train of 2.7 nJ pulse in 95 fs FWHM pulse duration centered 1055 nm in FWHM. This oscillator beam is selected at 10 Hz while it go though the Pockels Cell which rotate the polarization by 90 degrees and delivered to the grating beam stretcher to stretch the beam to 1 ns. 2 paris of BBO crystals compose the OPCAP

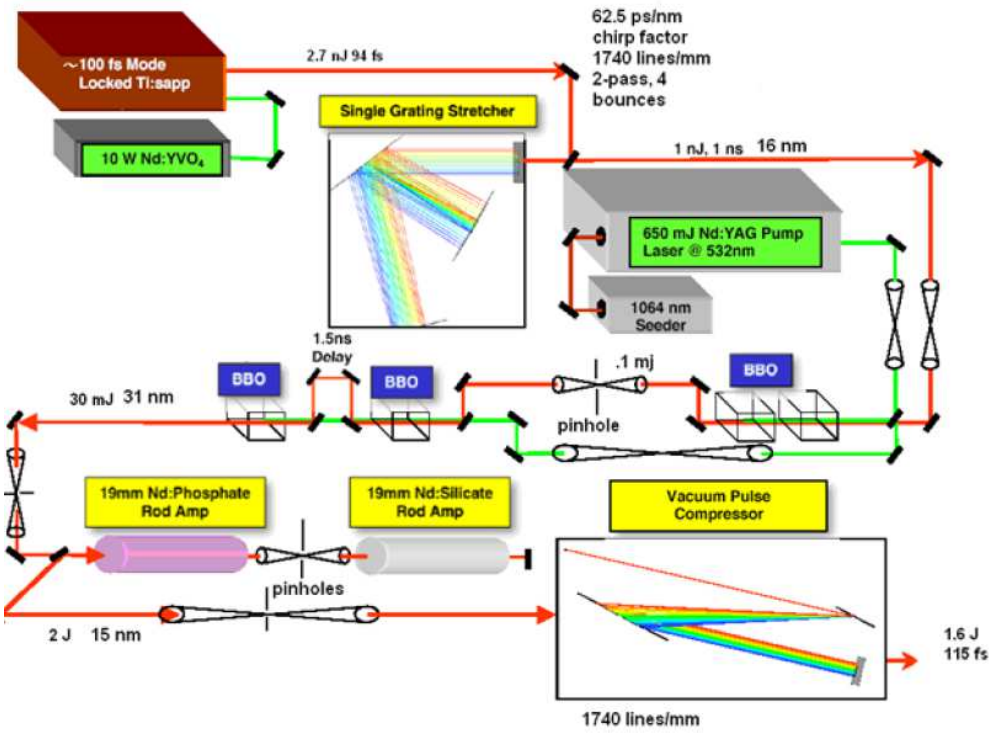

Figure 6.1: The layout of the GHOST Laser.

stage to preamplify the stretched beam up to level of mJ. 532 nm Q-switched Nd:YAG pump laser is synchronized from the front-end photodiode signal and pump the BBO crystals to amplify the oscillator beam. The beam amplified at the first stage is cleaned as it go through a pinhole placed after the first stage, so selected mode of the Gaussian beam is delivered to the 2nd stage. This OPCAP beam is magnified through a telescope and delivered to the main amplification stage of the hybrid glass rods. Both rods are flash lamp pumped by the Pulse-Forming Network (PFN) that is composed of capacitor bank

and amplify the laser up to 1.8 J. A $\phi = 45$ mm isolator is installed before the compressor chamber to prevent any damage on the upstream optics by reflected beam from target chamber.

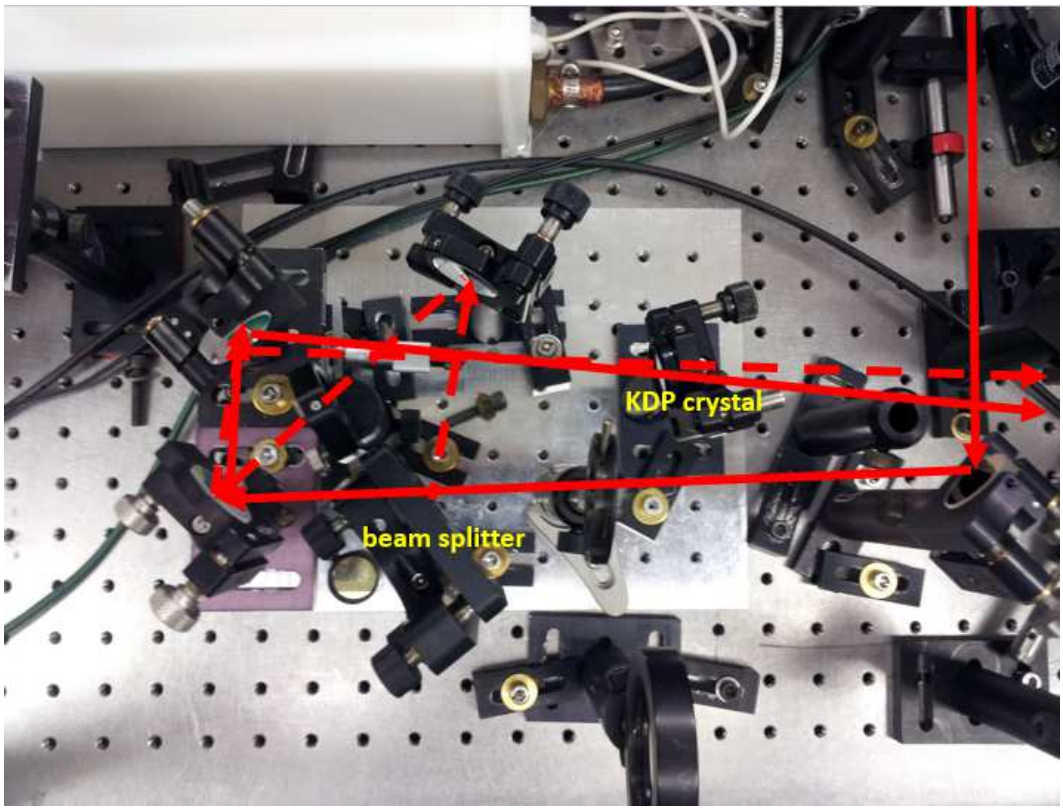

Figure 6.2: GHOST 2nd order autocorrelation stage.

In the last stage, 2 multilayer dielectric gratings in vacuum chamber is designed to compress the laser beam in double pass. The compressor transmits 65% of the incoming beam to the switch yard. To measure the pulse duration of the compressed beam, a leaked beam of the compressed chamber is relayed to the 2nd order autocorrelation stage to the outside of the chamber. The 2nd

order autocorrelation stage is designed with a KDP crystal which generates 2nd harmonic laser beam when the autocorrelation is occurred in it. By measuring the time integrated intensity product of the 2nd harmonic beam, we can calculate the pulse duration of the compressed beam. Figure 6.2 shows the beam path on the autocorrelation stage and figure 6.3 shows the 2ω beam image on the camera. Detailed calculation is referred to the appendix.

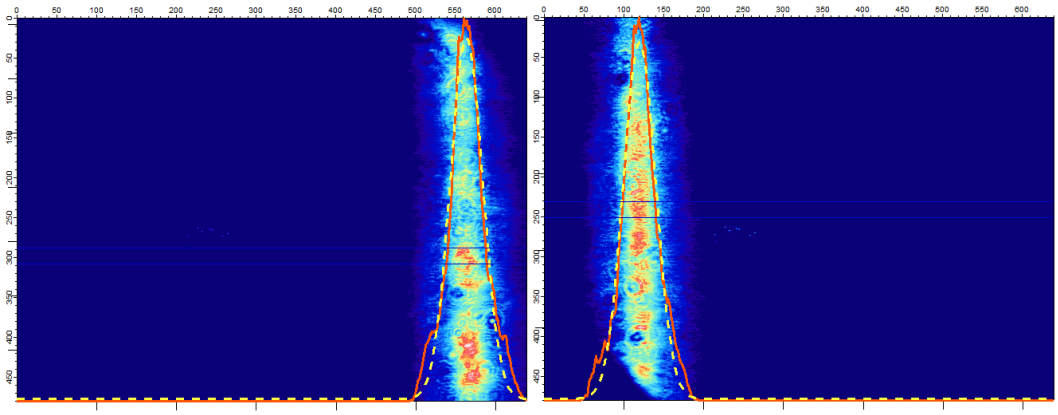

Figure 6.3: GHOST 2nd order autocorrelation calibraion image.

6.1.2 Texas Petawatt Laser

The Texas Petawatt (TPW) Laser system delivers 100 J at 110 fs in FWHM laser beam based on Optical Parametric Chirped Pulse Amplification (OPCPA) with mixed Nd:glass amplification heads. In 2011, the Texas Petawatt Facility commissions Target Chamber 1 (TC1) on its target bay section. A fast focus $f/3$ off axis parabolic (OAP) mirror which can focus the laser up to 10^{21} W/cm^2 is installed in the TC1 to utilize for solid-target

experiments.

The layout of the TPW chain is shown in the figure 6.4[4]. The chain begins with a 100 fs pulse from a tunable, Ti:sapphire oscillator. The pulse is stretched to 2 ns in a stretcher using a modification of the design of Banks [21]. Following 3 broadband OPCPA stages consist of BBO, YCOB amplifies the pulse and delivers the pulse to into downstream Nd:glass amplifiers. The first Nd:glass amplifier consists of a 64 mm diameter silicate rod amplifier and its peak fluence is under 1.5 J/cm^2 to avoid damage and to keep the system B-Integral below 1. After 8 passes amplification on this stage, the pulse delivered to 315 mm phosphate disk amplifier stage for 4 passes amplification. Amplified pulse beam is delivered to grating compressor chamber and compressed when it passes two 40 $\times$ 80 cm^2 multilayer dielectric diffraction gratings, and then finally 100 J at 110 fs beam is directed into target chambers. 2-nd order auto correlation system, far field and near field diagnostics and wave front sensor (WFS) correlated with deformable mirror that are designed to diagnose and feedback for of beam quality enhancement.

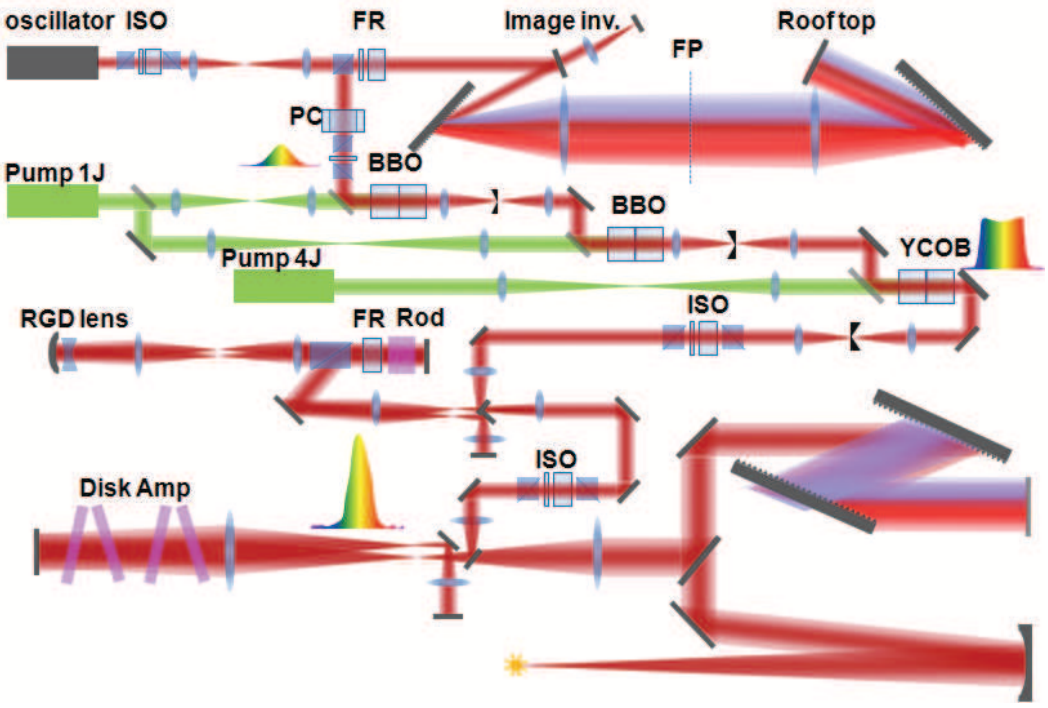

Figure 6.4: The laser layout of the Texas Petawatt Laser.

6.2 Micro-structured Target Experiments at the TPW

6.2.1 Motivation

In TNSA, a quasi-electrostatic field is produced on the target rear surface when the ultra-short and ultra-intense laser interacts with solid density target, driving hot electrons go torward the target rear surface. The quasi-electrostatic field produced by these hot electrons accelerates ions from the target rear surface [26][62][57][13][20][27]. Typically this mechanism results in a range of field gradients leading to a broad proton energy distribution. To mitigate this ion energy spread, micro-structured targets, or micro-dot targets

have been presented as a facile method to achieve a quasi-monoenergetic proton energy spectrum [53]. Micro-structured dot composed of hydrogen rich material have the potential of enriching the proton source in a spatial region that is coincident with the laser focal spot and can, therefore, sample only a small region of the various field gradients set up by the cloud of hot electrons. Experiment presented in ref. [53] indicated that such micro-dot target could produce fairly monoenergetic proton distributions at 1 MeV energy with modest intensity ($\sim 10^{19}$ W/cm^2). We have attempted to confirm this early result and scale it to higher laser intensity using a petawatt laser pulse.

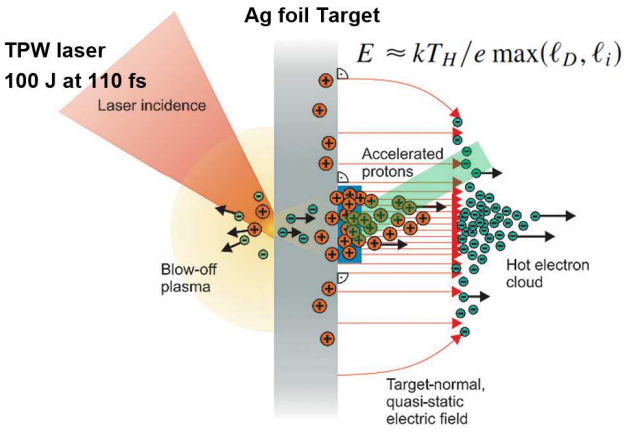

Figure 6.5: Conceptual scheme of the micro-structured target experiment. Micro-dot can be aligned with the main focal spot and the abliation laser. [53]

6.2.2 Microstructured Target Fabrication

The micro-structured dots are fabricated on 800 nm thickness Ag foil. By using water soluble synthetic polymer of the 1% Polyvinyl Alcohol (PVA),

we can make water floatable thin film on the substrate. Figure 6.6 shows the fabrication process.

1. PVA spin coating
    (a) 3000 rpm, 60 sec
    (b) Hard baking (110 °C, 5 min)
2. Thermal evaporation deposition of the Ag
3. Photoresist (PR) spin coating
    (a) Mix Rhodamine 6G 100 g with 400 $\mu\ell$ water
    (b) Mix it with AZ-5209E PR
    (c) 3000 rpm, 60 sec
    (d) soft baking (90 °C, 90 sec)
4. Photolithography
    (a) soft contact, 20 sec exposure
5. Developing
6. Hard baking
    (a) (120 °C, 3 min)
7. Water floating

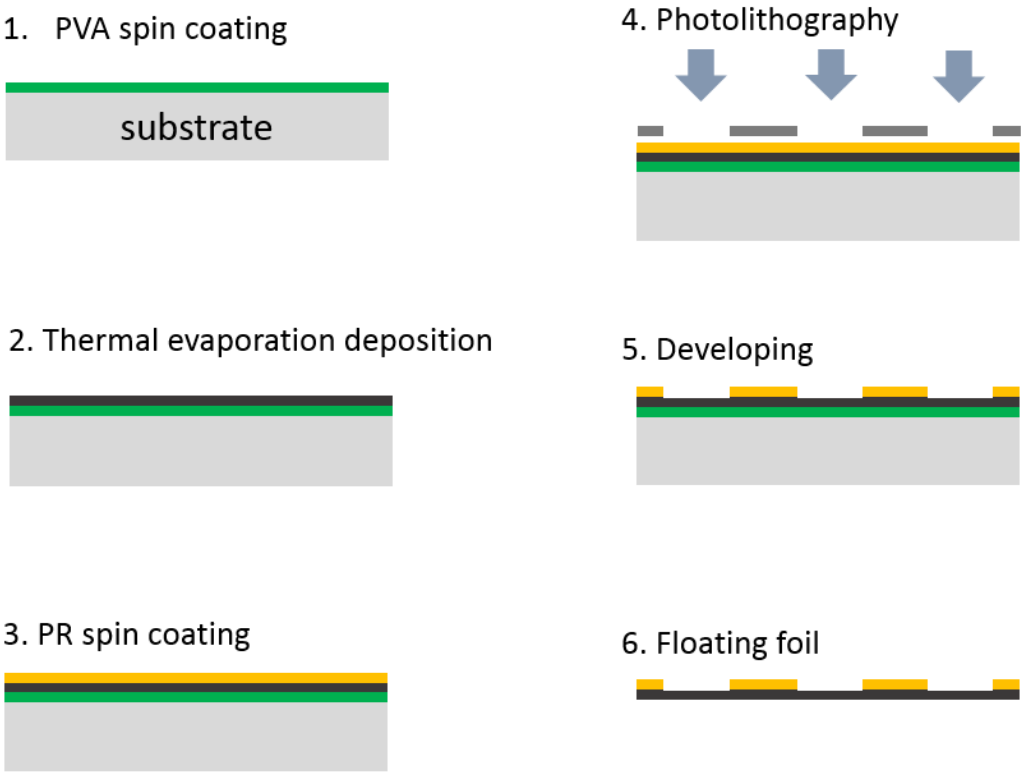

Figure 6.6: Micro-dot target fabrication process

The PR is a polymer containing rich hydrogen in the carbon chain. Rhodamine 6G which absorbs the 532 nm and emits 550 nm wavelength light is selected for the laser dye with the PR. Figure 6.7 shows the absorption and emission spectrum of the Rhodamine 6G [35]. By mixing it with the PR, the micro-structured dot is aligned to be coincident spatially with PW pulse focal spot so the laser pulse can be irradiated on the exactly opposite side on the front surface. In the step 3, 400 $\mu\ell$ water is mixed with the Rhodamine 6G

powder to prevent the clotting when it mixed with the PR directlyd, so that the surface of the micro-dot can be fabricated uniformly. By a photolithography technique, 120 nm thickness of micro structured dot array is placed on the Ag target patterned in 10×10, 15×15, 20×20 μm^2 squares with each dot 100 μm apart. By irradiating 532 nm laser pulse on the dots with appropriate intensity, the omnipresent contamination layer can be ablated whereas the proton rich dots remains [6].

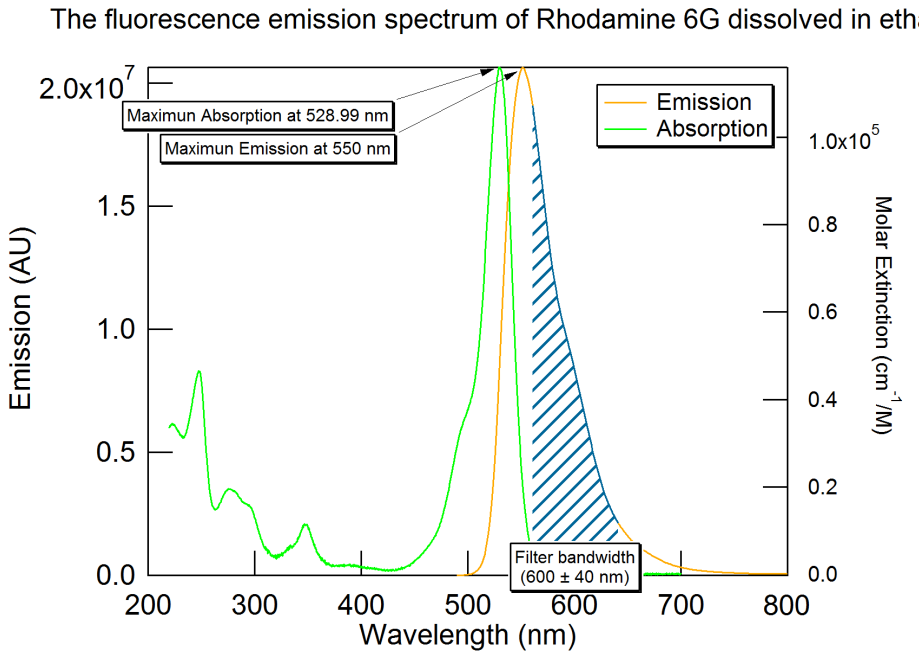

Figure 6.7: Absorption and emission spectrum of the Rhodamine 6G

Figure 6.8 shows the 10×10 μm^2 dots microscope image. The bottom image shows the light when they are exposed to the 532 nm light.

The intensity of the ablation light is pretty strong to see clear image of the scintillating dots on the CCD camera, so 750 nm filter can be installed with the camera. Figure 6.9 shows the dots image with the filter. The bottom image shows the micro-dot target on the holder.

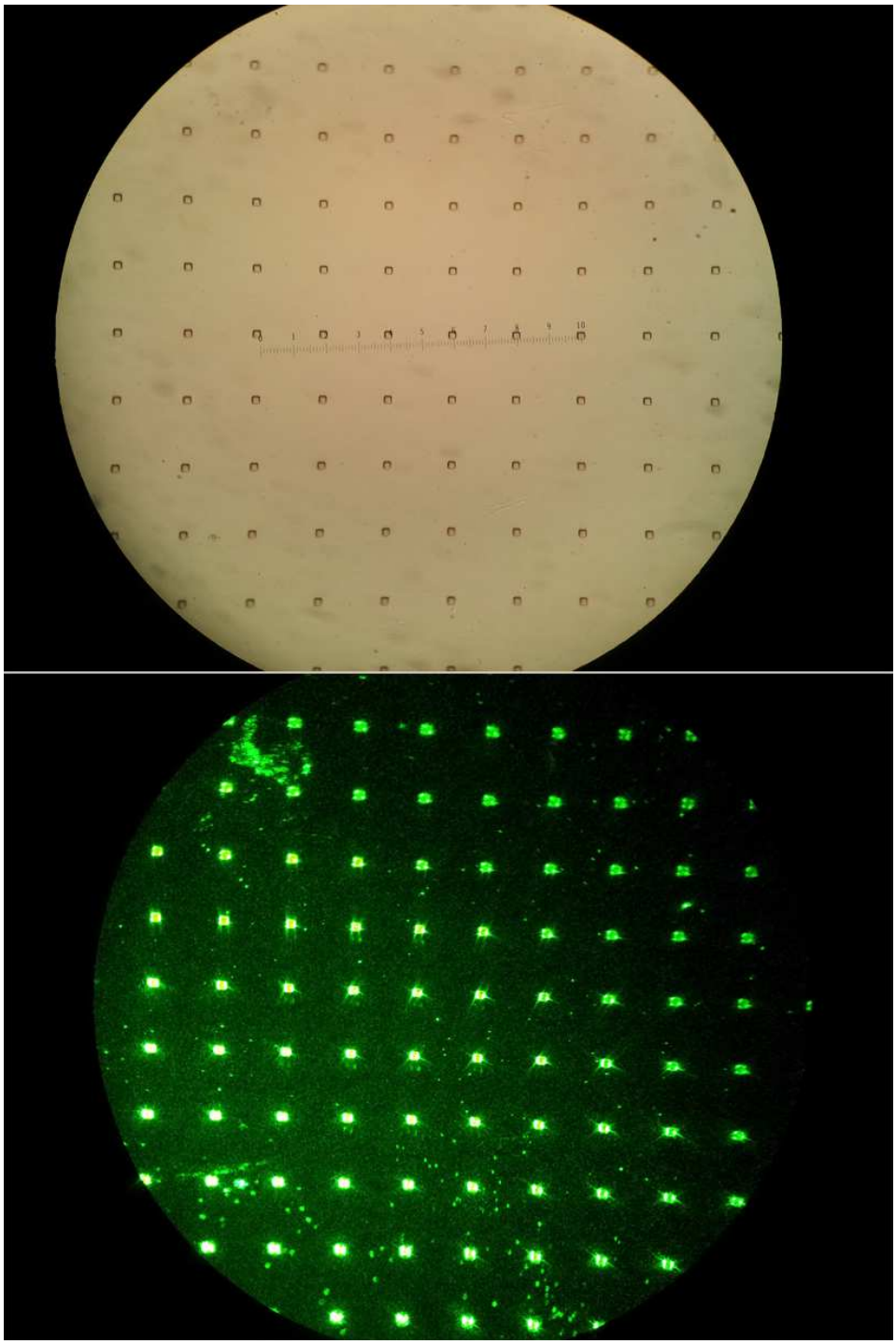

Figure 6.8: Micro-dot array target on a silver film coated on a substrate

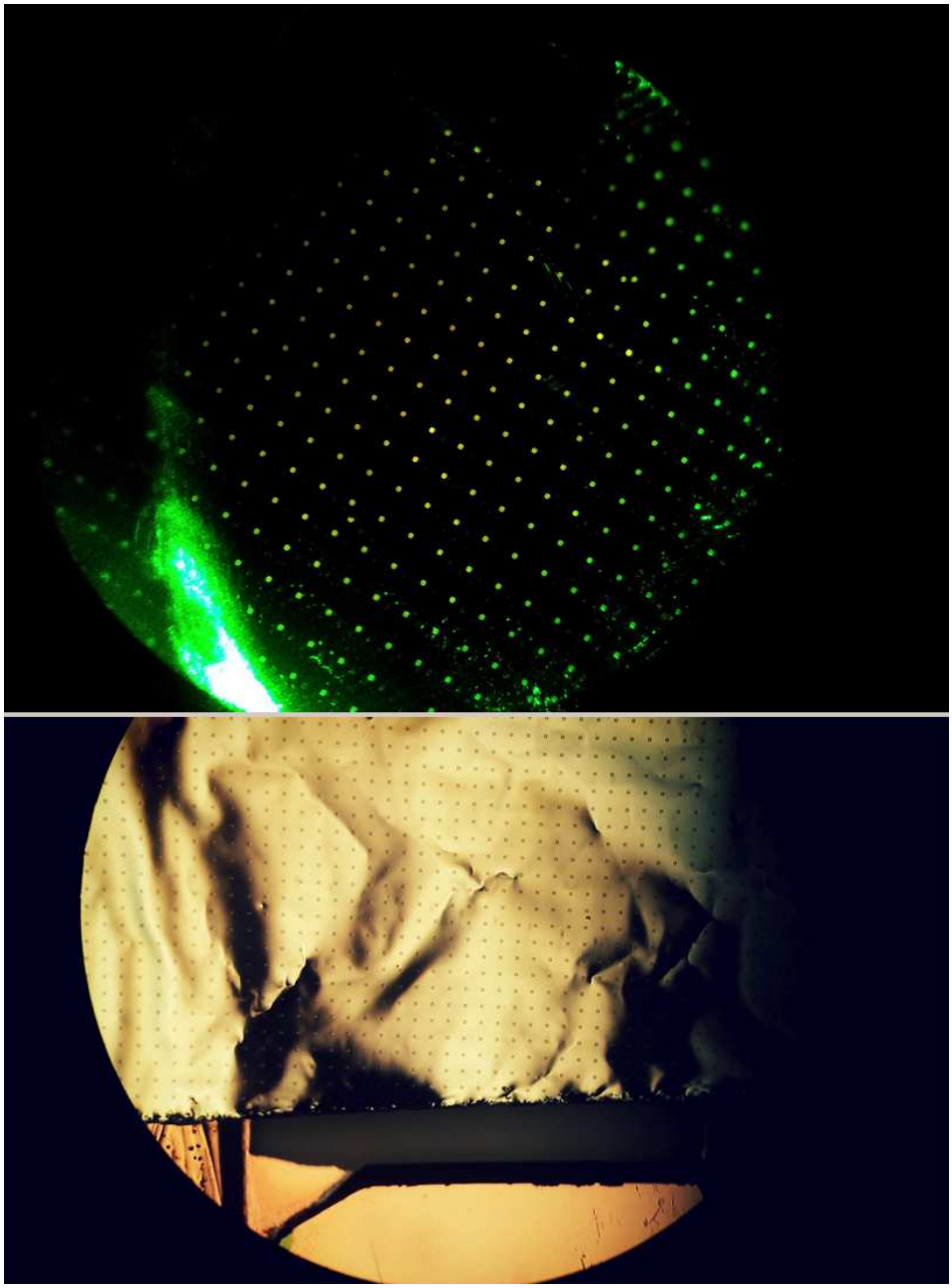

Figure 6.9: Micro-dot array target on the target holder

6.2.3 Experimental Setup

The experiment had been carried out at the Texas Petawatt Laser Facility. The λ_L=1057 nm , E=100 J at $\tau_L = 110$ fs laser beam is focused by $f/3$ OAP mirror to 8 μm diameter and the irradiance on the focal spot is order of 10^{21} W/cm^2. The laser is focused at the center of the 60 inch diameter target chamber (TC1). To relay the focal spot image to the outside of the target chamber (along through focus beam line), 2 optical relay system is utilized on the setup. Figure 6.10 shows the setup of the image relay system. At first, 20x objective is installed to magnify the focal spot image on its 18 cm back. This cast focal spot image is relayed by the combination of 2 achromats lens which can relay the image as a pin to pin telescope. By using achromats, the magnified image can be relayed long distance in minimal aberration.

The ablation beam is set at the outside of the chamber. Figure 6.11 shows the setup of the 532 nm, 10 Hz laser beam with an output power that can be controlled by tuning the control knob. The beam is expanded to prevent any damage to the quartz window and aligned into the chamber. This ablation beam is aligned to coincid with the focal spot in spatial.

Figure 6.12 shows that a STM tip is utilized to check that the 2 beams are coincident on the tip end.

Figure 6.13 shows the alignment prodecure of the micro-dot target. .

1. Find the focal spot image of the OPA beam and mark its position on the screen.

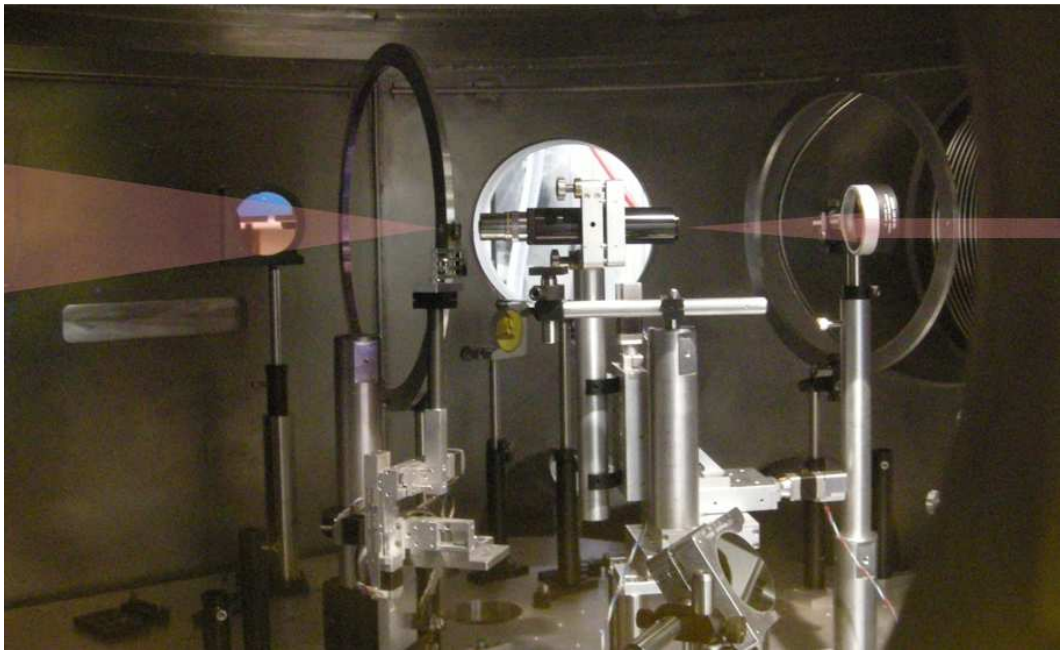

Figure 6.10: Image relay of the focal spot.

2. Place the STM tip with unpinched CW beam around of the focal spot plane.

3. Pinch down the CW beam to put the tip end on the focal spot. The tip end should be placed on the focal spot mark position.

4. Block the CW beam and turn on the low power ablation CW beam. Move the objective in forward and backward to get the sharp tip image due to the changed wavelength of the beam.

5. Move the target holder so the micro-dots image is on the screen.

6. Move the target in $\pm z$ direction to acquire best dot image is coincide

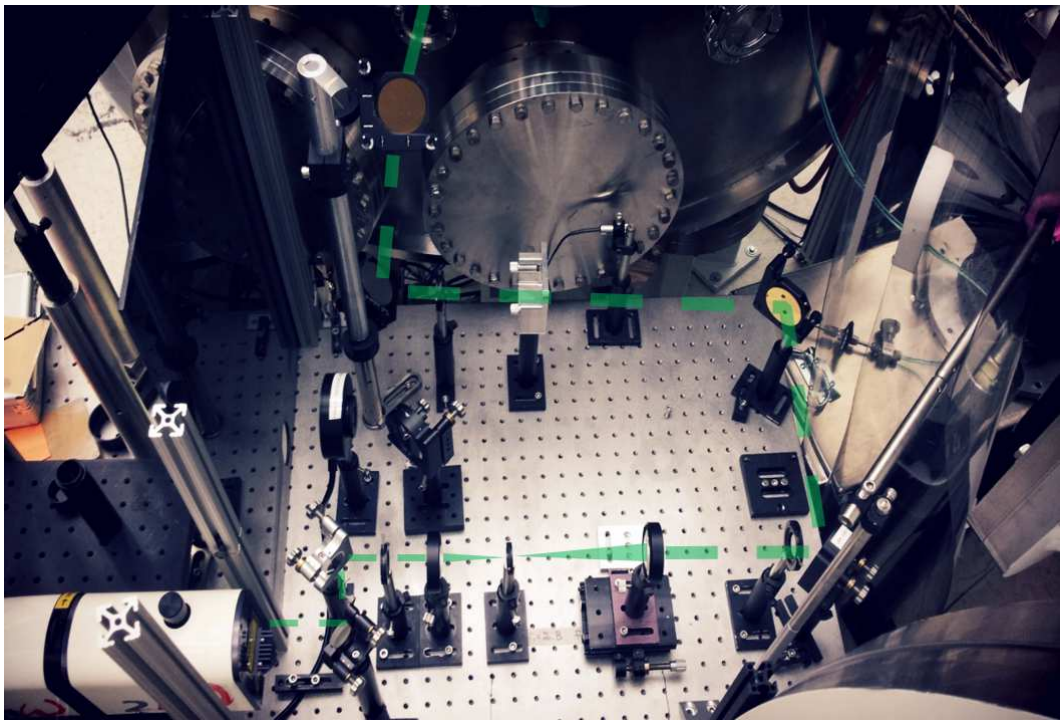

Figure 6.11: Ablation beam setup

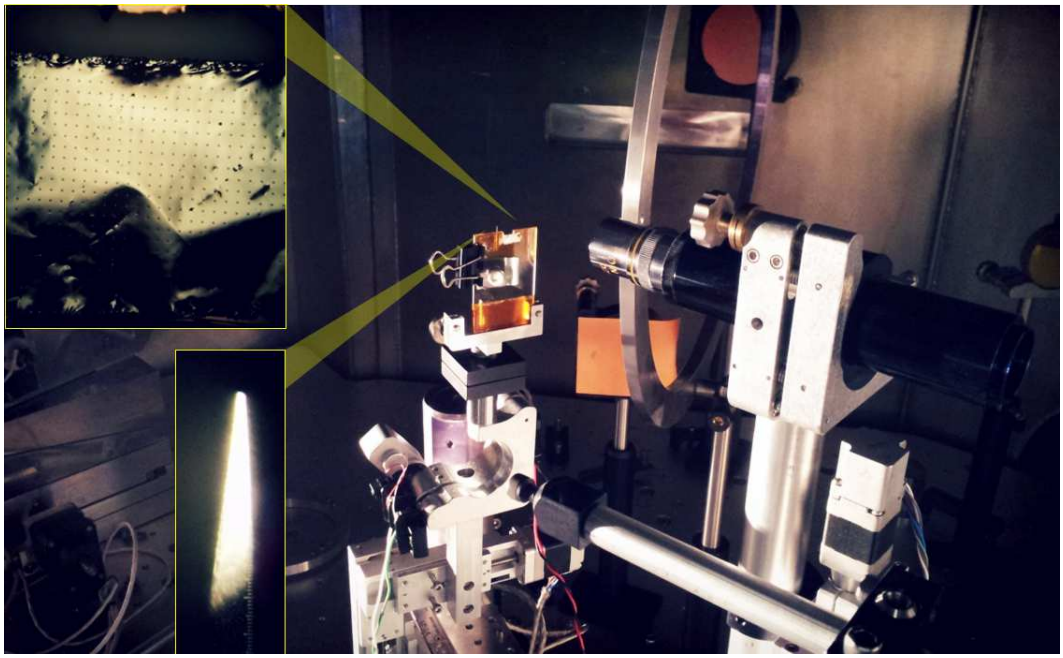

Figure 6.12: Micro-dot target on the focal spot.

with the marker.

7. Turn the ablation beam in 10 Hz mode and tune up to appropriate power so the ablation is getting started. Putting filter can help to see clear image of the dot.

6.2.4 Results

Accelerated protons and ions are detected by phosphor screen image plate in a Thomson parabola spectrometer. The charged particle beams are dispersed in the parabola on the ion's q/m ratios while they travel through 0.5 T of magnetic field and 0.7 MV/m of electric field. The proton energy spectrums for the micro-structured targets and bare targets are shown in the figure 6.14. The distribution can be fit to Maxwell-Boltzmann thermal distribution of the $N(H+) \sim \exp(-e\phi/k_B T_i)$ where the T_i is the ion temperature, ϕ is the quasi-static electric potential, e is the electron charge and k_B is the Boltzmann constant. Thus the slopes of each plot in the figure 6.14 are correspond to the each of ϕ, T_i. In the experiment, the laser is operated keeping steady irradiance on the focal spot so the temperature of the hot electrons is likely to be constant for all system shot. This leads that the ϕ related with the hot electrons temperature has been kept consistently for all system shot. Consequently, the slope in the figure 6.14 is strongly related with the ion temperature T_i. The shot # 5413, 5417 for bare targets shows gentle slope than the micro-dot case which means the ion plasma temperature of the bare target experiments is more hotter than micro-dot case. The thickness of polymer micro-dot is 100

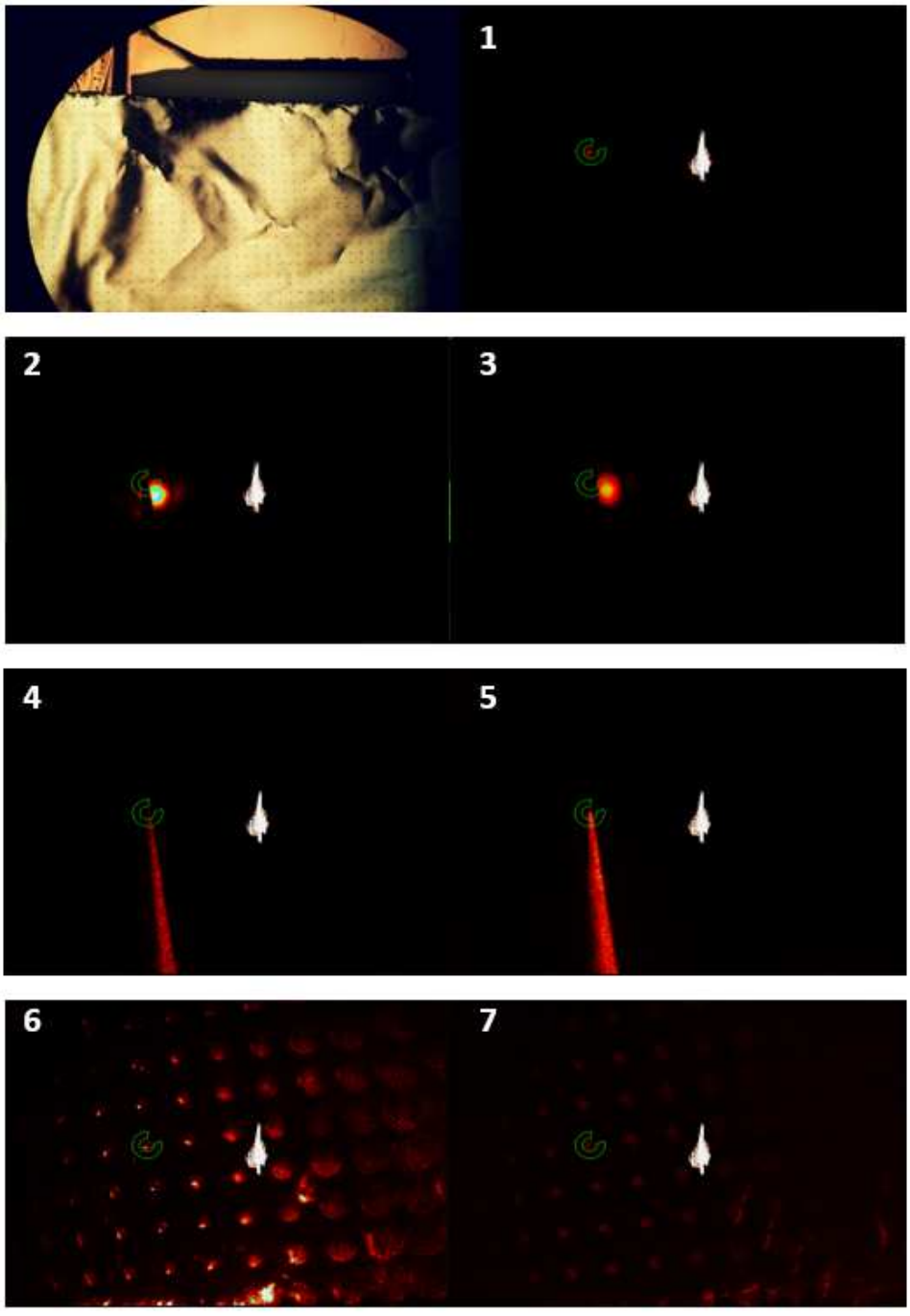

Figure 6.13: Micro-dot target alignment procedure

nm at best that is ignorable with the 800 nm of Ag foil target and the microns scale length of the Debye length. Therefore, the micro-dot itself diminish the ions temperature which aroused from the interaction with the hot electrons cloud. The presumptions for the diminished ions temperature is the presence of the micro-dot itself. The density of the micro-dot is much dense than the air contiminating layer, almost 10^3 times denser. This density difference leads shorten Debye length on the target by a factor of 0.03 which means the Debye length on the target rear surface is order of tens nanometer for the micro-dot target. If the micro-dot is thicker than this length, then the hot electrons can not be separated from the micro-dot fully and this results weaken quasi-static sheath field. Moreover, the abundant carbon and oxygen atoms in the micro-dot hamper effective acceleration of the lighter ions like hydrogen. When the strong quasi-static field ionizes the atoms in the sheath field, the carbon and oxygen atoms screen the hydrogen atoms in the sheath field and this hampers effective separation of the lighter ions from the other species of ions.

On the other hand, we can compare the presence and absence of the ablation beam (532 nm) for each targets. Comparing the presence (shot# 5417) and absence (shot# 5413) of the ablation beam for the bare target, we observe that the number of protons are reduced when the contaminating hydrogen layer on the target rear surface is cleaned by the 532 nm ablation beam so that the source of proton beam is dwindled. This result make sense with the TNSA mechanism which explains that the proton is originated from the target rear surface. However, the micro-dot targets shows somewhat different

trends with the bare targets. Comparing the presence (shot# 5423, 5425) and absence (shot# 5431) cases of the ablation beam for the micro-dot targets, the number of proton is increased when the target rear surface is cleaned with the ablation laser beam.

Meanwhile, the pointing error for the system shot is analyzed through the Far-Field diagnostic system. The spatial alignment of the micro-dot is very important in this experiment, so we acquire the pointing error data to check the reliablity of the experimental data. The micro-dot is aligned with the attenuated OPA beam so that the center of the dot is coincide with the focal spot. The Far-Field diagnostic system installed on the diagnostic table at the TPW captures the OPA beam image and system shot image. By comparing the center of the these 2 images, we can track the pointing error of the system shot. Figure 6.15 shows the pointing error analysis for the experiments. Taking consider the focal spot size on the target front surface, one can insisit that the micro-dot is spatially coincident with the focal spot for the system shots.

From the micro-dot experiment, we clearly see evidence of proton acceleration from the micro-dot as the proton yield from a cleaned target is much reduced unless we are spatially aligned to the micro-dot. And as shown in the figure 6.14, we do see differences in the proton energy spectrum from micro-dots when compared to simple bare target (uncleaned and hence coated with uniform proton containing layer). However, to date we have seen no evidence of a monoenergetic beam.

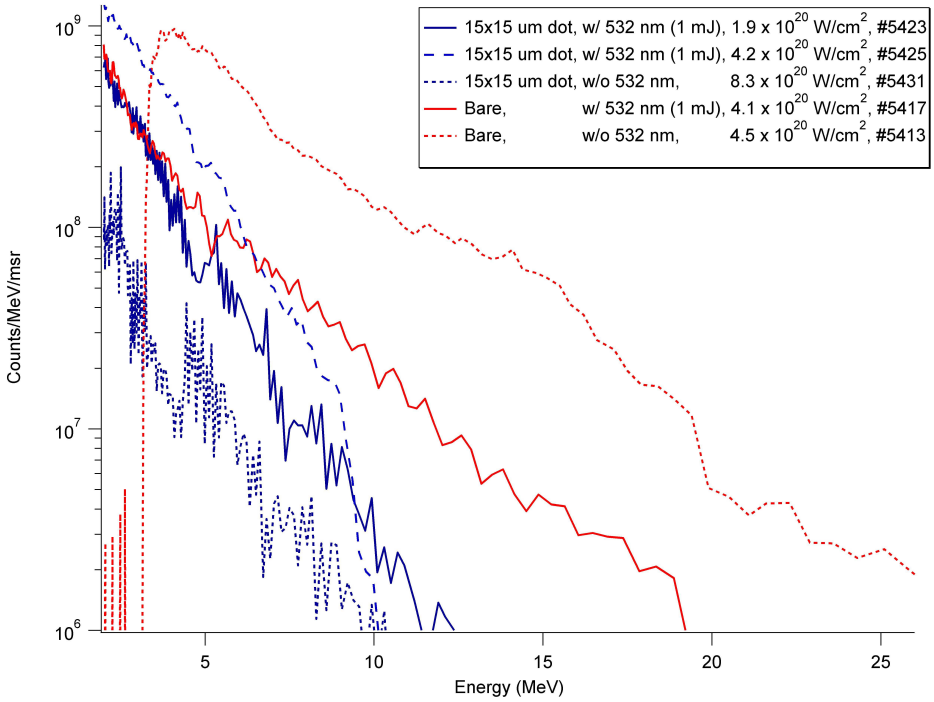

Figure 6.14: Proton energy spectrum of the micro-dot expriment.

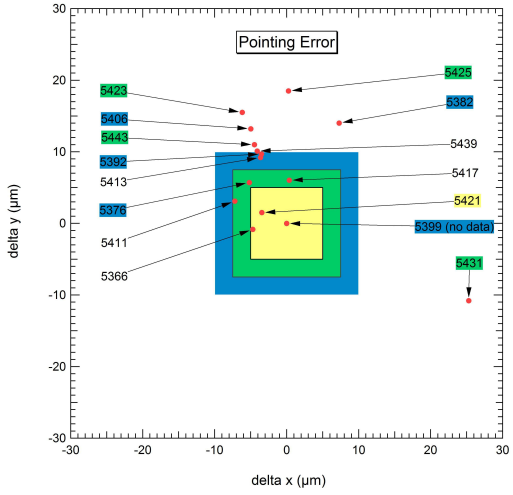

Figure 6.15: Pointing error analysis with the Far-Field diagnostic image.

6.3 Circularly Polarized Laser Experiments at the GHOST

6.3.1 Motivation

When a linearly polarized TW laser pulse interacts with a solid target, the hot electrons generated by the J $\times$ B heating lead to charge separation and accelerate ions to multi-MeV. However, this non adiabatic heating of hot electrons result in a thermal distribution of the accelerated ions. To suppress the thermal effects of the hot electrons, circularly polarized beam incident on an ultra-thin target has been suggested, so that the oscillating component of the J $\times$ B force is suppressed [50][51][64].

Recently, experimental studies for the circularly polarized laser driven ions acceleration have been conducted from several research group [28][45]. In these references, a few notable properties of the circularly polarized laser driven ions acceleration has been reported at the irradiance level of $I < 10^{16}$ W/cm^2 and $I \sim 10^{19}$ W/cm^2. In the reference [28], a quasi-monoenergetic peak for the carbon ions had been observed around 30 MeV. In the reference [45], a quasi-monoenergetic proton peak had been observed around 1.1 Mev for a hydrogen gas jet target.

In this experiment, we study proton acceleration experiment with circularly polarized laser beam comparing with linearly polarized beam and clarify the experimental distinction between of them.

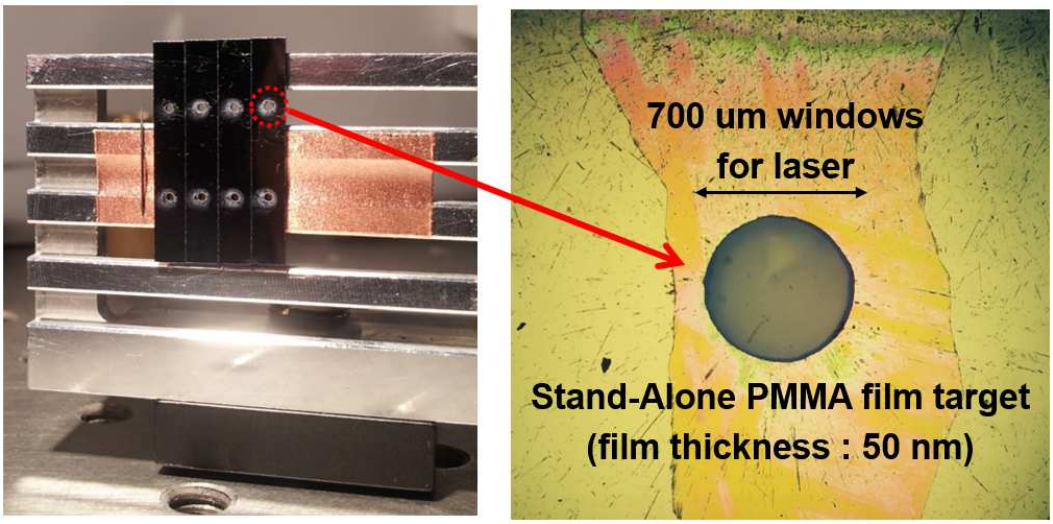

Figure 6.16: 50 *nm* PMMA film on the substrate.

6.3.2 PMMA Target Fabrication

The concept of the fabrication for Stand-Alone ultra thin target is very similar with the micro-dot target. Spin coated PMMA on the PVA baked substrate is the film substrate. And then the PMMA film can float when the substrate is soak in water. The thickness of the PMMA film can be controlled by the chlorobenzene concentration in the solution and the thickness should be characterized with an ellipsometry.

1. PVA spin coating
   (a) 3000 rpm, 60 sec
   (b) Hard baking (110 °C, 5 min)
2. PMMA spin coating

(a) 3000 rpm, 60 sec

(b) Hard baking (110 °C, 5 min)

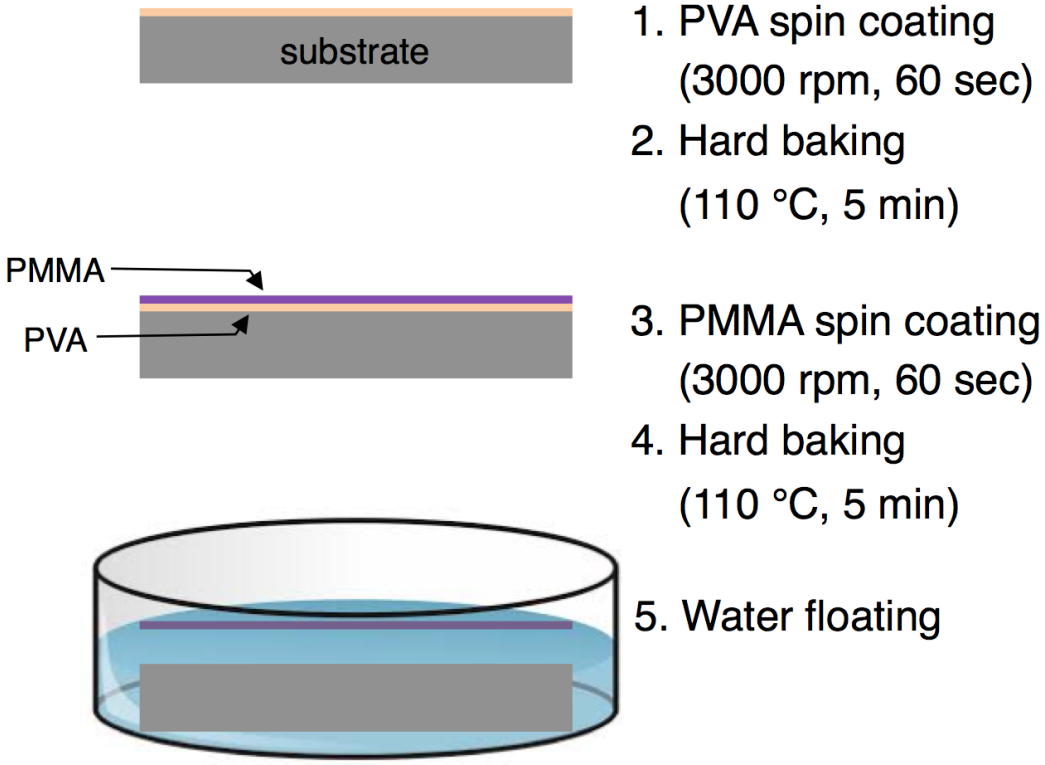

Figure 6.17: A scheme for the PMMA target fabrication.

As shown in the figure 6.16, 700 μm through holed silicon substrate is used to hold the film and 4 set of these substrate is mounted on the target holder.

6.3.3 Experimental Setup

The GHOST compressor is compatible with vertically polarized beam, thus linearly polarized compressed laser is incident into the target chamber. To convert linearly polarized laser into circularly polarized laser beam, $\lambda/4$ waveplate are widely used when the non-linear effects are ignorable. However , the B-integral is not ignorable when the 1.6 J at 115 fs pusled laser beam pass through the 0.6 mm thickness of the crystal quartz waveplate whose n_2 is order of 10^{-16} cm^2/W.

$$B = \frac{2\pi}{\lambda} \int n_2 I(z) dz \approx 0.9 \tag{6.1}$$

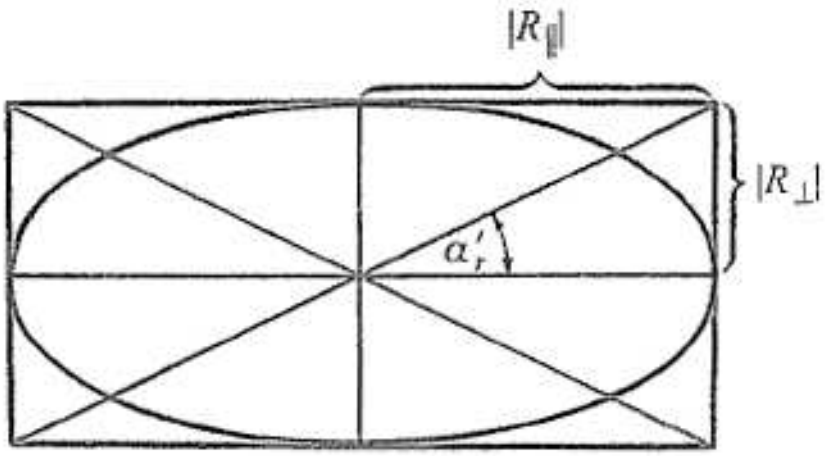

Figure 6.18: Vibration ellipse of light reflected from a metal at the principal angle of incidence.

Therefore, we need to design the other way of generation of the circularly polarized laser beam. In stead of introducing $\lambda/4$ waveplate, a periscope

is designed which rotates the laser polarization direction 45 degree such that 50 % of P-pol. and 50 % of S-pol can be incident to a metal mirror. If this laser beam incident in the principal angle on a metal mirror, then it reflected as elliptically polarized light. If, moreover, $P \tan \alpha_i = 1$, then the reflected light is circularly polarized where $P = \rho_\perp / \rho_\parallel$, $\rho_\perp, \rho_\parallel$ are absolute values of the reflection coefficient in normal and parallel, α_i is the azimuth angle of the linearly polarized incident beam [40]. As shown in the figure 6.18, the circularly polarized reflected beam can be occurred when the $\alpha_r^{'} = 45^\circ$ and this means that the azimuth angle of the incident beam must be $\alpha_i = 45^\circ$ [40].

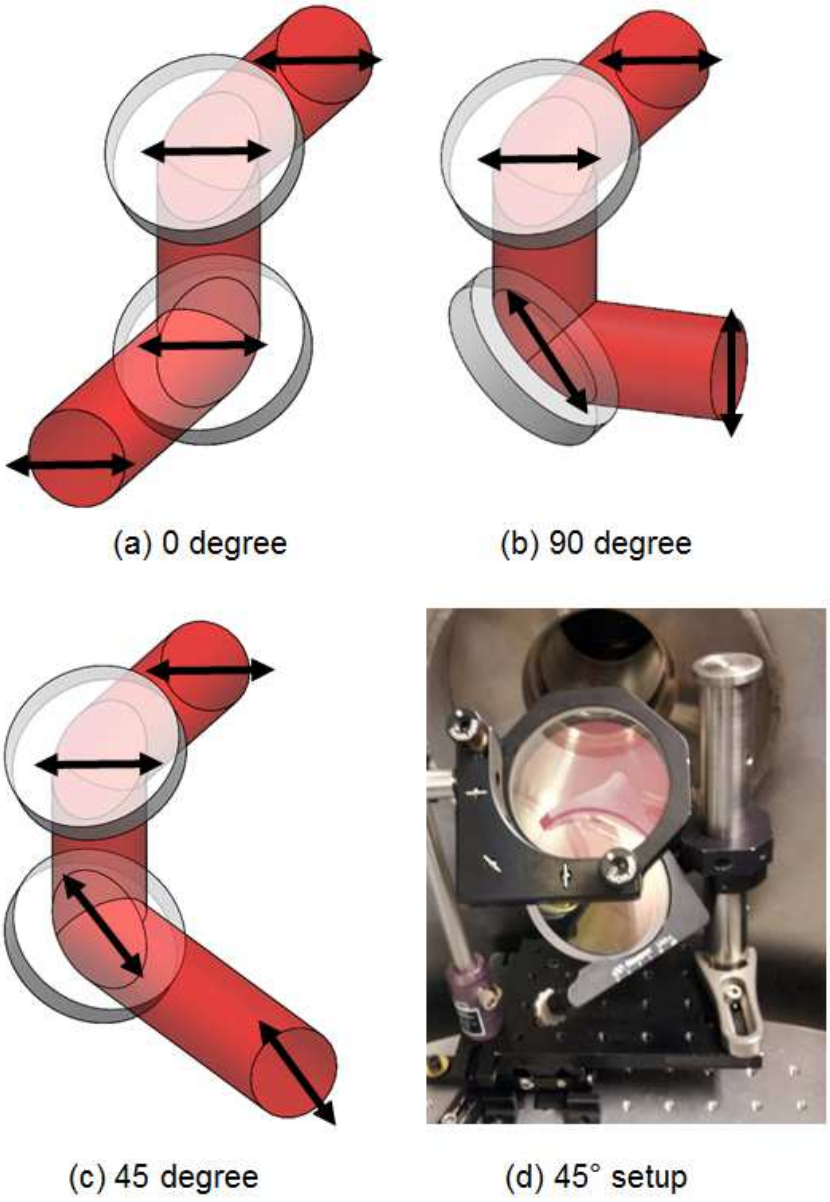

Figure 6.19: (a) A periscope scheme for 0° rotation in azimuthal angle of the polarization. (b) 90° rotation scheme. (c) 45° rotation scheme. (d) 45° rotation setup.

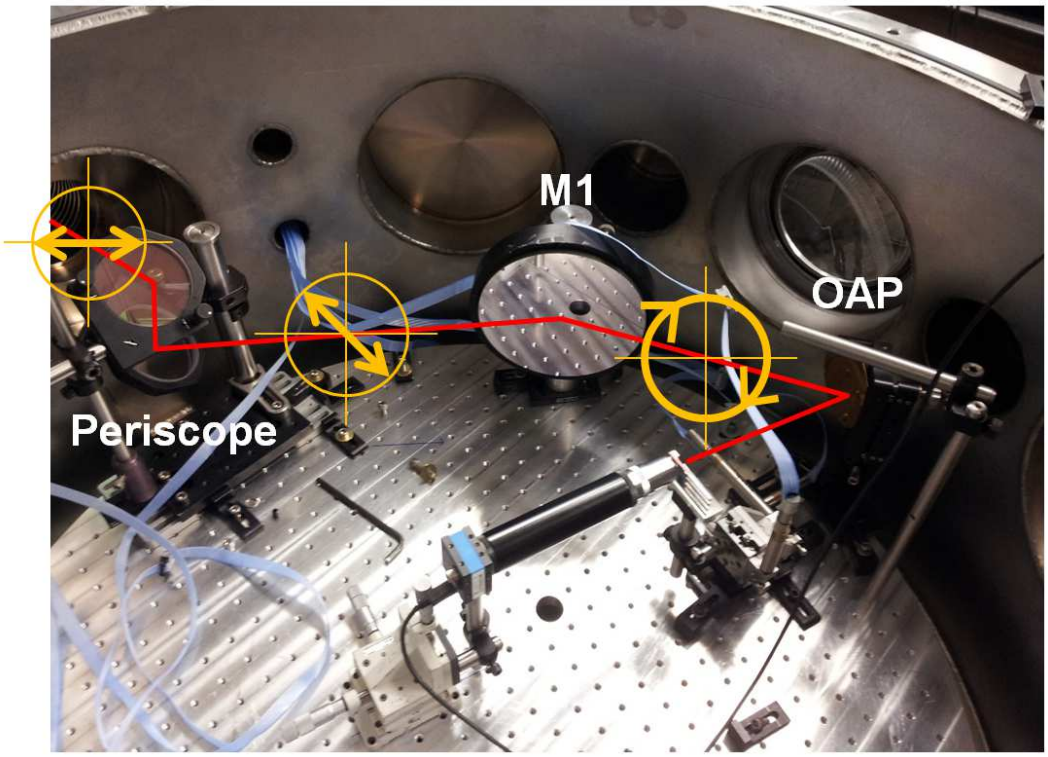

Figure 6.20: Scheme of the periscope and M1 setup for circularly polarized beam generation.

Figure 6.19 shows the periscope that is composed of 2 mirrors such that the azimuth angle of the polarization of the reflected beam can be 45°. The angle of 2nd mirror controls the azimuth rotational angle of the laser polarization. This 45° setup satisfies $\alpha_i = 45°$ and that leads to $\alpha_r^{'} = 45°$ which is the condition for the circular polarization of the reflected beam. Figure 6.20 shows that how the polarization is changed from periscope to focal spot. A 6" aluminum coated mirror (M1) is installed after the periscope to accept the

beam which is incident in a large angle of incident.

To check whether the azimuth angle is rotated as desired, a linear polarizer mounted CCD camera measures the beam intensity. The beam intensity is measured in every 10° rotated polarizer and plot the intensity as a function of the polarizer rotating angle. Figure 6.21 shows the beam intensity polar chart at 1. before periscope (yellow), 2. after periscope (blue), 3. after M1 (green) and 4. at the focal spot (red). This chart clearly shows the azimuth angle of the polarization. Before the periscope, the beam is horizontally polarized. But the azimuth angle is rotated in 45° after the beam pass the periscope. This beam is incident to the M1 in the principal angle of incidence. As shown in the figure 6.21, the beam intensity after M1 is very close to the circularly polarization with its ellipticity $e = 0.86$. And this ellipticity is valid on the focal spot either.

On the other hand, the question for the ellipticity if it effects for the condition of RPA had been presented and S. G. Rykovanov et. al. studied the effect of ellipticity numerically [51]. As shown in the figure 6.22, RPA dominant regime for quasi-monoenergetic proton beam had been studied with changing ellipticity [51]. According to the study, there is a threshold ellipticity, e_{thr} is 0.7. When the ellipticity is less than the threshold, the quasi-monoenergetic proton peak is not observed anymore which means the RPA is not dominant. And this threshold is independent from the laser intensity although it changes a little when the a_0 is less than 7. In this experiment, we achieve $e = 0.86$ which means that the oscillating effect from linearly polarization can be suppressed

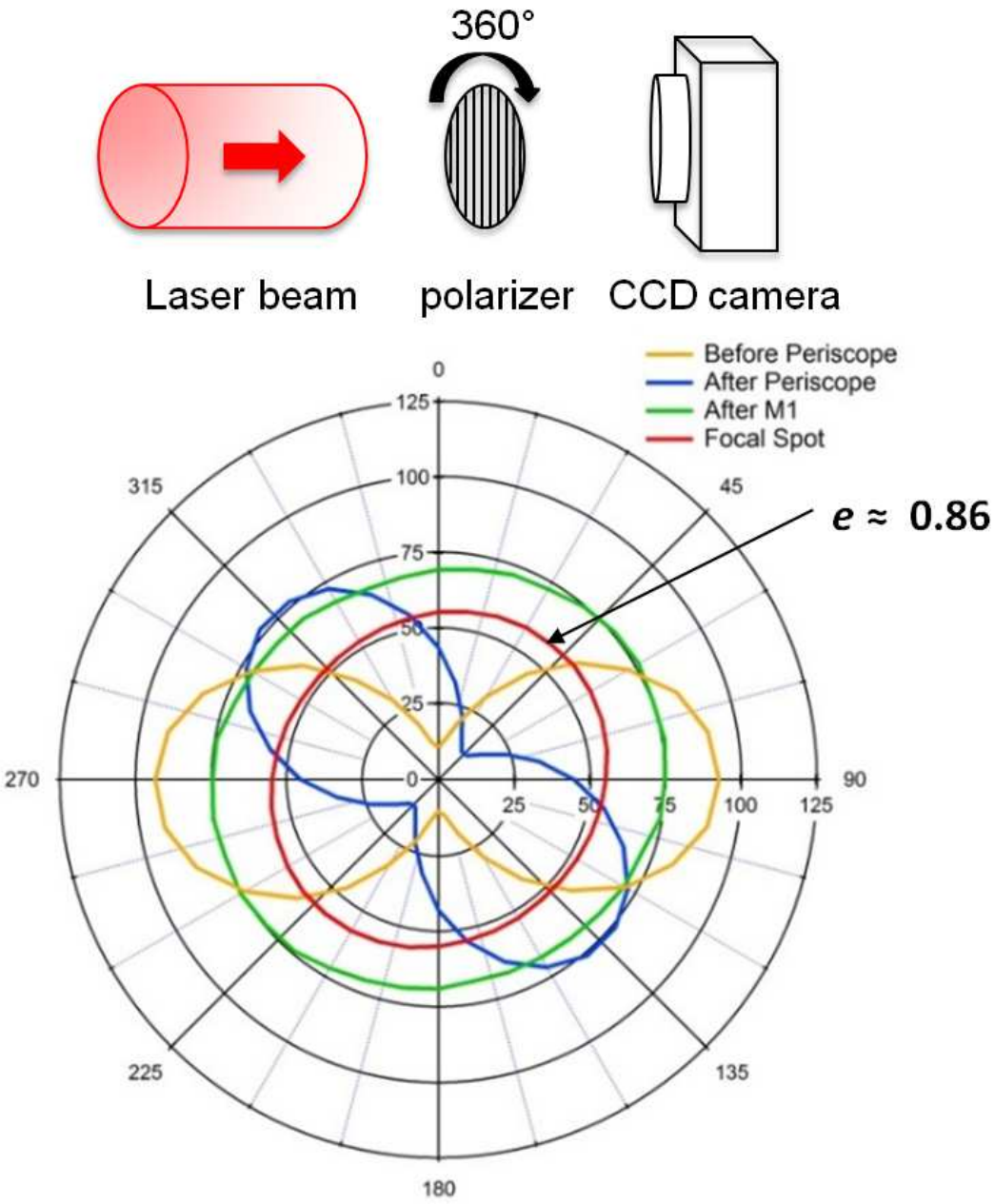

Figure 6.21: Beam intensity measurement for rotating the polarizer 360°.

efficiently.

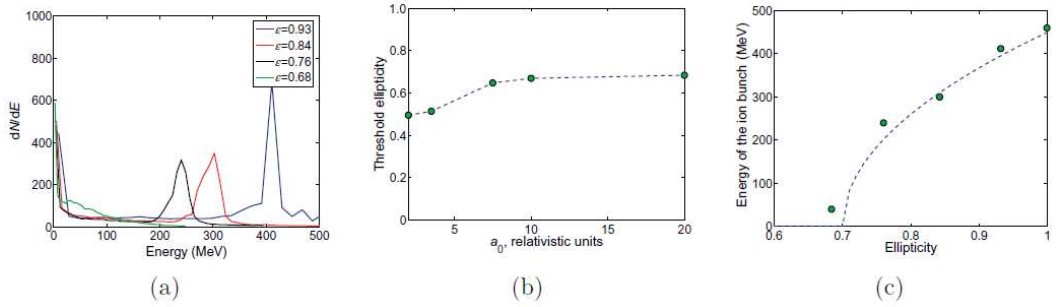

(a) (b) (c)

Figure 6.22: (a) Proton energy spectrum for $a_0 = 20$ and different ellipticities. (b) Dependence of thershold ellipticity on a_0. (c) Dependence of the proton bunch energy on ellipticity for $a_0 = 20$ [51].

Figure 6.23 shows the through focus image relay setup. 20X infinity-corrected objectives relays the focal spot image followed by achromat lens at the chamber outside along the collimated beam line. Figure 6.24 shows the focal spot image focused by $f/3$ OAP and relayed to the CCD camera. The beam is focused upto 7 μm in FWHM which can generate the intensity of 3×10^{19} W/cm^2. The objectives is retracted to the back of shielding block for system shot so the ions and electrons can be injected into the Thomson parabola spectrometer or electron spectrometer through the pinhole. The PMMA target is set to be normal to the main laser beam by check the reflected back to the up stream. To align the PMMA target on the focal spot, the STM tip is installed with the target on the target holder. When the tip end is placed so coincided with the focal spot, we can tweak the image realy system to acquire the best image of the tip end on the camera. Figure 6.25 shows

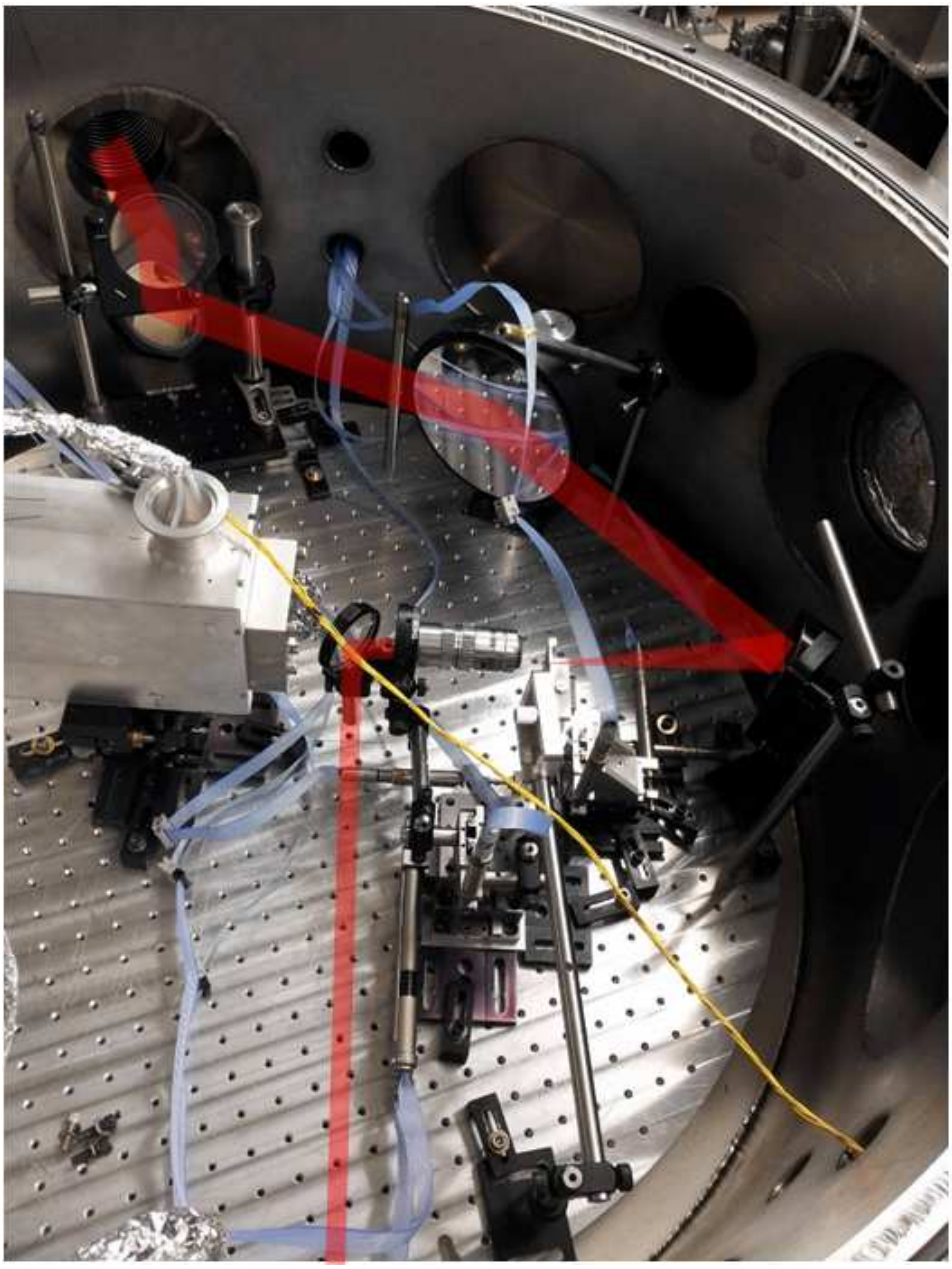

Figure 6.23: Through focus beam setup with 20X infinity-corrected Objectives.

the STM tip image relayed through the 20X objectives. With this best image relay system, the PMMA target can be align on the focal spot. When the PMMA film is placed on the focal spot, any dust attached or defects on the target film is shown on the camera. By finding the best image of the dust or defects, the PMMA target can be placed on the focal spot of the Gaussian beam.

Thomson spectrometer is aligned to be parallel with the main beam by using HeNe laser on it. When the Thomson parabola spectrometer is aligned parallel with the main mean, then the airy pattern through the pinhole must be observed on the main laser up stream. In this way, the target can be aligned normal to the main beam and Thomson parabola spectrometer.

The M1 is dislodged to switch from circularly polarized to linearly polarized setup. The energy reflectivity of the Al mirror is almost 80% so the laser energy of the linearly polarized is tuned down by manipulate PFN charge knob to deliver the same amount of the energy on the target. Figure 6.26 shows the setup of the linearly polarized beam with the Thomson parabola spectrometer. To measure the electron temperature, the Thomson parabola spectrometer is replaced with the electron spectrometer but the distances from target to spectrometer are always same for any setup to keep the consistency.

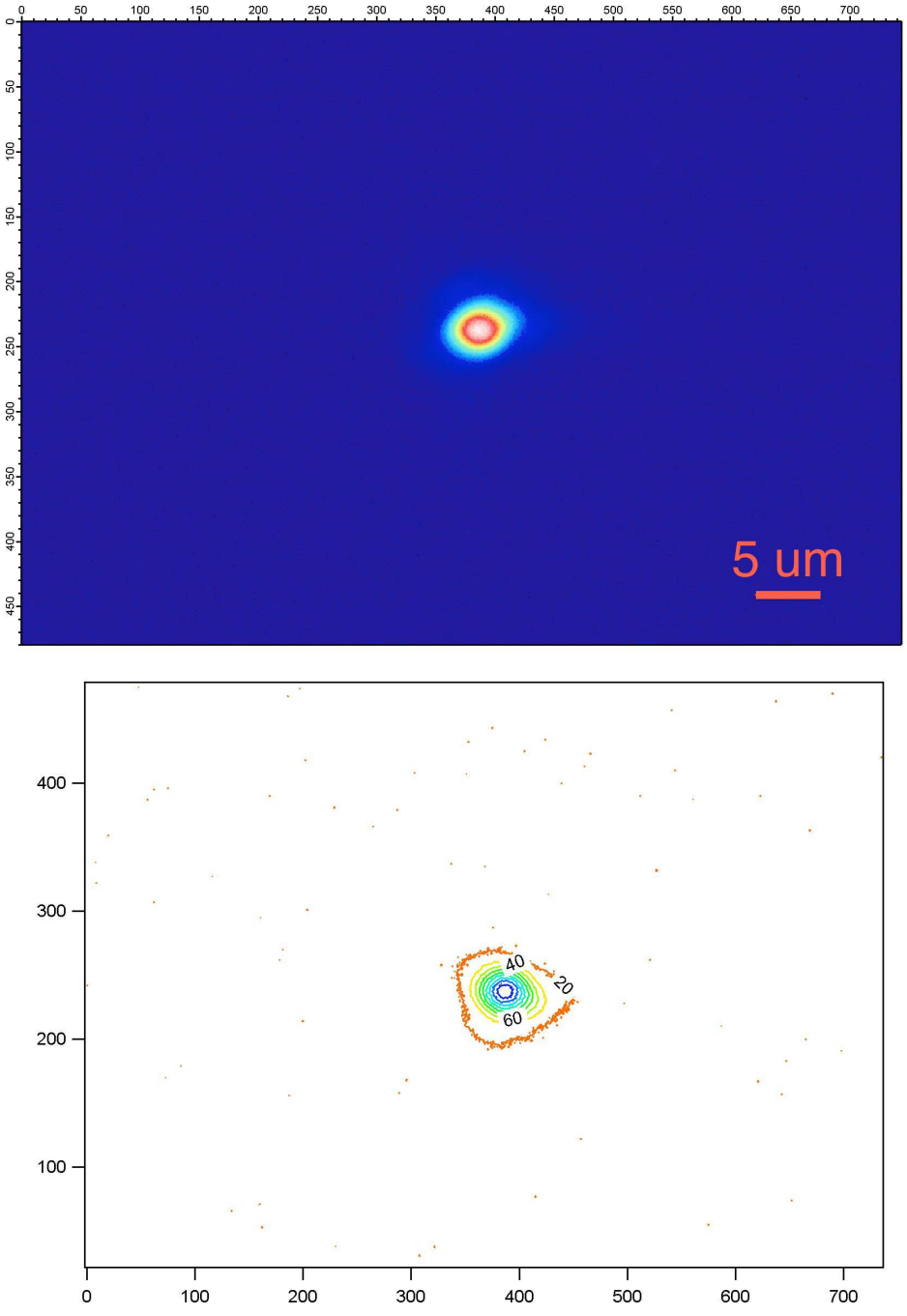

Figure 6.24: Focal spot image and its contour line.

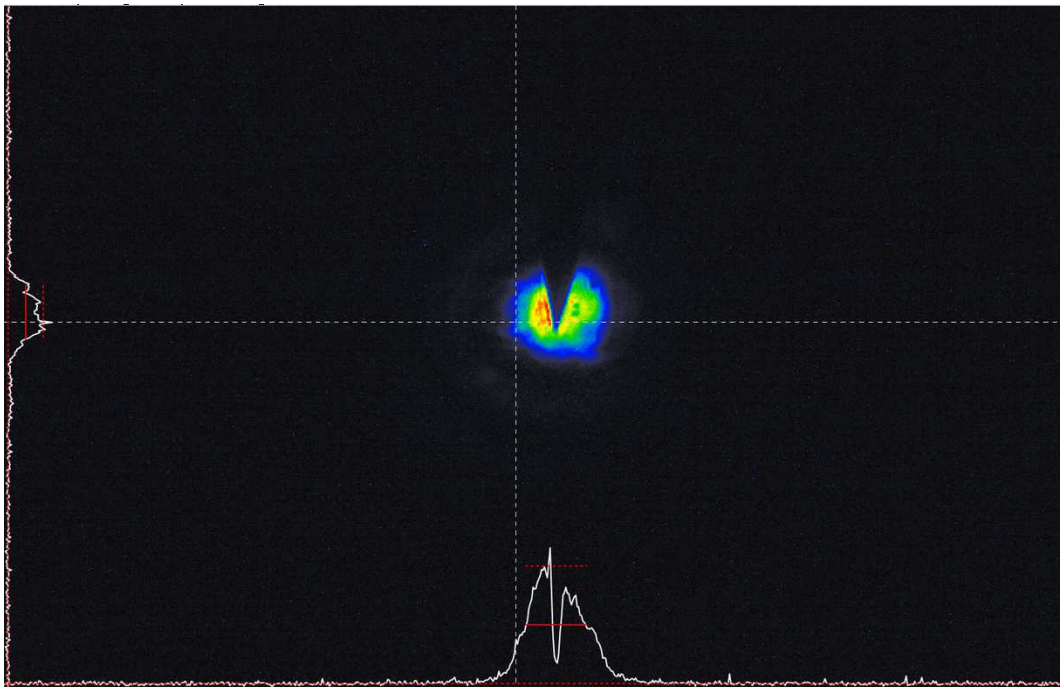

Figure 6.25: STM tip end image alogn the through focus line.

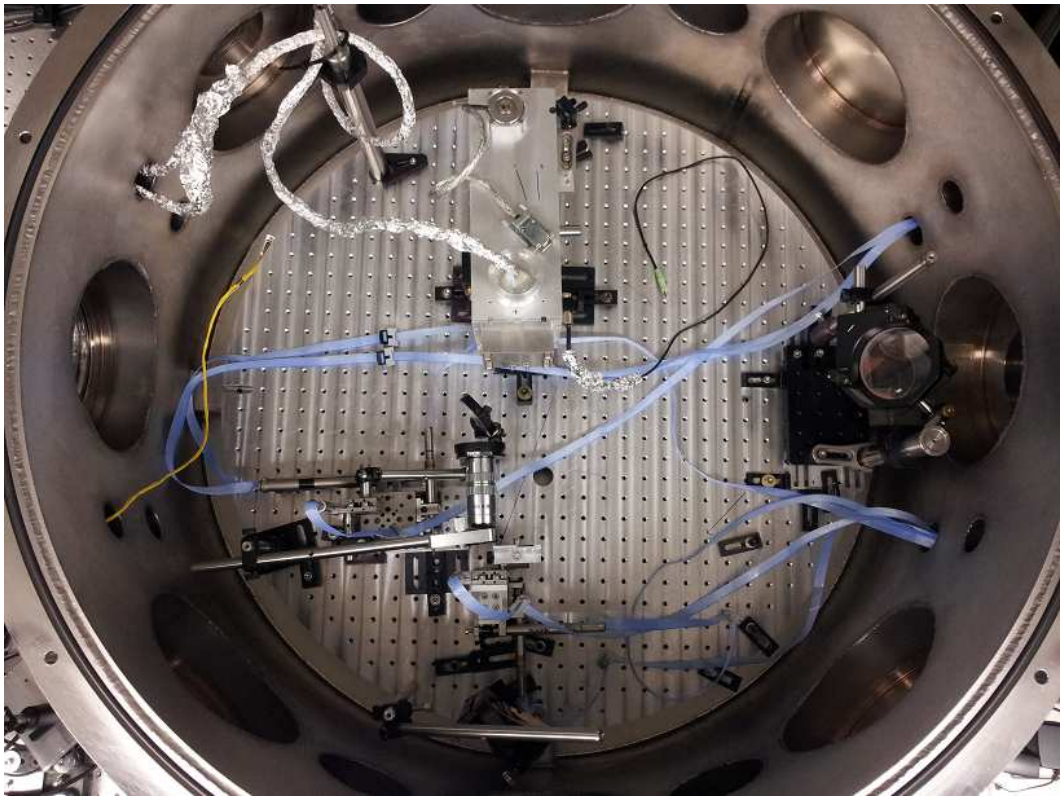

Figure 6.26: Experimental setup with the Thomson parabola spectrometer.

6.3.4 Results

To compare the hot electrons temperature generated by the circularly polarized and linearly polarized laser beam, the electron spectrometer introduced at chapter 5 is installed and collect the energy spectrum data. Figure 6.27 and figure 6.28 shows the raw data of the Phosphor image plate for the circularly polarized and linearly polarized beam respectively. As shown in the figure 6.28, more hot electrons from the linearly polarized beam than circu-

larly polarized beam are observed abundantly. To compare quantitatively for both case, the raw data are converted to a plot of the number of hot electrons as a function of kinetic energy by using the image plate calibration reference [11]. The number of particle spectrum for all thickness target is shown from figure 6.29 to figure 6.34. The red curve is for linearly polarized and the blue curve is for circularly polarized beam and the dark and light color is for the different shot. For all thickness targets, the linearly polarized beam generates two peaks. The first peak occurs around of 300 keV and the second peak occurs from 0.8 MeV to 1.5 MeV. On the other hand, the circularly polarized beam generate only one peak around of 300 keV. The temperautre of hot electron produced from J $\times$ B heating can be calculated from the equation 3.22, and it is almost 1.3 MeV for the linearly polarized GHOST laser. Thus the second peak of the linearly polarized cases are correspond to the hot electrons generated from J $\times$ B heating. The width of the second peaks are getting broaden as the target thickness is getting thicker. This means that the TNSA assiciated with the the J $\times$ B heating is dominant for the thicker target. For the circularly polarized beam, we can observe that the J $\times$ B heating is dramatically suppressed so that there is no peak on the corresponding temperature. In the case of circularly polarized beam, only lower energy hot electrons are observed that peak also occurs in the linearly polarized beam. The J $\times$ B heating is assumed to be suppressed and the oscillating effects of the ponderomotive force is also to be diminished for the circularly polarized beam. However, on the wing of the focal spot, the beam is not normal to the

target perfectly so there is longitudinal component of the laser electric field. This trivial longitudinal component can drives resonance absorption in both case of circularly and linearly polarized beam. The formula of the hot electron temperature generated by the resonance absorption is given from the equation 3.16. For the linearly polarized GHOST laser, the T_{hot} is almost 600 keV. The peak is occured around of 300 keV and this corresponds the temperature of the resonance absorption that is generated by 30% of the peak intensity. Thus the laser energy at few microns away from the center of focal spot is able to contribute in generation of hot electrons driven by resonance absorption though the laser is normal to the target. Accordingly these difference in hot electrons temperatures driven from linearly and circularly polarized laser beam result different proton energy spectrum.

The proton energy spectrum data collected by the Thomson parabola spectrometer are shown from figure 6.35 to figure 6.41. The red curves are for the linearly polarized and blue color curves are for the circularly polarized setup likewise electron spectrometer. In both of case, the proton energy distribution can be fit to Maxwell-Boltzmann thermal distribution. The slope of the linearly polarized case are gentle than the circularly polarized case that means the ions temperature of the linearly polarized case are obviously hotter than the circularly polarized case. Accordingly, the linearly polarized beam generated higher cut-off energy than circularly polarized beam. And we observe that the cut-off energy is quite independent from the target thickness. Comparing the proton energy spectrums with the electrons energy spectrums,

we observe that suppressed hot electron driven by J × B heating leads smooth acceleration of the protons. Quelling the isochronic heating process by suppressing the J × B heating, the electrons are heated pretty gently and pushed along the laser beam direction smoothly.

The difference of the cut-off energy for both polarization can be compared from the the sheath field strength. From equation 4.2, $E_{sheath} \approx \frac{k_B T_H}{e\,\lambda_D}$, the sheath field sheath field is proportional to the hot electron temperature. But the Debye length, $\lambda_D = \sqrt{(k_B T_H)/(4\pi n_e e^2)}$, is also proportional to the the square root of the hot electron temperature. Thus, the sheath field is proportional to the square root of the hot electron temperature, $E_{sheath} \propto \sqrt{T_H}$.

The electric field of the linearly polarized beam is stronger than the electric field of the circularly polarized beam by a factor of $\sqrt{2}$, $E_{LP} = \sqrt{2}E_{CP}$. And the beam intensity is proportional to the square of the electric field strenght, $I \propto E^2$. Thus the beam intensity of the linearly polarized beam is stronger than the circularly polarized beam by a factor of 2, $I_{LP} = 2I_{CP}$. If the J × B heating is not suppressed by the circularly polarized beam, then we can compare the hot electron temperature for both case by using the equation 3.22, $T_{J\times B} = 0.511\left(\sqrt{1 + (I\lambda_\mu^2)/(2.8\times 10^{18})} - 1\right)$ MeV. And it results that the hot electron temperature of the circularly polarized case is less than linearly polarized beam by a factor of 0.63, i. e. $T_{CP} = 0.63\,T_{LP}$. Thus the comparison of the sheath field for both case becomes that $E_{sheath,CP} = \sqrt{0.63}\,E_{sheath,LP} = 0.8\,E_{sheath,LP}$. Namely, the sheath field of the hot electron driven by linearly polarized is stronger by a factor of 0.8 than the sheath field

of the circularly polarized case when we assume the suppressing doesn't work.

On the other hand, the experimental cut-off energy of the proton for linearly polarized beam is almost higher by a factor of 2 than the circularly polarized beam as shown from figure 6.35 to figure 6.41. This means that the lower cut-off proton energy of the circularly polarized beam is not originated from the weaken electricfield by changing the the polarization simply. It is the effect of the suppressed J $\times$ B heating evidently.

Consequently, the suppression of the generation of the hot electron by J $\times$ B heating is observed from the circularly polarized beam incident on the ultra-thin target.

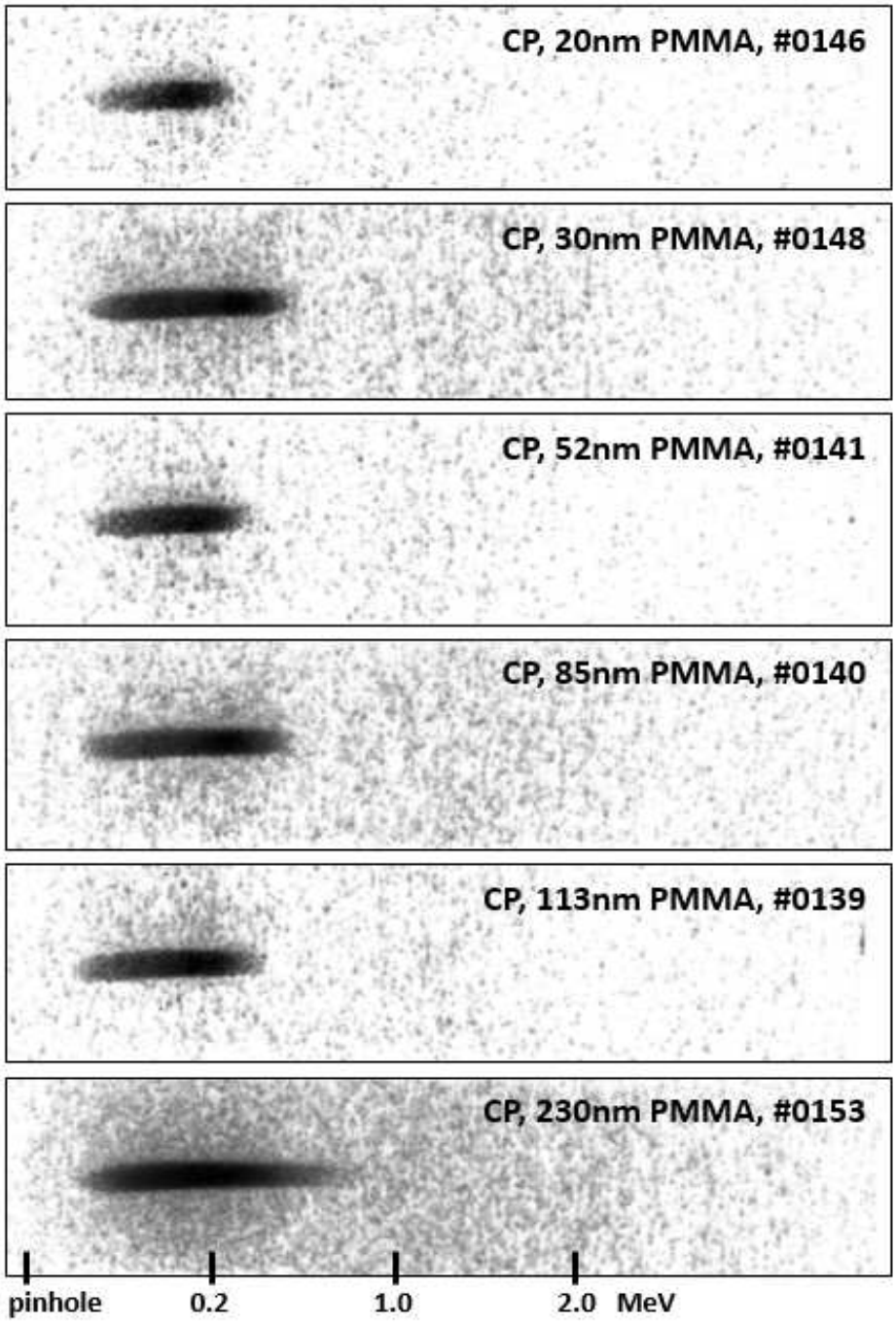

Figure 6.27: Raw data for the CP setup with PMMA targets.

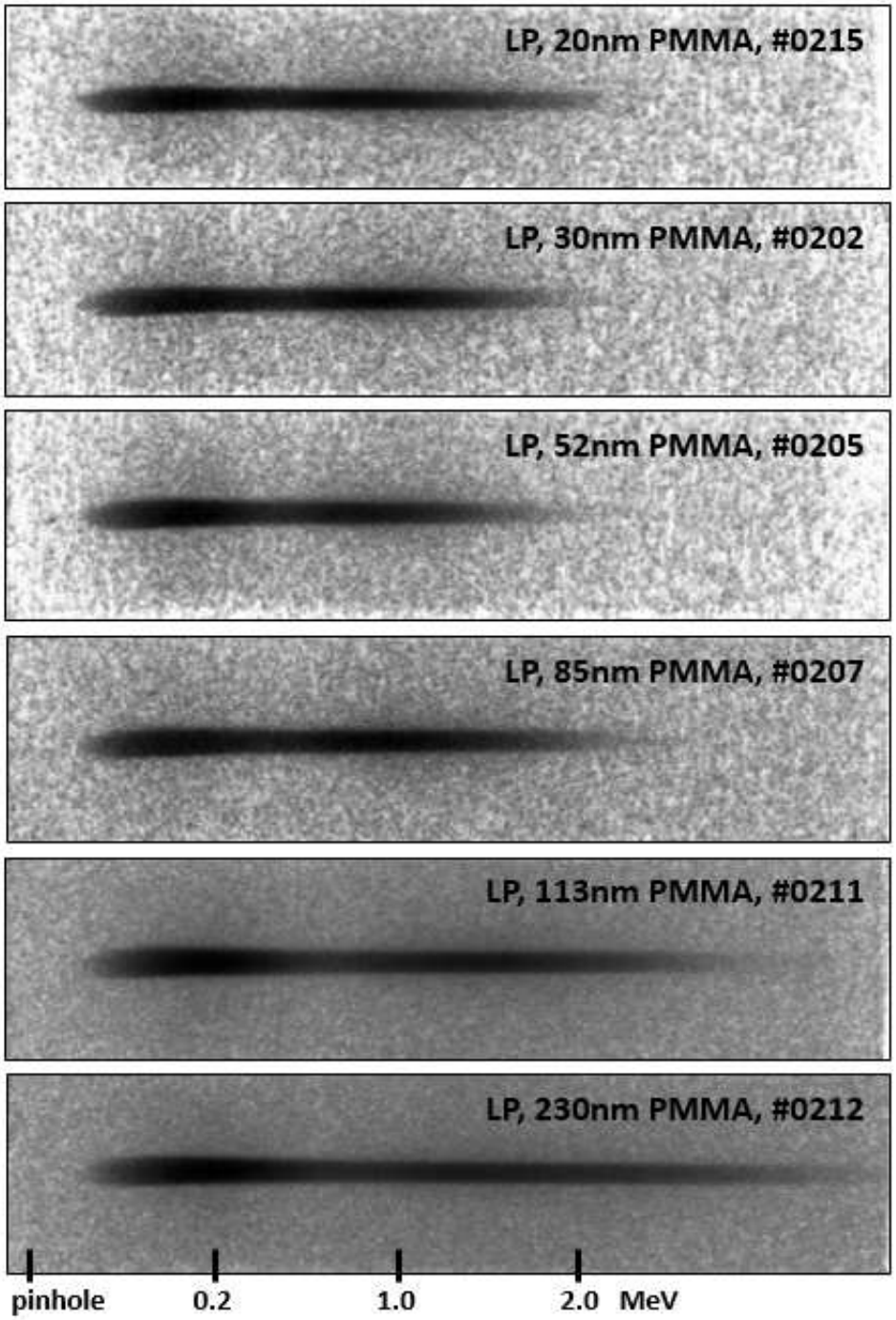

Figure 6.28: Raw data for the linearly polarized setup with PMMA targets.

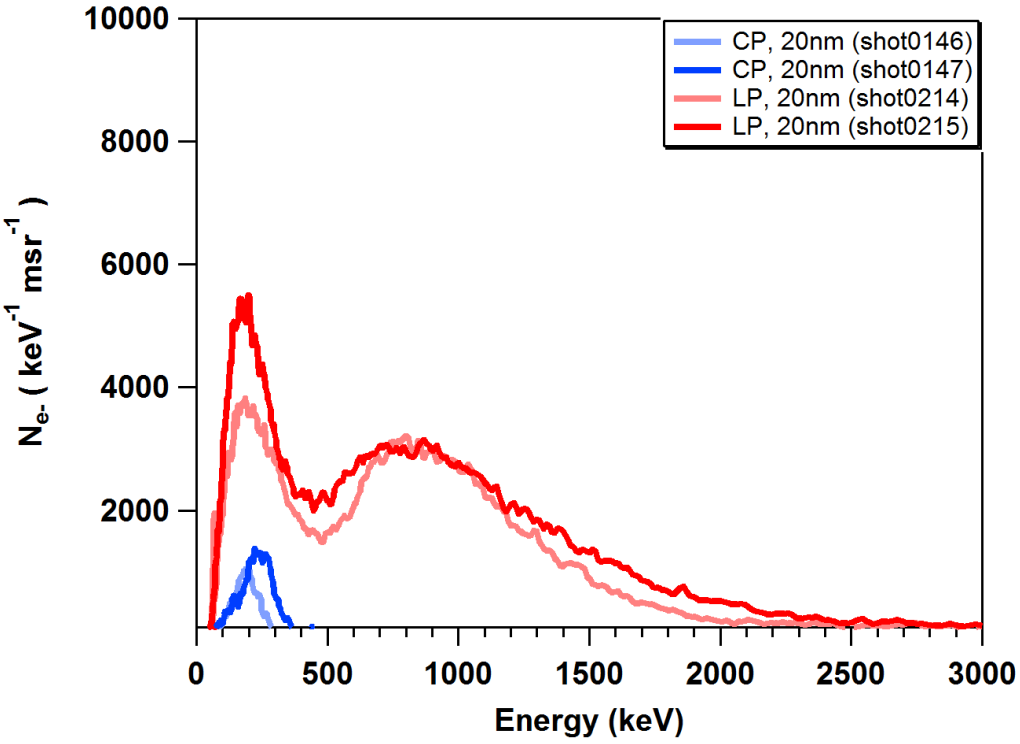

Figure 6.29: Electron energy spectrum for 20 nm PMMA targets.

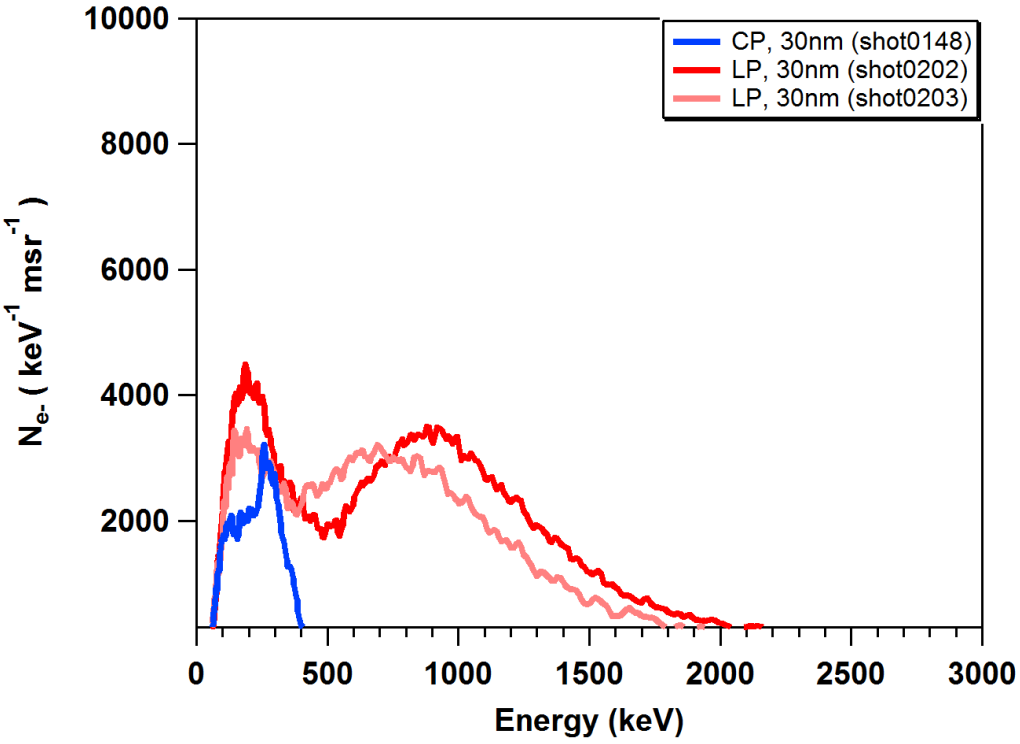

Figure 6.30: Electron energy spectrum for 30 nm PMMA targets.

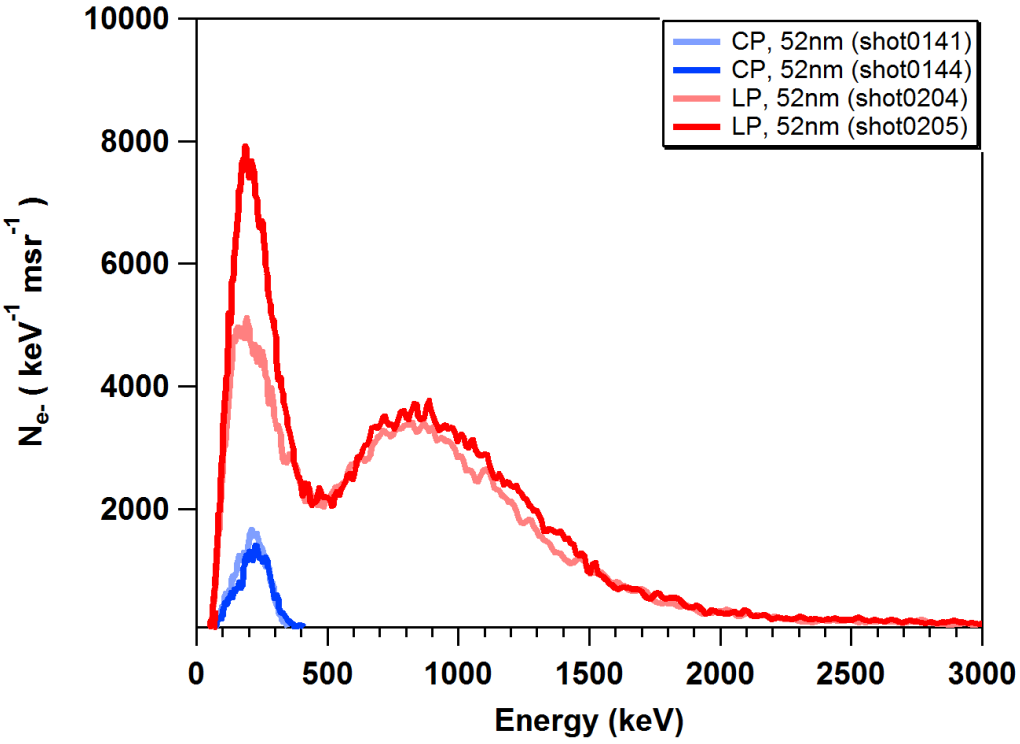

Figure 6.31: Electron energy spectrum for 52 nm PMMA targets.

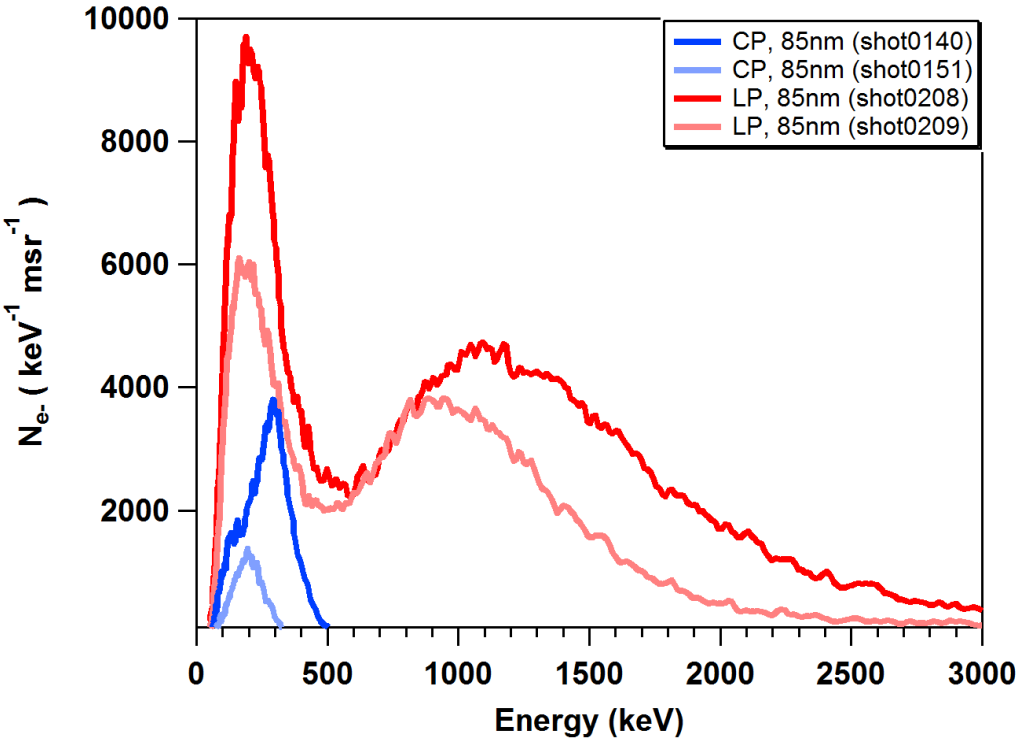

Figure 6.32: Electron energy spectrum for 85 nm PMMA targets.

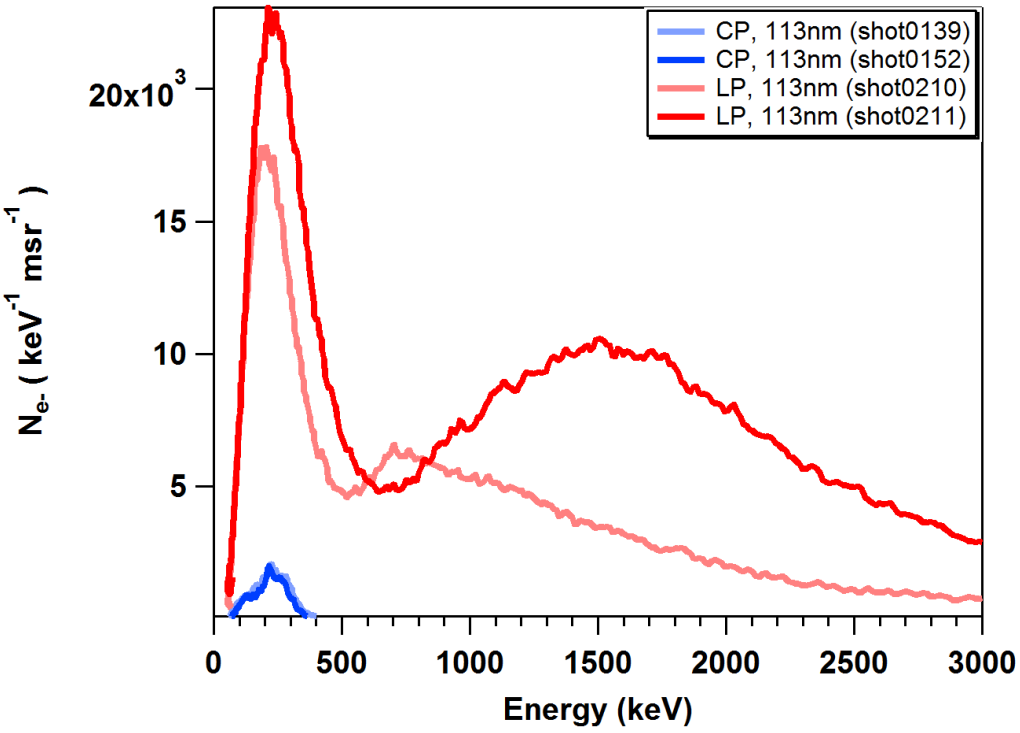

Figure 6.33: Electron energy spectrum for 113 nm PMMA targets.

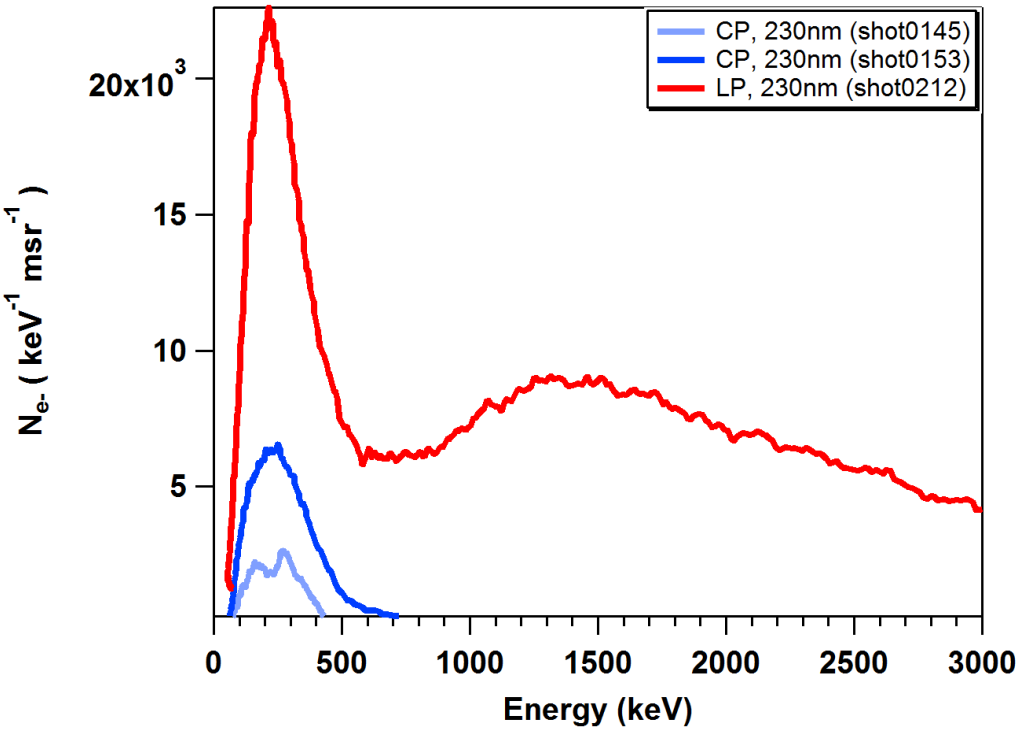

Figure 6.34: Electron energy spectrum for 230 nm PMMA targets.

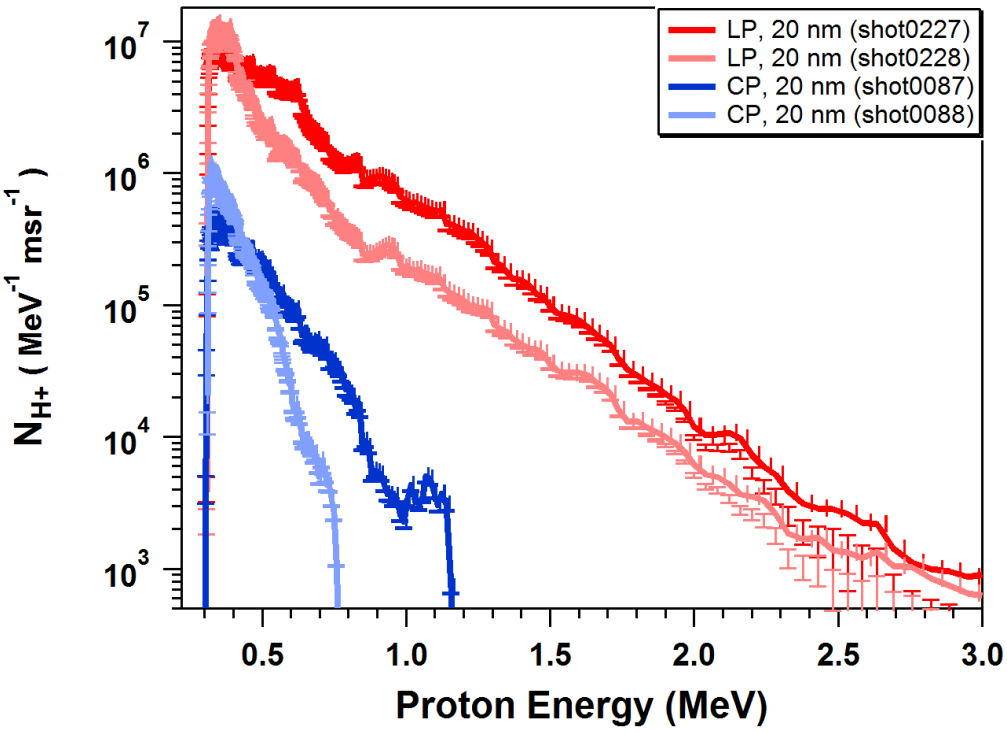

Figure 6.35: Proton energy spectrum for 20 nm PMMA targets.

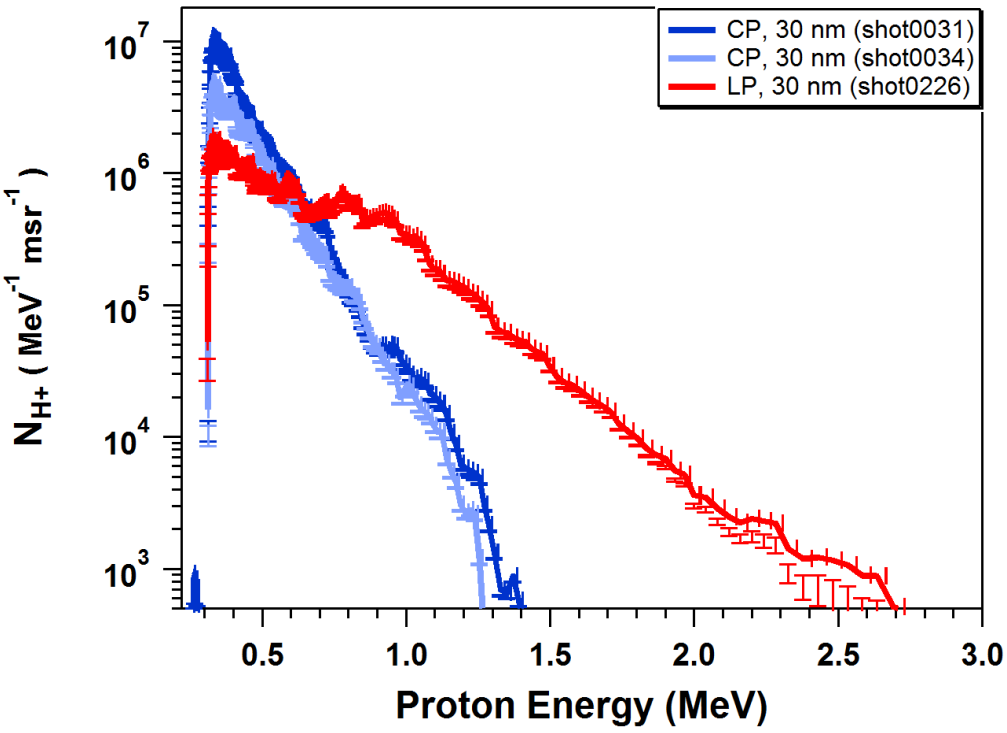

Figure 6.36: Proton energy spectrum for 30 nm PMMA targets.

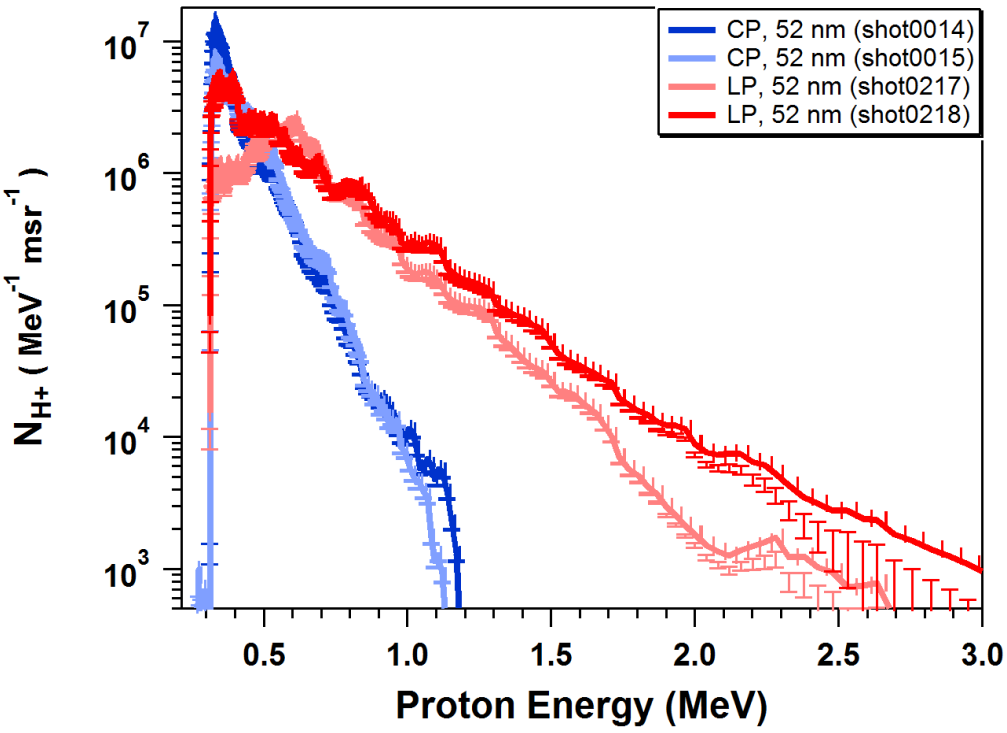

Figure 6.37: Proton energy spectrum for 52 nm PMMA targets.

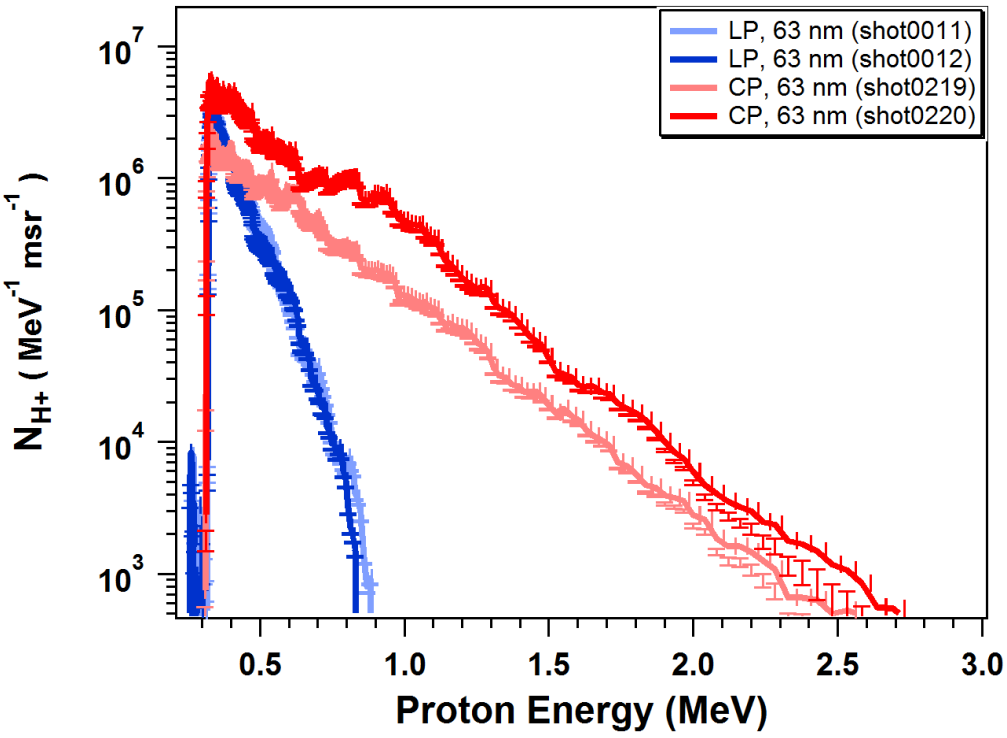

Figure 6.38: Proton energy spectrum for 63 nm PMMA targets.

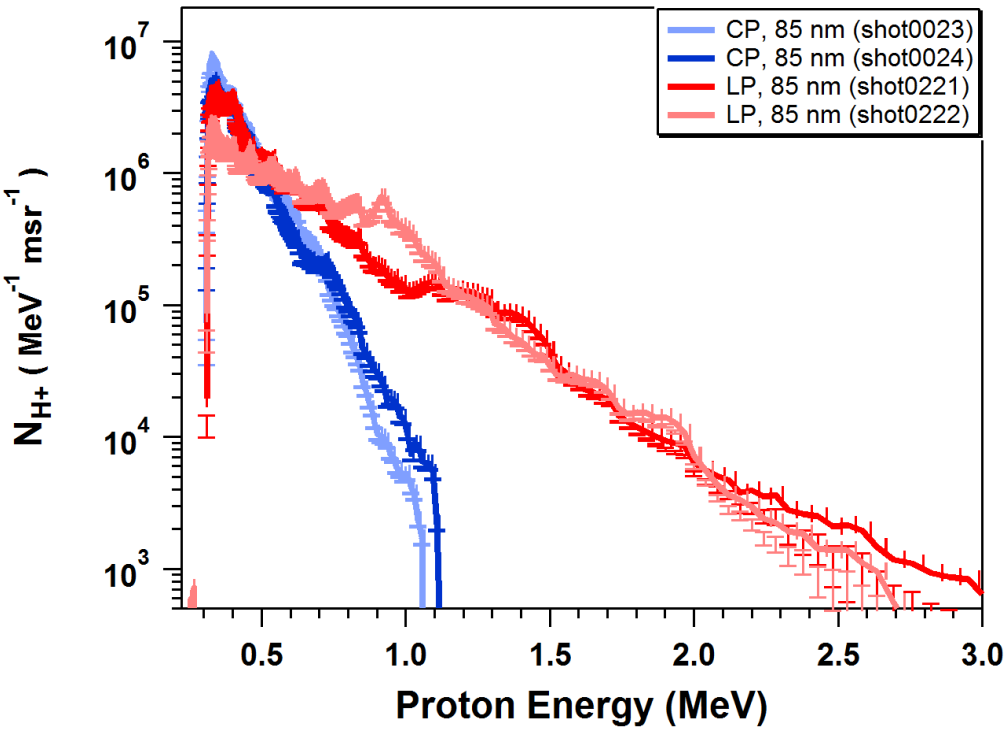

Figure 6.39: Proton energy spectrum for 85 nm PMMA targets.

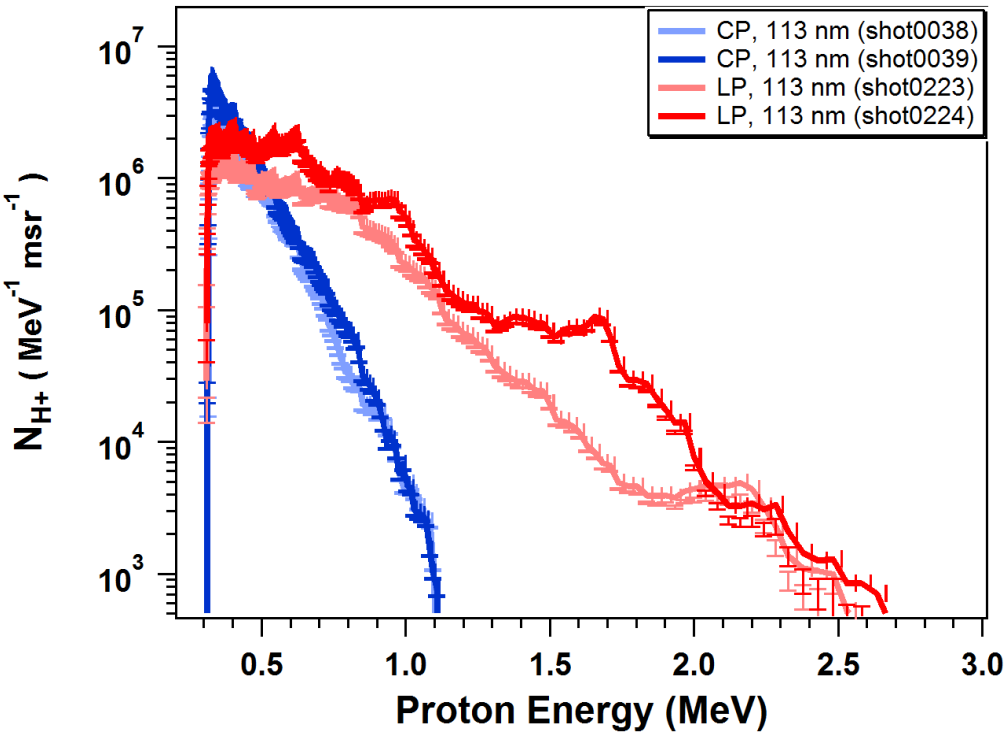

Figure 6.40: Proton energy spectrum for 113 nm PMMA targets.

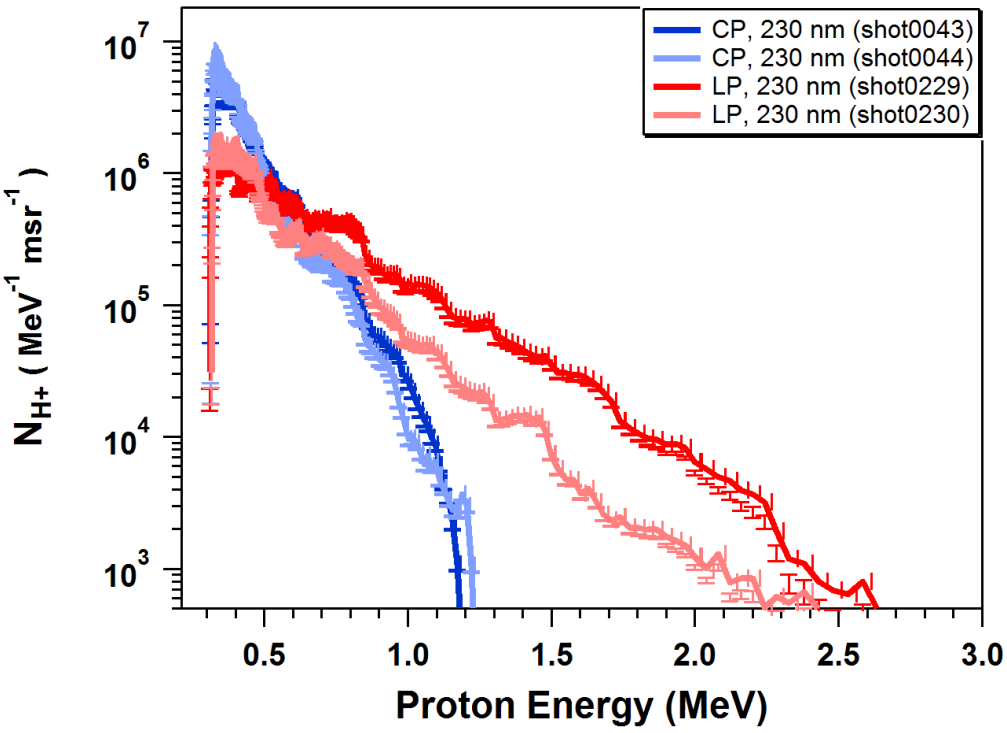

Figure 6.41: Proton energy spectrum for 230 nm PMMA targets.

6.3.5 EPOCH simulation

EPOCH is the abbreviation for Extendable PIC Open Collaboration project. EPOCH is open source PIC code for high energy density physics. EPOCH can utilizes the pseudoparticles in the cell so that the physical particles collected are represented to a smaller number of pseudoparticles. The fields generated by the motion of these pseudoparticles are calculated using a finite difference time domain technique on an underlying grid of fixed spatial resolution [39].

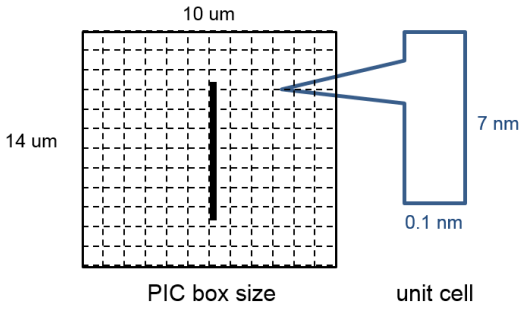

Figure 6.42: EPOCH cell size.

As shown in the figure 6.42, the PIC box size is defined over 10×14 μm. Each mesh cell size is defined 0.1 nm in z-axis and 7 nm in x-axis so that the physical condition of $(x_{max} - x_{min})/nx < \lambda_{Debye}$ is valid over the box while the particle tracking.

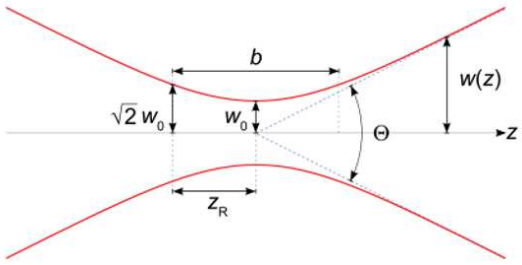

Figure 6.43: Gaussian beam parameters.

The practical laser parameters of the GHOST are employed to define the laser part of the input deck. As shown in the figure 6.43, the measured focal spot size in FWHM is defined as the beam waist and then the Rayleigh length can be defined $z_R = \pi w_0^2/\lambda_L$, the beam size is $w(z) = w_0\sqrt{1 + (z/z_R)^2}$.

On the other hand, the molecular formula of the PMMA $(C_5O_2H_8)_n$ are used to define each species of particle and their density. The total number of electron must satisfy total neutral condition of $n_e = n_H Z_H + n_C Z_C + n_O Z_O = n_H + 6n_C + 8n_O$ and this leads to the ratio of the number density of the Hydrogen, Carbon and Oxygen atoms with respect to the electron density as follow

$$\begin{cases} n_H &= 8\, n_{PMMA} = 0.146\, n_e \\ n_C &= 5\, n_{PMMA} = 0.093\, n_e \\ n_O &= 2\, n_{PMMA} = 0.037\, n_e \end{cases}$$

In the linearly polarized case, the direction of the E-field of the laser is defined on the xz-plane. Figure 6.44 shows the propagating linearly polarized gaussian beam on the xz-plane. On the other hand, 2 E-fields are defined on xz- and yz-planes in $\pi/2$ phase difference to define the circularly polarization which propagating along the z-axis. As shown in the figure 6.45 comparing with the linearly polarized, the oscillating intensity is vanished and the E-field intensity is decreased that satisfies $|\vec{E}_{LP}| = \sqrt{2}\,|\vec{E}_{CP}|$.

These 2 beams are incident in normal to the 20 nm thickness of the PMMA slab placed on z=0. From figure 6.46 to figure 6.49 show the time evolution of the electron and proton density for the linearly and circularly polarized beam respectively. As shown in the figure 6.46, linearly polarized beam heat up the target non-adibatically and the target undergoes thermal expansion in forward and backward direction. On the other hand, figure 6.48 shows that circularly polarized beam does not generate hot electrons by J $\times$

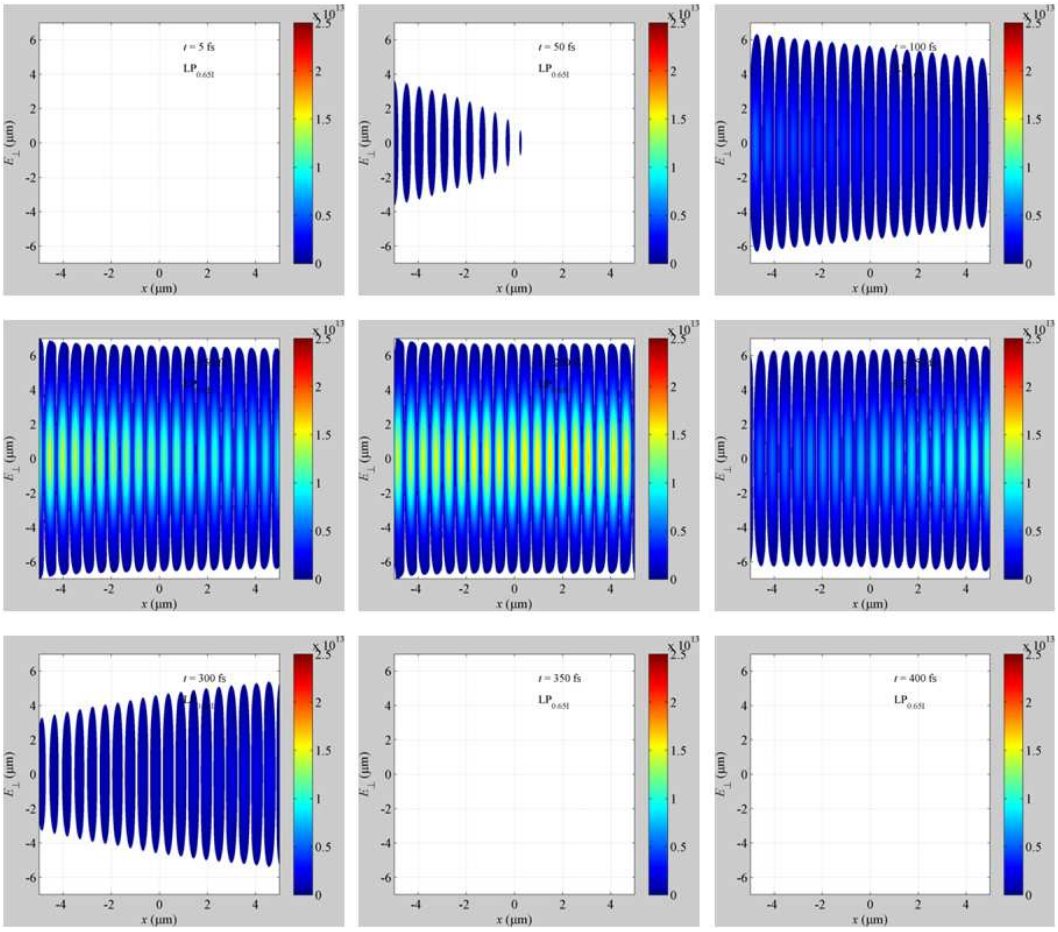

Figure 6.44: E field of the propagating linearly polarized laser.

B heating. Comparing in the same time scale in the figure 6.46 and figure 6.48, the electrons for the circularly polarized case just pushed by the laser pressure and they are just filed up ahead of the main beam. This dense electron layer pulls out the ions and accelerated them but this in a fashion piston like process occurs very smoothly and gently. Comparing the proton density evolution between figure 6.47 and figure 6.49, the circularly polarized

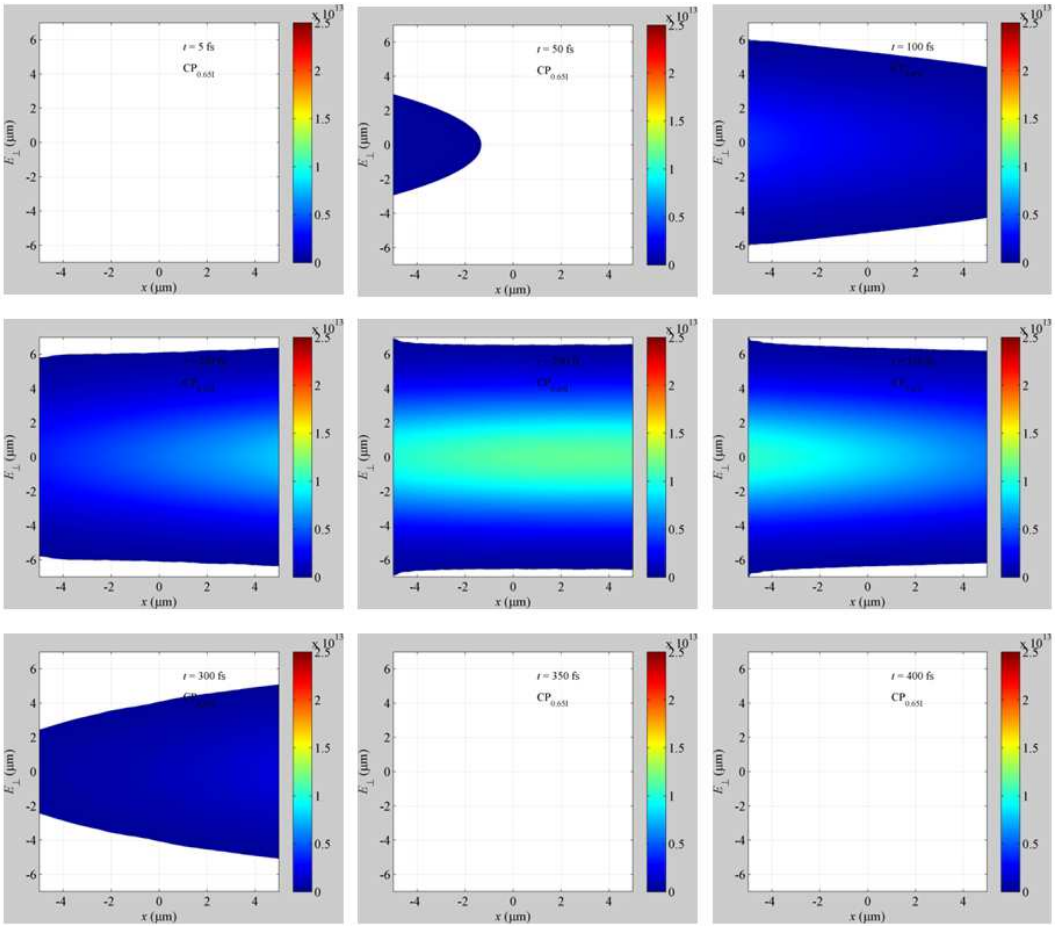

Figure 6.45: E field of the propagating circularly polarized laser.

beam accelerate protons in very dense layer than the linearly polarized beam. This is observed for other species of ions like carbon and oxygen in the PMMA target either.

The simulation energy spectrum results for the electron and proton are shown from figure 6.50 to figure 6.51. The red line is the energy spectrum detected at the target rear side and the magenta line is the energy spectrum

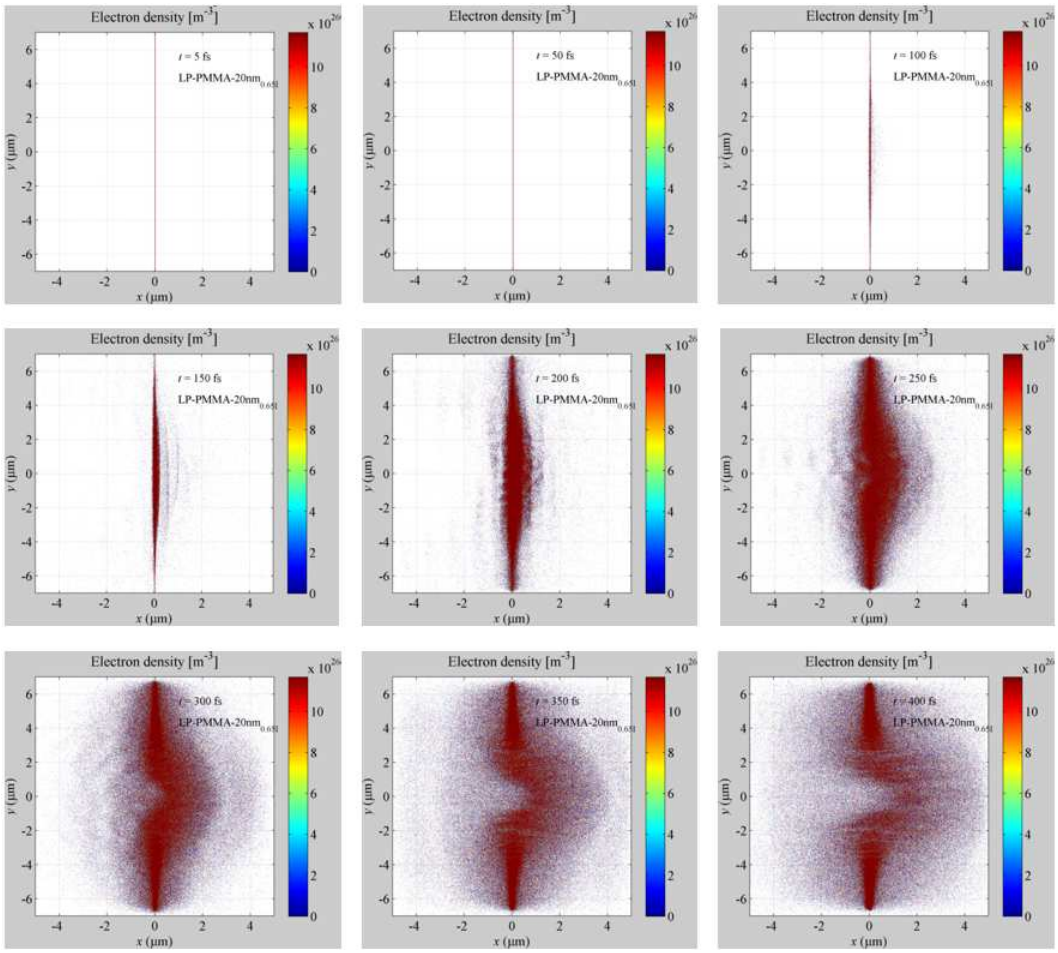

Figure 6.46: Electron density evolution for the linearly polarized beam with the 20 nm PMMA target.

of the particle detected at the target front surface side. The green is the summation of them. The results of the EPOCH simulation are not match with the experimental data very well. The cut-off energy for both particles are higher than the experimentally observed value. However, the results of the EPOCH simulation show that there are differeces between linearly and

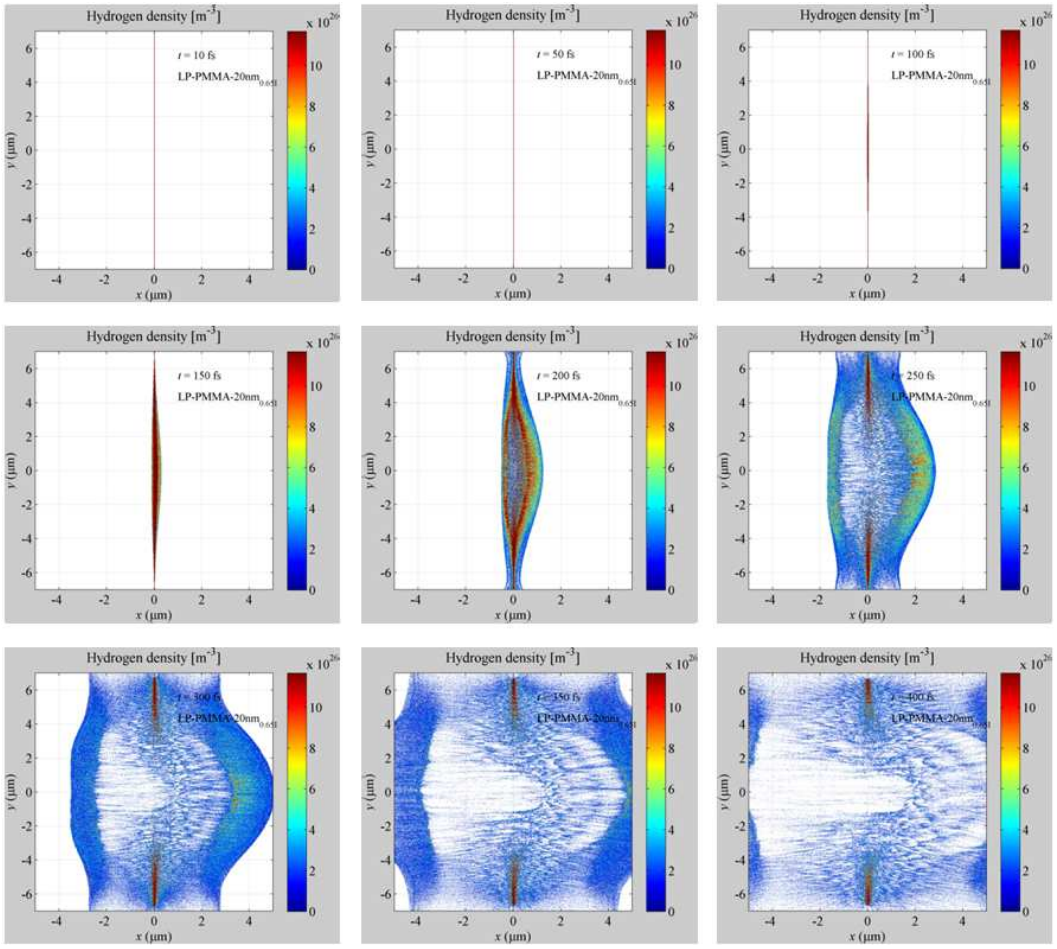

Figure 6.47: Hydrogen density evolution for the linearly polarized beam with the 20 nm PMMA target.

circularly polarized beam obviously and we have to extend the code in 3D to investigate more of the detail.

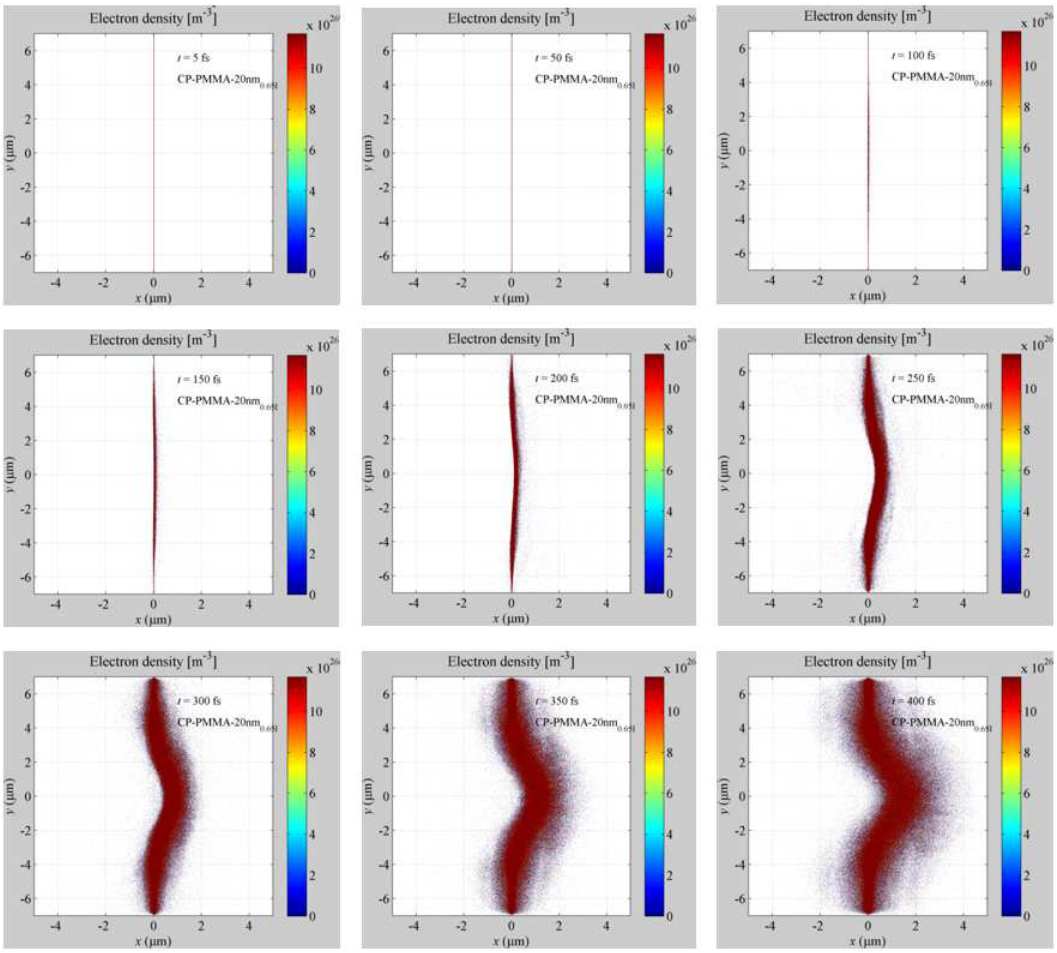

Figure 6.48: Electron density evolution for the circularly polarized beam with the 20 nm PMMA target.

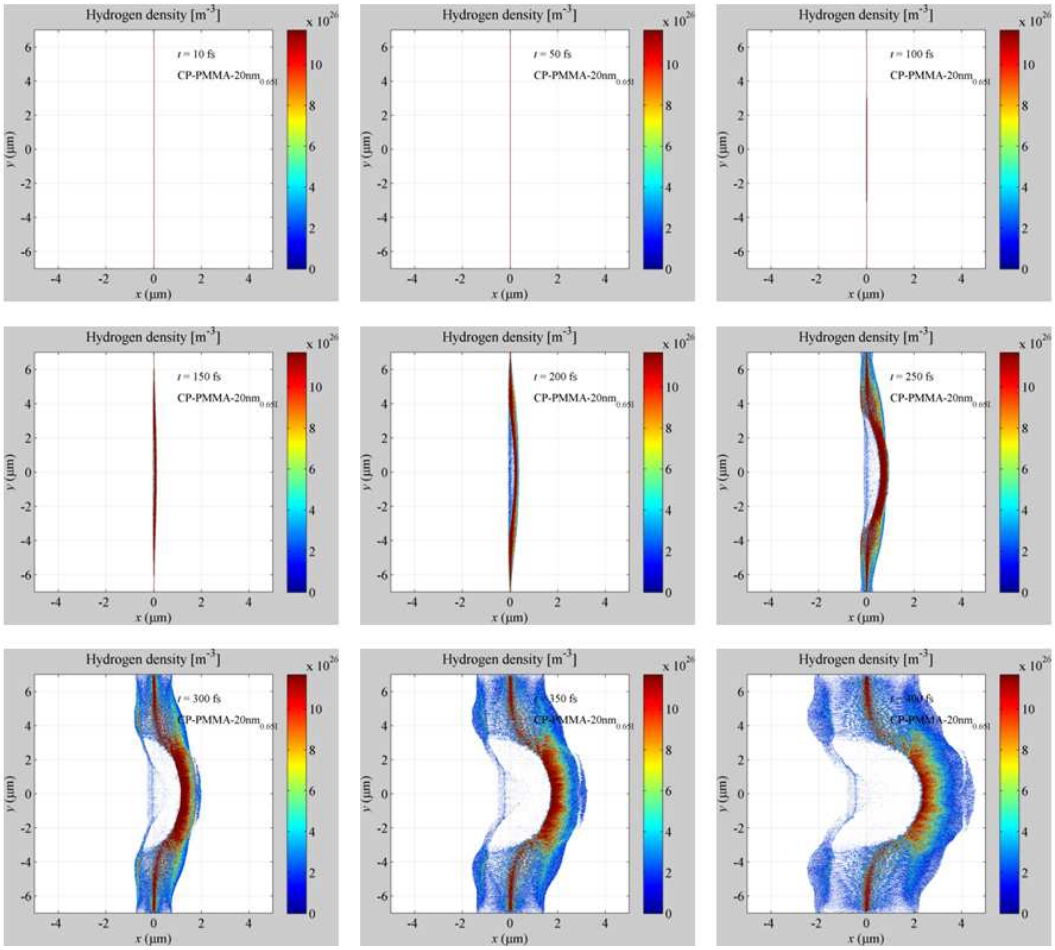

Figure 6.49: Hydrogen density evolution for the circularly polarized beam with the 20 nm PMMA target.

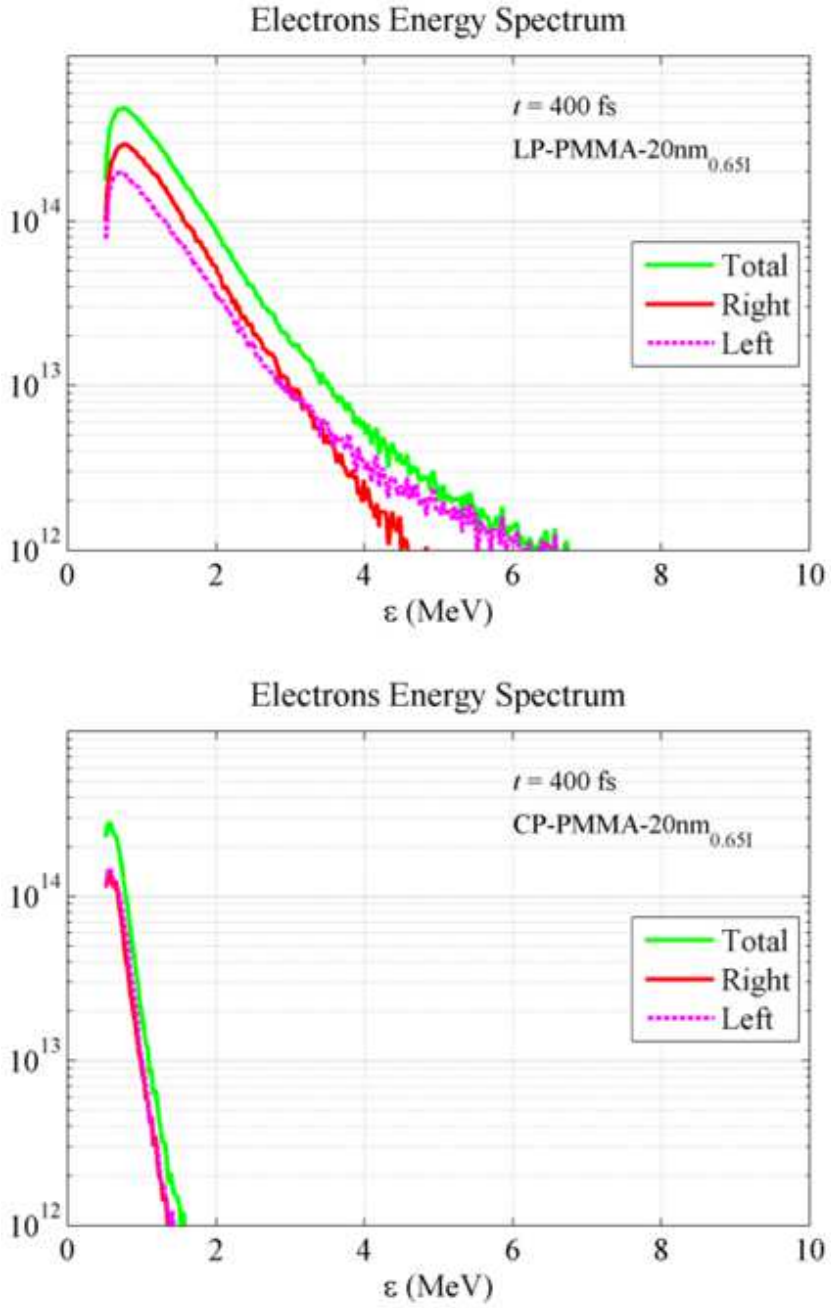

Figure 6.50: Electron energy sprctrum of 20nm PMMA target. Top is for the linearly polarized and bottom is for the circularly polarized beam.

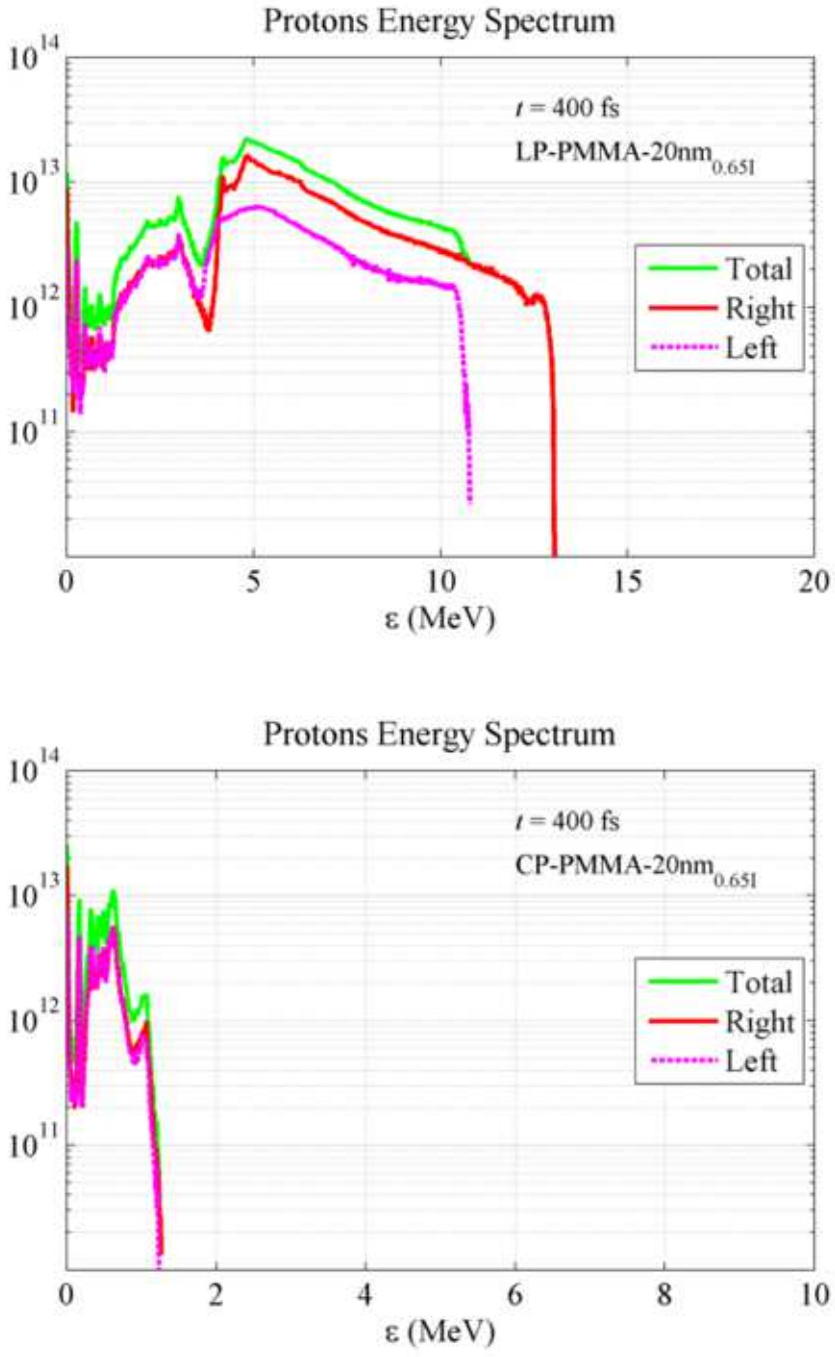

Figure 6.51: Proton energy sprctrum of 20nm PMMA target. Top is for the linearly polarized and bottom is for the circularly polarized beam.

Chapter 7

Summary

The generation of quasi-monoenergetic proton beam from plasma produced by the interaction of high intensity laser with solid target is one of the most important research area in the high energy density physics. The goal of this study is to investigate the laser driven protons acceleration experiments and find validation of the presented methods for the quasi-monoenergetic proton acceleration by other research groups.

One is the micro-dot target experiment. Micro-structured dot composed of hydrogen rich material have the potential of enriching the proton source in a spatial region that is coincident with the laser focal spot and can, therefore, sample only a small region of the various field gradients set up by the cloud of hot electrons. The experiment is carried out at the Texas Petawatt Laser Facility where the $f/3$ OAP mirror focuses 100 J in 110 fs laser beam to 10 μm in FWHM and generates 10^{21} W/cm^2 intensity on the target. The data from this experiment shows that suppressing hot electron generation is more important than manipulating the spatial distribution of the cold ions on the target rear surface.

The other experiment is the circularly polarized beam normal incident

on the ultra-thin target. The feasiblility for the quasi-monoenergetic ion beam is based on the RPA mechanism. To achieve the RPA dominant region, the laser intensity must higher than 10^{24} W/cm^2 for the linearly polarized beam. Unfortunately, this high of intensity is still beyond current cutting-edge of the laser technology. However, the RPA can be dominant at the 10^{21} W/cm^2 when the laser is circularly polarized. By suppressing the generation of the hot electron driven by J $\times$ B heating leads smooth acceleration of the electrons and that results the quasi-monoenergetic proton acceleration. Although the 10^{21} W/cm^2 intensity is achievable at petawatt laser facilities, the quarter waveplate is not compatible for the circularly polarization as the self focusing. Thus, we designed the combination of a periscope and metal mirror to generate the circularly polarized beam with the TW laser and study the suppression of the J $\times$ B heating effects experimentally. Comparing the circularly polarized beam with the linearly polarized beam, the effect of suppression of the J $\times$ B heating is observed from electron and proton energy spectrum data. And the suppression is not just by the decreased electric field by changing the polarization of the laser.

In spite of the less intensity for the RPA dominant regime, we present the experimental studies of ion acceleration driven by circularly polarized beam to observe the suppression of the hot electron generation driven by the J $\times$ B heating. And the experimental data make us to anticipate for the quasi-monoenergetic ion acceleration driven by circularly polarized beam with the 10^{21} W/cm^2 intensity where the RPA is dominant.

Appendices

Appendix A

Operation Procedure at the Microelectronics Research Center at J. J. Pickle Research Campus

A.1 Hood C16 - Piranha Cleaning

Purpose: To strip off the PR, general purpose cleaning prior to non-critical high temperature furnace processing (e.g.: doped tube, undoped tube, field oxide growth, annealing, or any LPCVD depositions). At least a piranha clean is necessary prior to any LPCVD step, unless the wafers are being *directly transferred* from one of the diffusion tubes without a time gap (an example for such a situation is polysilicon deposition performed immediately after the gate oxidation).

A.1.1 Procedure

1. Triple rinse the beakers for Hydrogen peroxide (H_2O_2) and Sulfuric acid (H_2SO_4)

2. Triple rinse the quartz beaker. (Note: The quartz beakers designated for RCA clean ONLY are labeled 'SC-1' and 'SC-2'. Never use the quartz beakers or the thermometers found inside these beakers for any purpose

other than the ones they have been designed for.)

3. Pour 800 *ml* of H_2O_2, followed by 1600 *ml* of H_2SO_4 (1:2 ratio).

4. Let the solution stand for 5 minutes, to enable the temperature of the reaction to build up (exothermic reaction).

5. Meanwhile, rinse your wafers in the wafer carrier along with a tweezer and a wafer handle in a quick dump.

6. Immerse the wafer carrier into the solution and let it stand for 8 minutes.

7. After the piranha clean, take the auto rinse.

8. Now, if you choose to, follow the clean by a dilute HF (preferably 40:1 dilution) dip to remove the chemical oxide on bare silicon (or polysilicon) that has formed during the cleaning.

9. you must aspirate ALL the chemical solution at the end of the processing. Note that the teflon aspirating pipes are capable of handling solutions upto 100 °C. Hence, you can aspirate the hot piranha solution anytime.

A.2 LPCVD Nitride - MRL

1. Log on to the tool using the LabAccess terminal.

2. Go to the recipe loader on the MRL control computer by selecting the apple and choosing process loader.

3. Select the nitride furnace (5-2).

4. Select the desired recipe (new recipes must be approved and created by the maintenance staff).

5. Enter the desired deposition time (current rates for standard recipes may be determined by checking the log book)

6. Enter run data (user, recipe, deposition time) in log book.

7. Enter MRL control password and select load recipe.

8. Open the tube status window (under the apple icon if not already open).

9. Open the nitride furnace window.

10. Select control button.

11. Select start.

12. Wait for load/unload step.

13. Place wafers in boat (this should be done on the load platform with clean tools and on cleanroom wipes to prevent contamination of the boat) including buffer wafers to ensure more uniform deposition on device wafers.

14. Transfer the boat into the furnace with the rod.

15. Close the furnace door.

16. Re-open the nitride furnace status window, select the control button, and select hold to remove the load/unload hold.

17. Hold the furnace door closed until the 10 second load/unload countdown is complete and the system has been pumping for an additional 5-10 seconds. This is essential for the furnace to establish a good vaccuum, and the furnace will abort if it fails.

18. Wait for the deposition to run automatically.

19. Wait for load/unload step.

20. Use rod to remove the boat from the furnace.

21. Close the furnace door.

22. Re-open the nitride furnace status window, select the control button, and select hold to remove the load/unload hold.

23. Hold the furnace door closed until the 10 second load/unload countdown is complete and the system has been pumping for an additional 5-10 seconds. This is essential for the furnace to establish a good vaccuum, and the furnace will abort if it fails.

24. Allow boat and wafers to cool while waiting for recipe to finish running.

25. After process is complete, reopen the process loader under the apple.

26. Select the nitride furnace.

27. Choose the idleLP recipe.

28. Enter MRL control password and select load recipe.

29. Open the nitride furnace status window.

30. Select control button.

31. Select start.

32. Unload the wafers again using cleanroom wipes and clean tools to prevent contamination to the boat.

33. Measure the nitride deposition thickness.

34. Enter the nitride deposition thickness in the log book.

35. Log off of the tool using the LabAccess terminal.

A.3 Woollam Ellipsometer

1. Log on the tool using the LabAccess Terminal

2. Power up the tool

   (a) Turn on the lamp ignition D2 located on the M-2000DI. Lamp power QTH should be on at all times

   (b) The EC-400 should be on at all times

   (c) The computor monitor should be on at all times

3. If the software is not launched already, double click WVASE32TM icon on the desktop. 6 windows appear: Model, Generated Data, Fit, Experimental Data, Hardware and Graph

4. Click anywhere in the Hardware window and click Initialize

5. In the WVASE32TM Hardware log window enter a user name (MRC by default) and click Ok

6. Place sample on stage. Make sure that the light

   (a) is aligned with the aperture in the Output unit (MQD-160)

   (b) is focused on the sample. This can be done by placing a piece of paper on the sample to locate the light and algining the sample with it

7. Turn the vacuum on. The switch is located on the lower left hand side of the Sample Stage.

8. on the Setup menu select Load Sample

9. "Mount new Sample" window appears. Click Ok "Hardware: Align" window appears with a red cross.

10. Center the cross at the origin and in between the grey bands using the 2 knobs located on the front and the right sides of the sample stage. Press "Esc" on the keyboard when the red cross is close to the center

11. Answer "Yes" to "Repeat tilt-alignment and Z-alignment steps?" to improve the alignment. Repeat step 10. Select "No" otherwise

12. The error message "Insufficient intensity for Auto Alignment of Sample Z-stage" might appear. In this case, repeat steps 6 through 10 again to align the sample better.

13. "The sample load sequence is complete". Click Ok

14. On the Acquire data menu select Spectroscopic Scan. The "V.A.S.E Scan" window appears. Choose range and increment of angles. Typical values for different materials are listed below

    (a) Metal, dielectrics" 60 to 75 degrees, increment = 5 °

    (b) Silicon: 40 to 55 degrees, increment = 5 °

    (c) "Revs/meas" box can be set to 10 (40 for better precision)

    Click "Ok" after setting the required values.

15. Select Yes/No to the "Save experimental data?" inquiry. Select "No" (by default). If "Yes" is selected, save the data in the "DAT" folder.

16. Build model for the sample

    (a) Click anywhere on the "Model" window

    (b) Select AddLayer. A window appears, highlight the material of interest form the list and click "Ok". The Layer window appears.

Enter the desired thickness, select fit and click "Ok". If the selected material is for the bulk, 1mm is a typical thickness value and the "fit" option is not active.

(c) add an other layer by repeating step 16.(b)

17. Click anywhere in the "Generate data" window and select Generate data

18. Click anywhere in the "Fit" window. On Normal fits menu select Normal fit

19. Repeat steps 16 to 18 in order to get a good fit. i.e. MSE ¡ 10 in the Fit window

20. To save the environment, click on the Global menu and select Save current environment. The model can be modified and analyzed later without having to go through steps 6 to 15 again

21. Turn off vacuum and unload the sample

22. Log out of the tool using the LabAccess Terminal

A.4 RIE Etcher - 790 Plasma Therm #2

1. Log on to the tool using the LabAccess terminal.

2. Log into the system software.

3. Select the chamber to be used. Utilities → Select Active Chamber → chose either the left or right chamber

4. Vent chamber : Utilities → Vent

5. Clean the chamber before the first process is started. Wipe the walls and any quartz wafer holders with Acetone and then IPA. Wipe the graphite susceptor with IPA.

6. Run a 10 to 30 minute oxygen clean, Pressure = 200 mTorr, O_2=18 sccm, power = 300 W.

7. Vent chamber : Utilities → Vent

8. Place your wafer in the chamber.

9. Firmly hold the lid to the chamber down and evacuate the chamber by choosing: Utilities → Pump Chamber → LoVacuum. Once the chamber is under vacuum you may stop holding the lid down. System status will now be ON & STANDBY.

10. To edit a recipe choose: Process → Edit, now choose the recipe from the list. Edit the recipe and save it before exiting.

11. To load a recipe choose: Process → Load, now choose the recipe. System Status will change to ON & READY. The loaded recipe will show in the Process box at the lower right.

12. Run the loaded recipe by clicking the RUN button at the lower right.

13. Once your recipe is finished, vent the chamber, remove your sample and pump the chamber down again.

14. ALWAYS CLOSE GATES. Always close the gate between the chamber and the pumps before logging off or when leaving the system idle for over 10 minutes. When the gate is left open pump oil back streams into the chamber. Choose: Utilities → Close Gates.

15. Log off of the system software.

16. Log off of the tool using the LabAccess terminal.

A.5 Hood H18 - KOH Etching

1. Log on to the tool using the LabAccess terminal.

2. Cover hotplate areas with the provided covers.

3. Fill the cascade rinser with DI water and wait until the resistivity is at least 12 MW-cm. This should only take a few minutes. If it does not reach 12 MW-cm, dump tank and restart.

4. Prepare the Piranha solution. Pour 825 ml Hydrogen Peroxide into the rectangular quartz tank and then add 1650ml the Sulfuric Acid. If you are processing small samples that do not require this much chemical, please use the smallest amounts of chemical necessary in the ratio (1 part Hydrogen Peroxide : 2 parts Sulfuric Acid) to complete this etch. Cover the piranha beaker with a Teflon cover and allow the solution to sit for 5 minutes.

5. Place wafers into the Piranha solution for 8 minutes.

6. When Piranha clean is completed, place the wafers in the cascade rinser and perform two 5-cycle rinses.

7. Dump cascade rinse and remove wafers unless performing the optional HF native oxide etch.

8. Optional HF etch:

   (a) Pour 1600 ml of DI water into the polypropylene tank in the hood and add 80 ml of 49% Hydroflouric acid.

   (b) Put the wafers into the HF solution until the wafer back de wets (20 seconds).

   (c) Place the wafers back into the full cascade tank for rinsing.

   (d) Perform one 5-cycle rinses. The resistively should reach 12.5 MW-cm. If it does not, you have the option to perform additional 5-cycle rinses.

9. If you are drying your wafers by hand, remove them from the cascade tank and carefully blow them dry with the N_2 gun.

10. If you are using a vertical shaft spin rinser dryer (SRD) to dry your wafers, you will need to use two carriers of equal size and weight to balance the load during spinning. Load an equal number of dummy wafers into one of the carriers and place it into the SRD. Remove the processed wafers from the cascade tank and place the second carrier into

the SRD directly opposite the dummy wafer carrier. Please do not use SRDs in other bays as this can cause cross contamination.

11. Initiate SRD cycle.

12. Turn on the aspirator and plenum rinse to remove the Piranha. If an HF dip was used, aspirate of the HF. When the acid is completely removed, place the aspirator into DI water and run for 2 minutes.

13. Fill and dump each acid container with DI water three times.

14. Turn off the aspirator and plenum rinse.

15. When the SRD is finished, very carefully lift the SRD lid and remove the wafers.

16. DONT FORGET to turn off the DI water taps, rinse beakers, clean-up the hood deck (including covers and dividers) and any empty chemical bottles. Be sure to rinse your gloves.

17. Log off of the tool using the LabAccess terminal.

A.6 Denton DV - 502A Thermal Evaporator

1. Check to be sure the power is turned off.

2. Turn off High-Vacuum Gauge before venting.

3. Turn #4 knob to "Auto-Vent".

4. After pressure reaches atmospheric, open chamber and load sample/evaporation source. There are 4 positions available to mount crucibles (refer the figure on the machine)

5. Close chamber door and purge by turning #4 to "Auto-Pump". When the high-vac indicator light turns on, turn on the high-vacuum gauge.

6. After reaching desired vacuum, select the evaporation source position with the appropriate selector knob. The three position on the left are controlled by #6 and the two on the right by #7.

7. Turn on the power using #1 or #2 for the left or right ositions, respectively.

8. SLOWLY increase the current with the corresopnding knob (#8 or #9) while monitoring the evaporation source for heating.

9. The thickness indicators can be setup similarly to the Denton Explorer system for thickness monitoring.

10. Upon completion, turn the current to zero, turn off power, turn off high-vacuum gauge, and turn #4 to "Auto-Vent".

11. Remove sample/materials, close chamber door, and turn #4 to "Auto-Pump"

Appendix B

Pulse duration calculation from the 2nd order Auto-correlation Measurement of the GHOST

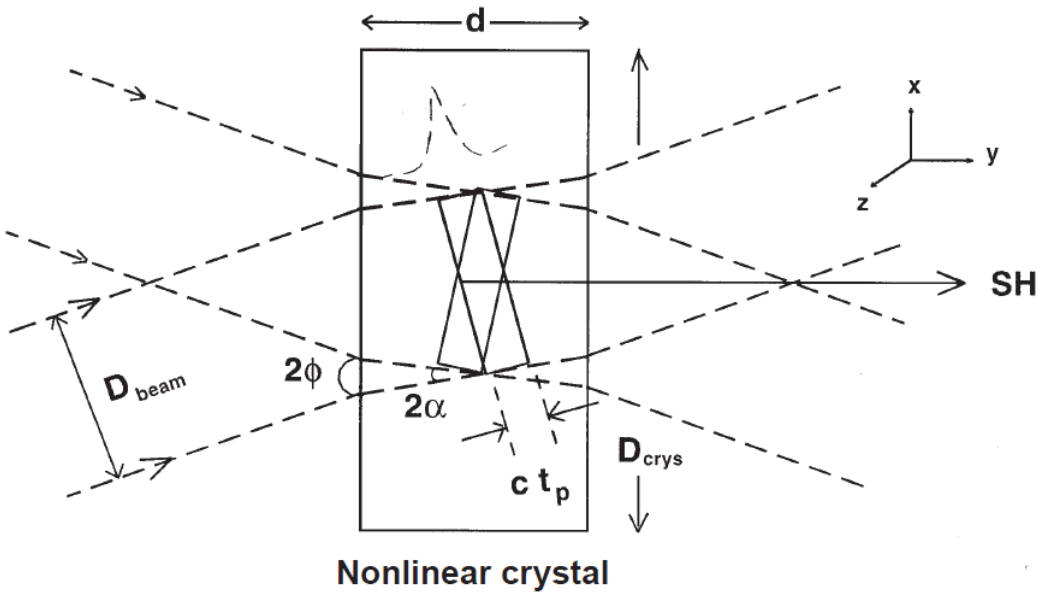

Figure B.1: Schematic of the 2nd order autocorrelation. [49]

In[20]:=
```
c = 299 792 458 ; (*in m/s*)
(*N1=(47.94+47.723)/2*) (*FWHM in Pixel, avg*)
N1 = 69.334;
Δx = 160 * 10^-6; (* in um*)
Δp = (571.47 - 60.837); (* in px*)
Δτ = N[2 * Δx / c ];(*in sec*)
R1 = Δτ / Δp ;(*in fs/px*)
Δτ1 = N1 * R1;(*in sec*)
Δτ_FWHM = Δτ1 / √2 (*√2 for Gaussian fit. it will be 1.3 for sech^2*)
```

Out[27]= 1.02483×10^{-13}

Figure B.2: GHOST laser pulse duration calculation from the 2nd order autocorrelation data data

Appendix C

EPOCH input deck file

C.1 LP, 20nm PMMA target

```
begin:constant
  GHOST_laser_lambda = 1.054 * micron
  # E=1.8J, D=6um in FWHM
  GHOST_laser_intensity = 5.5e19
  GHOST_laser_omega = 2.0 * pi * c / GHOST_laser_lambda
  # wave length for GHOST_laser_lambda (i.e. 3.51577*10^-15 sec)
  GHOST_laser_time = 2.0 * pi / GHOST_laser_omega
  # return the critical density for the given frequency
  n_crit = critical(GHOST_laser_omega)
  # PMMMA electron number density (number of electrons per cc)
  n_PMMA=4.3978e23
  den_max = n_PMMA * 1.0e6 # density in 1/m^3

  #rhomax = 0.8 * n_crit
  #scale_x = 20 * micron
  #las_scale_y = 8 * micron
  #xmin = -4 * micron

  # Gaussian Beam stuff
  #wz = w0 * sqrt(1+(x_start/rayleigh_range)^2)
  #radius_of_curvature = x_start * (1.0+(rayleigh_range/x_start)^2)

  xf = 5.0 * micron # distance of the focal spot from the left boundary
  w0 = 3.6034 * micron # width of the beam in the focal spot
  rayl=pi*w0^2/GHOST_laser_lambda #Rayleigh length
  sG = xf/rayl
  wb = w0*sqrt(1+sG^2) # beam width at the left boundary

end:constant


begin:control
nx = 10000
    ny = 2000
# npart = 300*ny*20

# size of domain in meter. From milli to atto is available as a scale factor
x_min = -5 * micron
x_max = -x_min
        y_min = -7 * micron
        y_max = -y_min
```

```
# simulation time in second
t_end = 400 * femto

        dlb_threshold=0.4
end:control


begin:boundaries
  bc_x_min = simple_laser
  bc_x_max = open
  bc_y_min = open
  bc_y_max = open
end:boundaries



begin:laser
  boundary = x_min
 #intensity at the boundary
  intensity_w_cm2 = 0.65*GHOST_laser_intensity / sqrt(1+sG^2)
  lambda = GHOST_laser_lambda
  # temporal profile for GHOST of FWHM=115fs
  t_profile=gauss(time,173e-15,69.065e-15)
  #transverse profile at the left boundary
  profile=exp(-((y/wb)^2))
  phase=sG*((y/w0)^2)/(1+sG^2)
  pol_angle = 0
end:laser



begin:output
  name = restart_dumps
  dt_snapshot=200.0e-15
  restartable=T
end:output


begin:output
  name = e_fields
  file_prefix = e_fields
  #number of timesteps between output dumps
  dt_snapshot=5.0e-15
#Number of dt_snapshot between full dumps
#  full_dump_every=200
#  restart_dump_every=200
#  force_final_to_be_restartable=T

  #Properties on grid
  grid=always
  ex=always + single
  ey=always + single
  ez=always + single
end:output
```

```
begin:output
  name = b_fields
  file_prefix = b_fields
  #number of timesteps between output dumps
  dt_snapshot=5.0e-15
  #Properties on grid
  grid=always
  bx=always + single
  by=always + single
  bz=always + single
end:output


begin:output
  name = dens
  file_prefix = dens
#  #number of timesteps between output dumps
  dt_snapshot=5.0e-15
#  #Properties on grid
  grid=always
  number_density=always + no_sum + single + species
end:output


begin:output
  name = ejected
  file_prefix = ejected

#  #number of timesteps between output dumps
  dt_snapshot=5.0e-15

  ejected_particles = always + single
#  px = always + single
#  py = always + single
#  particle_weight = always + single
#  charge = always + single
end:output


begin:output
  name = DF
  file_prefix = DF

#  #number of timesteps between output dumps
  dt_snapshot=5.0e-15

  distribution_functions=always + single + no_sum
  particle_probes=never
  absorption = always + no_sum
#distinguish energy in laser and particle
  total_energy_sum = always + no_sum
end:output


begin:dist_fn
```

```
  name=en
  ndims=1
  dumpmask=always
  direction1=dir_en
  #range is ignored for spatial coordinates
  range1=(0,0)
  #resolution is ignored for spatial coordinates
  resolution1=2500
  include_species:Electron
  include_species:Hydrogen
  include_species:Carbon
  include_species:Oxygen
end:dist_fn

begin:dist_fn
  name=px
  ndims=1
  dumpmask=always

  direction1=dir_px

  #range is ignored for spatial coordinates
  range1=(0,0)

  #resolution is ignored for spatial coordinates
  resolution1=2500

  include_species:Electron
  include_species:Hydrogen
  include_species:Carbon
  include_species:Oxygen
end:dist_fn


#-------------------------------------------------------------------------
#PMMA: C5O2H8
#number of electrons per molecule=(5*6)+(2*8)+8=30+16+8=54
#number of ions per molecule=5+2+8=15
#total number of particles per molecule=54+15=69
#-------------------------------------------------------------------------

begin:species
  name=Electron
  charge=-1.0
  mass=1.0
# frac is not compatible with npart
#  frac=54/69
  npart_per_cell = 100
  dump=T
  temp=0
  density_min = 0.1 * den_max

  density = den_max
  density = if(rho(Electron) gt den_max,den_max,rho(Electron))
  density = if(x gt 0.02*micron,0,rho(Electron))
  density = if(x lt 0*micron,0,rho(Electron))
```

```
  density = if(y gt 7*micron,0,rho(Electron))
  density = if(y lt -7*micron,0,rho(Electron))
end:species

begin:species
  name=Carbon
  charge=6.0
  mass=1836.2*(12.011/1.01)
#  frac=5/69
  npart_per_cell = 30
  dump=T
  temp=0
#  density = density(Electron)*5*6/54
  density = density(Electron)*0.093
end:species

begin:species
  name=Oxygen
  charge=8.0
  mass=1836.2*(15.999/1.01)
#  frac=2/69
  npart_per_cell = 30
  dump=T
  temp=0
#  density = density(Electron)*8*2/54
#  density = density(Electron)/8
  density = density(Electron)*0.037
end:species

begin:species
  name=Hydrogen
  charge=1.0
  mass=1836.2
#  frac=8/69
  npart_per_cell = 100
  dump=T
  temp=0
#  density = density(Electron)*8*1/54
#  density = density(Electron)
  density = density(Electron)*0.146
end:species
```

C.2 CP, 20nm PMMA target

```
begin:constant
  GHOST_laser_lambda = 1.054 * micron
  # E=1.8J, D=6um in FWHM
  GHOST_laser_intensity = 5.5e19
  GHOST_laser_omega = 2.0 * pi * c / GHOST_laser_lambda
  # wave length for GHOST_laser_lambda (i.e. 3.51577*10^-15 sec)
  GHOST_laser_time = 2.0 * pi / GHOST_laser_omega
  # return the critical density for the given frequency
  n_crit = critical(GHOST_laser_omega)
  # PMMMA electron number density (number of electrons per cc)
```

```
  n_PMMA=4.3978e23
  den_max = n_PMMA * 1.0e6 # density in 1/m^3

  #rhomax = 0.8 * n_crit
  #scale_x = 20 * micron
  #las_scale_y = 8 * micron
  #xmin = -4 * micron

  # Gaussian Beam stuff
  #wz = w0 * sqrt(1+(x_start/rayleigh_range)^2)
  #radius_of_curvature = x_start * (1.0+(rayleigh_range/x_start)^2)

  xf = 5.0 * micron # distance of the focal spot from the left boundary
  w0 = 3.6034 * micron # width of the beam in the focal spot
  rayl=pi*w0^2/GHOST_laser_lambda #Rayleigh length
  sG = xf/rayl
  wb = w0*sqrt(1+sG^2) # beam width at the left boundary

end:constant


begin:control
nx = 10000
    ny = 2000
# npart = 300*ny*20

# size of domain in meter. From milli to atto is available as a scale factor
x_min = -5 * micron
x_max = -x_min
        y_min = -7 * micron
        y_max = -y_min

# simulation time in second
t_end = 400 * femto

        dlb_threshold=0.4
end:control


begin:boundaries
  bc_x_min = simple_laser
  bc_x_max = open
  bc_y_min = open
  bc_y_max = open
end:boundaries



begin:laser
  boundary = x_min
 #intensity at the boundary, 35% beam loss in the compressor
  intensity_w_cm2 = 0.325*GHOST_laser_intensity / sqrt(1+sG^2)
  lambda = GHOST_laser_lambda
  # temporal profile for GHOST of FWHM=115fs
  t_profile=gauss(time,173e-15,69.065e-15)
  #transverse profile at the left boundary
```

```
  profile=exp(-((y/wb)^2))
  phase=sG*((y/w0)^2)/(1+sG^2)
  pol_angle = 0
end:laser


begin:laser
  boundary = x_min
 #intensity at the boundary
  intensity_w_cm2 = 0.325*GHOST_laser_intensity / sqrt(1+sG^2)
  lambda = GHOST_laser_lambda
  # temporal profile for GHOST of FWHM=115fs
  t_profile=gauss(time,173e-15,69.065e-15)
  #transverse profile at the left boundary
  profile=exp(-((y/wb)^2))
  phase=sG*((y/w0)^2)/(1+sG^2) + pi/2.0
  pol_angle = pi/2.0
end:laser



begin:output
  name = restart_dumps
  dt_snapshot=200.0e-15
  restartable=T
end:output


begin:output
  name = e_fields
  file_prefix = e_fields
  #number of timesteps between output dumps
  dt_snapshot=5.0e-15
#Number of dt_snapshot between full dumps
#  full_dump_every=200
#  restart_dump_every=200
#  force_final_to_be_restartable=T

  #Properties on grid
  grid=always
  ex=always + single
  ey=always + single
  ez=always + single
end:output


begin:output
  name = b_fields
  file_prefix = b_fields
  #number of timesteps between output dumps
  dt_snapshot=5.0e-15
  #Properties on grid
  grid=always
  bx=always + single
  by=always + single
  bz=always + single
```

```
end:output


begin:output
  name = dens
  file_prefix = dens
#  #number of timesteps between output dumps
  dt_snapshot=5.0e-15
#  #Properties on grid
  grid=always
  number_density=always + no_sum + single + species
end:output


begin:output
  name = ejected
  file_prefix = ejected

#  #number of timesteps between output dumps
  dt_snapshot=5.0e-15

  ejected_particles = always + single
#  px = always + single
#  py = always + single
#  particle_weight = always + single
#  charge = always + single
end:output


begin:output
  name = DF
  file_prefix = DF

#  #number of timesteps between output dumps
  dt_snapshot=5.0e-15

  distribution_functions=always + single + no_sum
  particle_probes=never
  absorption = always + no_sum
#distinguish energy in laser and particle
  total_energy_sum = always + no_sum
end:output


begin:dist_fn
  name=en
  ndims=1
  dumpmask=always
  direction1=dir_en
  #range is ignored for spatial coordinates
  range1=(0,0)
  #resolution is ignored for spatial coordinates
  resolution1=2500
  include_species:Electron
  include_species:Hydrogen
  include_species:Carbon
```

```
  include_species:Oxygen
end:dist_fn

begin:dist_fn
  name=px
  ndims=1
  dumpmask=always

  direction1=dir_px

  #range is ignored for spatial coordinates
  range1=(0,0)

  #resolution is ignored for spatial coordinates
  resolution1=2500

  include_species:Electron
  include_species:Hydrogen
  include_species:Carbon
  include_species:Oxygen
end:dist_fn


#-------------------------------------------------------------------------
#PMMA: C5O2H8
#number of electrons per molecule=(5*6)+(2*8)+8=30+16+8=54
#number of ions per molecule=5+2+8=15
#total number of particles per molecule=54+15=69
#-------------------------------------------------------------------------

begin:species
  name=Electron
  charge=-1.0
  mass=1.0
# frac is not compatible with npart
#  frac=54/69
  npart_per_cell = 100
  dump=T
  temp=0
  density_min = 0.1 * den_max

  density = den_max
  density = if(rho(Electron) gt den_max,den_max,rho(Electron))
  density = if(x gt 0.02*micron,0,rho(Electron))
  density = if(x lt 0*micron,0,rho(Electron))
  density = if(y gt 7*micron,0,rho(Electron))
  density = if(y lt -7*micron,0,rho(Electron))
end:species

begin:species
  name=Carbon
  charge=6.0
  mass=1836.2*(12.011/1.01)
#  frac=5/69
  npart_per_cell = 30
  dump=T
```

```
  temp=0
#  density = density(Electron)*5*6/54
#  density = density(Electron)/6
  density = density(Electron)*0.093
end:species

begin:species
  name=Oxygen
  charge=8.0
  mass=1836.2*(15.999/1.01)
#  frac=2/69
  npart_per_cell = 30
  dump=T
  temp=0
#  density = density(Electron)*8*2/54
#  density = density(Electron)/8
  density = density(Electron)*0.037
end:species

begin:species
  name=Hydrogen
  charge=1.0
  mass=1836.2
#  frac=8/69
  npart_per_cell = 100
  dump=T
  temp=0
#  density = density(Electron)*8*1/54
#  density = density(Electron)
  density = density(Electron)*0.146
end:species
```

Appendix D

Igor Pro Electron Spectrometer Analysis Code

D.1 Igor Pro Procedure for the Electron spectrometer analysis

```
#pragma rtGlobals=3 // Use modern global access method and strict wave access.
#include <All IP Procedures>
#include <Image Saver>


//Constants for x to energy scale transformation through
//calibrated Quadratic Equation. refer to cal_v2 file
// k2*x^(2) + k1*x + k0
constant k0 = 72.192
constant k1 = -1.1901
constant k2 = 0.019385

constant l=120
constant dl=50

constant kk0 = 0.045117
constant kk1 =-0.00010373
constant kk2 =8.0602e-008
constant kk3 =-3.425e-012
constant kk4 =-9.6123e-015
//constant kk5 =-5.1695e-019

//constnat a1 to d3 are the gaussian fit for PSL/electron data
constant a1=0.03
constant b1=200
constant c1=75
constant d1=0

constant a2=0.006
constant b2=600
constant c2=250
constant d2=0

constant a3=0.0025
constant b3=2000
constant c3=550
constant d3=0


// usual cutting boundries are (0,570, 40, 180)
```

```
function cropping(name, left, right, top, bottom, i)
string name
variable left, right, top, bottom, i

//cropp image and display
wave filename=$name
wave filename_crop=$(name+"_crop")
make/D/O/N=(right-left+1,bottom-top+1) $(name+"_crop")
redimension/n=(-1,-1) $(name+"_crop")
duplicate/O/R=(left,right)(top,bottom) $name $(name+"_crop")
// newimage $(name+"_crop")
// ModifyImage ''#0 ctab={*,*,geo,0}

//integrate over y for cropped image
wave filename_crop_int=$(name+"_crop_int")
make/S/O/N=(right-left+1) $(name+"_crop_int")
redimension/n=(-1,-1) $(name+"_crop_int")
filename_crop_int[]=0
for(i=0; i<(bottom-top+1); i+=1)
// print i
filename_crop_int[]=filename_crop_int[p]+filename_crop[p][i]
endfor


//x2energy conversion
wave filename_crop_int_x=$(name+"_crop_int_x")
make/D/O/N=(right-left+1,1) $(name+"_crop_int_x")
filename_crop_int_x[]=(k2*(x^(2)))+(k1*x)+k0

//generate error wave
wave error_R=$(name+"_error_R")
wave error_L=$(name+"_error_L")
make/D/O/N=(right-left+1,1) $(name+"_error_R")
make/D/O/N=(right-left+1,1) $(name+"_error_L")
error_R[]=((x)^(2)-(l)^(2))/(2*x*l)*dl
error_R[0]=0
error_L[]=error_R[p]
error_L[0]=0

//PSL/electron
// from Hui chen, et.al, "Absolute calibration of image plates for electrons
// at energy between 100 keV and 4 MeV", Rev. of Sci. Ins. 79, 033301, 2008
wave psl_per_electron=$(name+"psl_per_electron")
wave number_of_electron=$(name+"number_of_electron")
make/D/O/N=(right-left+1,1) $(name+"psl_per_electron")
make/D/O/N=(right-left+1,1) $(name+"number_of_electron")
psl_per_electron[]=0
number_of_electron[]=0
// calibration with a gaussian fitting
make/D/O/N=(right-left+1,1) g1
make/D/O/N=(right-left+1,1) g2
make/D/O/N=(right-left+1,1) g3
make/D/O/N=(right-left+1,1) g4
g1[]=a1*exp(-((x-b1)^2)/(2*((c1)^(2))))+d1
g2[]=a2*exp(-((x-b2)^2)/(2*((c2)^(2))))+d2
g3[]=a3*exp(-((x-b3)^2)/(2*((c3)^(2))))+d3
```

```
psl_per_electron[]=g1(x)+g2(x)+g3(x)+0.0065
// calibration with define step function from data.
// psl_per_electron[0,89]=2.95e-2
// psl_per_electron[90,117]=3.68e-2
// psl_per_electron[118,134]=1.9e-2
// psl_per_electron[135,154]=1.13e-2
// psl_per_electron[155,198]=0.90e-2
// psl_per_electron[199,559]=0.85e-2
// calibration with pololymal. this fitting leads
// exaggeration in range lower than 100 keV
// psl_per_electron[]=kk0+kk1*filename_crop_int_x[p]
// +kk2*(filename_crop_int_x[p]^2)
// +kk3*(filename_crop_int_x[p]^3)
// +kk4*(filename_crop_int_x[p]^4)
// +kk5*(filename_crop_int_x[p]^5)
number_of_electron[]=filename_crop_int[p]/psl_per_electron[p]


//plot Energy vs Number of ptl
Display 'filename_crop_int'[][0] vs 'filename_crop_int_x'[][0]
ModifyGraph standoff=0;DelayUpdate
SetAxis left 0,*;DelayUpdate
SetAxis bottom 0,1500
Label left "PSL";DelayUpdate
Label bottom "Energy (keV)"
Legend/C/N=text0/F=0/S=3/A=MC
ModifyGraph minor(bottom)=1
ErrorBars 'filename_crop_int' X,wave=('error_R','error_L')

Display 'number_of_electron'[][0] vs 'filename_crop_int_x'[][0]
ModifyGraph standoff=0;DelayUpdate
SetAxis left 0,*;DelayUpdate
SetAxis bottom 0,1500
Label left "Number of Electrons";DelayUpdate
Label bottom "Energy (keV)"
Legend/C/N=text0/F=0/S=3/A=MC
ModifyGraph minor(bottom)=1

end



end
```

Bibliography

[1] http://en.wikipedia.org/wiki/Bragg_peak.

[2] http://wanda.fiu.edu/teaching/courses/Modern_lab_manual/beta_spectroscopy.html.

[3] http://en.wikipedia.org/wiki/File:Airy_Functions.svg.

[4] Annual progress reports, 2008.

[5] Annual progress reports, 2010.

[6] Matthew Allen, Pravesh K. Patel, Andrew Mackinnon, Dwight Price, Scott Wilks, and Edward Morse. Direct experimental evidence of back-surface ion acceleration from laser-irradiated gold foils. *Phys. Rev. Lett.*, 93:265004, Dec 2004.

[7] J. Badziak, E. Woryna, P. Parys, K. Yu. Platonov, S. Jabłoński, L. Ryć, A. B. Vankov, and J. Wołowski. Fast proton generation from ultrashort laser pulse interaction with double-layer foil targets. *Phys. Rev. Lett.*, 87(21):215001, Nov 2001.

[8] V S Belyaev, V P Krainov, V S Lisitsa, and A P Matafonov. Generation of fast charged particles and superstrong magnetic fields in the interac-

tion of ultrashort high-intensity laser pulses with solid targets. *Physics-Uspekhi*, 51(8):793, 2008.

[9] F. Brunel. Not-so-resonant, resonant absorption. *Phys. Rev. Lett.*, 59(1):52–55, Jul 1987.

[10] A. E. Buenfil, C. Ruiz-Trejo, I. Gamboa-deBuen, P. Avils, O. Avila, C. Olvera, R. Robledo, M. Rodrguez-Ponce, H. Mercado-Uribe, M. Rodrguez-Villafuerte, and M. E. Brandan. Response of radiochromic dye films to low energy heavy charged particles. *Nuclear Instruments and Methods in Physics Research Section B: Beam Interactions with Materials and Atoms*, 197(3-4):317–322, December 2002.

[11] Hui Chen, Norman L. Back, Teresa Bartal, F.N. Beg, David C. Eder, Anthony J. Link, Andrew G. Macphee, Yuan Ping, Peter M. Song, Alan Throop, and Linn Van Woerkom. Absolute calibration of image plates for electrons at energy between 100 nbsp;kev and 4 nbsp;mev. *Review of Scientific Instruments*, 79(3):033301–033301–4, Mar 2008.

[12] B. I. Cho, J. Osterholz, A. C. Bernstein, G. M. Dyer, A. Karmakar, A. Pukhov, and T. Ditmire. Characterization of two distinct, simultaneous hot electron beams in intense laser-solid interactions. *Phys. Rev. E*, 80(5):055402, Nov 2009.

[13] T. E. Cowan, J. Fuchs, H. Ruhl, A. Kemp, P. Audebert, M. Roth, R. Stephens, I. Barton, A. Blazevic, E. Brambrink, J. Cobble, J. Fernández,

J.-C. Gauthier, M. Geissel, M. Hegelich, J. Kaae, S. Karsch, G. P. Le Sage, S. Letzring, M. Manclossi, S. Meyroneinc, A. Newkirk, H. Pépin, and N. Renard-LeGalloudec. Ultralow emittance, multi-mev proton beams from a laser virtual-cathode plasma accelerator. *Phys. Rev. Lett.*, 92:204801, May 2004.

[14] J. Denavit. Collisionless plasma expansion into a vacuum. *Physics of Fluids*, 22(7):1384–1392, 1979.

[15] Todd Ditmire. *Strong Field Physics*, volume 4. McGraw-Hill Professional, 2009.

[16] T. Esirkepov, M. Borghesi, S. V. Bulanov, G. Mourou, and T. Tajima. Highly efficient relativistic-ion generation in the laser-piston regime. *Phys. Rev. Lett.*, 92:175003, Apr 2004.

[17] T. Esirkepov, M. Yamagiwa, and T. Tajima. Laser ion-acceleration scaling laws seen in multiparametric particle-in-cell simulations. *Phys. Rev. Lett.*, 96:105001, Mar 2006.

[18] T. Zh. Esirkepov, S. V. Bulanov, K. Nishihara, T. Tajima, F. Pegoraro, V. S. Khoroshkov, K. Mima, H. Daido, Y. Kato, Y. Kitagawa, K. Nagai, and S. Sakabe. Proposed double-layer target for the generation of high-quality laser-accelerated ion beams. *Phys. Rev. Lett.*, 89(17):175003, Oct 2002.

[19] J. Fuchs, P. Antici, E. d/'Humieres, E. Lefebvre, M. Borghesi, E. Brambrink, C. A. Cecchetti, M. Kaluza, V. Malka, M. Manclossi, S. Meyroneinc, P. Mora, J. Schreiber, T. Toncian, H. Pepin, and P. Audebert. Laser-driven proton scaling laws and new paths towards energy increase. *Nat Phys*, 2(1):48–54, January 2006.

[20] J. Fuchs, Y. Sentoku, S. Karsch, J. Cobble, P. Audebert, A. Kemp, A. Nikroo, P. Antici, E. Brambrink, A. Blazevic, E. M. Campbell, J. C. Fernández, J.-C. Gauthier, M. Geissel, M. Hegelich, H. Pépin, H. Popescu, N. Renard-LeGalloudec, M. Roth, J. Schreiber, R. Stephens, and T. E. Cowan. Comparison of laser ion acceleration from the front and rear surfaces of thin foils. *Phys. Rev. Lett.*, 94:045004, Feb 2005.

[21] Erhard W. Gaul, Mikael Martinez, Joel Blakeney, Axel Jochmann, Martin Ringuette, Douglas Hammond, Ramiro Escamilla, Watson Henderson, Skyler Douglas, and Todd Ditmire. 1.1 petawatt hybrid, opcpa-nd:glass laser demonstrated. In *OSA Technical Digest (CD)*, pages FWX3–. Optical Society of America, October 2008.

[22] P Gibbon and E Forster. Short-pulse laser - plasma interactions. *Plasma Physics and Controlled Fusion*, 38(6):769, 1996.

[23] Paul Gibbon. `http://www.fz-juelich.de/jsc/splim/lectures/lecture8.pdf`.

[24] Paul Gibbon. *Short Pulse Laser Interactions with Matter: An Introduction.* Imperial Coll., London, 2005.

[25] S. J. Gitomer, R. D. Jones, F. Begay, A. W. Ehler, J. F. Kephart, and R. Kristal. Fast ions and hot electrons in the laser–plasma interaction. *Physics of Fluids*, 29(8):2679–2688, 1986.

[26] Stephen P. Hatchett, Curtis G. Brown, Thomas E. Cowan, Eugene A. Henry, Joy S. Johnson, Michael H. Key, Jeffrey A. Koch, A. Bruce Langdon, Barbara F. Lasinski, Richard W. Lee, Andrew J. Mackinnon, Deanna M. Pennington, Michael D. Perry, Thomas W. Phillips, Markus Roth, T. Craig Sangster, Mike S. Singh, Richard A. Snavely, Mark A. Stoyer, Scott C. Wilks, and Kazuhito Yasuike. Electron, photon, and ion beams from the relativistic interaction of petawatt laser pulses with solid targets. *Physics of Plasmas (1994-present)*, 7(5):2076–2082, 2000.

[27] B. M. Hegelich, B. J. Albright, J. Cobble, K. Flippo, S. Letzring, M. Paffett, H. Ruhl, J. Schreiber, R. K. Schulze, and J. C. Fernndez. Laser acceleration of quasi-monoenergetic mev ion beams. *Nature*, 439(7075):441–444, January 2006.

[28] A. Henig, S. Steinke, M. Schnürer, T. Sokollik, R. Hörlein, D. Kiefer, D. Jung, J. Schreiber, B. M. Hegelich, X. Q. Yan, J. Meyer-ter Vehn, T. Tajima, P. V. Nickles, W. Sandner, and D. Habs. Radiation-pressure acceleration of ion beams driven by circularly polarized laser pulses. *Phys. Rev. Lett.*, 103:245003, Dec 2009.

[29] D. S. Hey, M. H. Key, A. J. Mackinnon, A. G. MacPhee, P. K. Patel, R. R. Freeman, L. D. Van Woerkom, and C. M. Castaneda. Use of gafchromic

film to diagnose laser generated proton beams. 79(5):053501, 2008.

[30] Byoung ick Cho. *Experimental Study of Fast Electrons from the interaction of Ultra Intense Laser and Solid Density Plasmas*. PhD thesis, The University of Texas at Austin, 2008.

[31] Yasuaki Kishimoto, Kunioki Mima, Tsuguhiro Watanabe, and Kyoji Nishikawa. Analysis of fast-ion velocity distributions in laser plasmas with a truncated maxwellian velocity distribution of hot electrons. *Physics of Fluids*, 26(8):2308–2315, 1983.

[32] O. Klimo, J. Psikal, J. Limpouch, and V. T. Tikhonchuk. Monoenergetic ion beams from ultrathin foils irradiated by ultrahigh-contrast circularly polarized laser pulses. *Phys. Rev. ST Accel. Beams*, 11:031301, Mar 2008.

[33] W. L. Kruer and Kent Estabrook. J x b heating by very intense laser light. *Physics of Fluids*, 28(1):430–432, 1985.

[34] William L. Kruer. *The Physics of Laser Plasma Interaction*. Westview Press, 2003.

[35] R.F. Kubin and A.N. Fletcher. Fluorescence quantum yields of some rhodamine dyes. *Journal of Luminescence*, 27(4):455462, Dec 1982.

[36] T. V. Liseikina and A. Macchi. Features of ion acceleration by circularly polarized laser pulses. *Applied Physics Letters*, 91(17):–, 2007.

[37] Andrea Macchi, Federica Cattani, Tatiana V. Liseykina, and Fulvio Cornolti. Laser acceleration of ion bunches at the front surface of overdense plasmas. *Phys. Rev. Lett.*, 94:165003, Apr 2005.

[38] A. J. Mackinnon, M. Borghesi, S. Hatchett, M. H. Key, P. K. Patel, H. Campbell, A. Schiavi, R. Snavely, S. C. Wilks, and O. Willi. Effect of plasma scale length on multi-mev proton production by intense laser pulses. *Phys. Rev. Lett.*, 86(9):1769–1772, Feb 2001.

[39] EPOCH User Manual. `http://ccpforge.cse.rl.ac.uk/gf/project/epoch/`.

[40] E. Wolf M.Born. *Principles of Optics*. Cambridge University Press, Cambridge; New York, 1999.

[41] P. Mora. Plasma expansion into a vacuum. *Phys. Rev. Lett.*, 90(18):185002, May 2003.

[42] J. T. Morrison, C. Willis, R. R. Freeman, and L. Van Woerkom. Design of and data reduction from compact thomson parabola spectrometers. *Review of Scientific Instruments*, 82(3):–, 2011.

[43] Gerard A. Mourou, Toshiki Tajima, and Sergei V. Bulanov. Optics in the relativistic regime. *Rev. Mod. Phys.*, 78(2):309–371, Apr 2006.

[44] F. Nrnberg, M. Schollmeier, E. Brambrink, A. Blazevic, D. C. Carroll, K. Flippo, D. C. Gautier, M. Geiel, K. Harres, B. M. Hegelich, O. Lundh,

K. Markey, P. McKenna, D. Neely, J. Schreiber, and M. Roth. Radiochromic film imaging spectroscopy of laser-accelerated proton beams. 80(3):033301, 2009.

[45] Charlotte A. J. Palmer, N. P. Dover, I. Pogorelsky, M. Babzien, G. I. Dudnikova, M. Ispiriyan, M. N. Polyanskiy, J. Schreiber, P. Shkolnikov, V. Yakimenko, and Z. Najmudin. Monoenergetic proton beams accelerated by a radiation pressure driven shock. *Phys. Rev. Lett.*, 106:014801, Jan 2011.

[46] International Specialty Products. Configuration, specifications and performance data.

[47] B. Qiao, S. Kar, M. Geissler, P. Gibbon, M. Zepf, and M. Borghesi. Dominance of radiation pressure in ion acceleration with linearly polarized pulses at intensities of 10^{21} W cm^{-2}. *Phys. Rev. Lett.*, 108:115002, Mar 2012.

[48] B. Qiao, M. Zepf, M. Borghesi, and M. Geissler. Stable gev ion-beam acceleration from thin foils by circularly polarized laser pulses. *Phys. Rev. Lett.*, 102:145002, Apr 2009.

[49] M. Raghuramaiah, A.K. Sharma, P.A. Naik, P.D. Gupta, and R.A. Ganeev. A second-order autocorrelator for single-shot measurement of femtosecond laser pulse durations. *Sadhana*, 26(6):603–611, 2001.

[50] A P L Robinson, M Zepf, S Kar, R G Evans, and C Bellei. Radiation pressure acceleration of thin foils with circularly polarized laser pulses. *New Journal of Physics*, 10(1):013021, Jan 2008.

[51] S G Rykovanov, J Schreiber, J Meyer-ter Vehn, C Bellei, A Henig, H C Wu, and M Geissler. Ion acceleration with ultra-thin foils using elliptically polarized laser pulses. *New Journal of Physics*, 10(11):113005, Nov 2008.

[52] Marius S. Schollmeier. *Optimization and control of laser-accelerated proton beams.* PhD thesis, Universitat Darmstadt, 2008.

[53] H. Schwoerer, S. Pfotenhauer, O. Jackel, K.-U. Amthor, B. Liesfeld, W. Ziegler, R. Sauerbrey, K. W. D. Ledingham, and T. Esirkepov. Laser-plasma acceleration of quasi-monoenergetic protons from microstructured targets. *Nature*, 439(7075):445–448, January 2006.

[54] GE Healthcare Life Science. `https://www.gelifesciences.com/gehcls_images/GELS/Related%20Content/Files/1351177681492/litdoc29026296_20121218105651.pdf`.

[55] GE Healthcare Life Science. `https://http://wp1000855.server-he.de/screen/phoshpor%20screen.pdf`.

[56] Peter Sigmund. *Particle penetration and radiation effects.* Springer, Cham, 2014.

[57] R. A. Snavely, M. H. Key, S. P. Hatchett, T. E. Cowan, M. Roth, T. W. Phillips, M. A. Stoyer, E. A. Henry, T. C. Sangster, M. S. Singh, S. C. Wilks, A. MacKinnon, A. Offenberger, D. M. Pennington, K. Yasuike, A. B. Langdon, B. F. Lasinski, J. Johnson, M. D. Perry, and E. M. Campbell. Intense high-energy proton beams from petawatt-laser irradiation of solids. *Phys. Rev. Lett.*, 85(14):2945–2948, Oct 2000.

[58] Kazuo A. Tanaka, Toshinori Yabuuchi, Takashi Sato, Ryosuke Kodama, Yoneyoshi Kitagawa, Teruyoshi Takahashi, Toshiji Ikeda, Yoshihide Honda, and Shuuichi Okuda. Calibration of imaging plate for high energy electron spectrometer. *Review of Scientific Instruments*, 76(1):–, 2005.

[59] Donald Umstadter. Relativistic laserplasma interactions. *Journal of Physics D: Applied Physics*, 36(8):R151, 2003.

[60] L. M. Wickens, J. E. Allen, and P. T. Rumsby. Ion emission from laser-produced plasmas with two electron temperatures. *Phys. Rev. Lett.*, 41(4):243–246, Jul 1978.

[61] S. C. Wilks, W. L. Kruer, M. Tabak, and A. B. Langdon. Absorption of ultra-intense laser pulses. *Phys. Rev. Lett.*, 69(9):1383–1386, Aug 1992.

[62] S. C. Wilks, A. B. Langdon, T. E. Cowan, M. Roth, M. Singh, S. Hatchett, M. H. Key, D. Pennington, A. MacKinnon, and R. A. Snavely. Energetic proton generation in ultra-intense laser–solid interactions. *Physics of Plasmas*, 8(2):542–549, 2001.

[63] S.C. Wilks and W.L. Kruer. Absorption of ultrashort, ultra-intense laser light by solids and overdense plasmas. *Quantum Electronics, IEEE Journal of*, 33(11):1954 –1968, November 1997.

[64] X. Q. Yan, C. Lin, Z. M. Sheng, Z. Y. Guo, B. C. Liu, Y. R. Lu, J. X. Fang, and J. E. Chen. Generating high-current monoenergetic proton beams by a circularlypolarized laser pulse in the phase-stableacceleration regime. *Phys. Rev. Lett.*, 100:135003, Apr 2008.

[65] KITAGAWA Yoneyoshi et al. Prepulse-free petawatt laser for a fast ignitor. *IEEE Journal of Quantum Electronics*, 40:281–293, 2004.

[66] K. Zeil, S. D. Kraft, A. Jochmann, F. Kroll, W. Jahr, U. Schramm, L. Karsch, J. Pawelke, B. Hidding, and G. Pretzler. Absolute response of fuji imaging plate detectors to picosecond-electron bunches. *Review of Scientific Instruments*, 81(1):–, 2010.

[67] Xiaomei Zhang, Baifei Shen, Xuemei Li, Zhangying Jin, and Fengchao Wang. Multistaged acceleration of ions by circularly polarized laser pulse: Monoenergetic ion beam generation. *Physics of Plasmas (1994-present)*, 14(7):–, 2007.